UNIVERSITY OF CAMBRIDGE
DEPARTMENT OF CHEMISTRY

ENERGY LANDSCAPES OF MODEL GLASSES

A thesis submitted to the University of Cambridge in partial
fulfilment of the requirements for the degree of Doctor of Philosophy.

Thomas F. Middleton
Downing College

March 2003

DECLARATION

The work described in this thesis was carried out by the author in the department of Theoretical Chemistry at the University of Cambridge between October 1999 and March 2003. The contents are the original work of the author except where otherwise indicated, and contain nothing which is the outcome of collaboration. The contents have not previously been submitted for any degree or qualification at another institution. The number of words does not exceed 60 000.

Thomas F. Middleton
Cambridge, March 2003

ACKNOWLEDGEMENTS

I am indebted to my supervisor, Dr David Wales for his help throughout my PhD at Cambridge University. His energy and seamless flow of ideas have been a source of inspiration, and I am also grateful that he has been rather tolerant of all my various distractions.

I have also enjoyed working with the inhabitants of Room 3.60, the former Room 248, for the last four years. My discussions with three of my predecessors in the Wales group, Mark Miller, Jonathan Doye and Paul Mortenson were particularly fruitful. Mark and Paul were particuarly kind providing FORTRAN and LaTeX assistance.

The work was funded by the Engineering and Physical Sciences Research Council, and I also thank the National Lottery World Class Performance Fund for their help with living expenses.

For Sarah,
George, and Joseph.

ABSTRACT

The study of glasses and supercooled liquids is not for the faint hearted. The phenomenology is mysterious, and at first glance there appear to be as many 'universal' explanations of it as there are glass formers. At a fundamental level, this mysterious behaviour must be due to the underlying potential energy surface (PES), which is a consequence of the form of the interatomic or intermolecular potential function. Currently, little is known of the relationships between this hypersurface and the kinetics and thermodynamics of glass formers.

We eschew conventional simulation techniques to focus on the PES itself. We used global optimisation techniques to find the first fully crystalline structure for an archetypal model glass former, so that the inability of this system to form a crystal could be better understood. Searching techniques for local minima and interconnecting transition states on the PES were used to characterise regions of the PES close to crystal.

We then concentrated on low-lying regions of the PES, generating large databases of minima and transition states to better understand relaxation and transport processes below the glass transition. Large numbers of transition states with potential energy barriers kinetically accessible below the glass transition were found, leading to a classification of rearrangements in terms of those that contribute directly to diffusion, and those that do not. Low frequency harmonic modes corresponding to the experimentally observed boson peak were found, as was evidence that two-level systems could be present. The results at constant volume were also verified using a new algorithm that allowed the box lengths of the simulation supercell to vary.

Finally, we used a kinetic Monte Carlo scheme to simulate the supercooled liquid. Surprisingly, we found that for constant volume the energetic barrier heights to diffusion were essentially independent of temperature: instead the super-Arrhenius behaviour observed in molecular dynamics was due to increased connectivity between higher energy minima. Thus we provided an explanation for the connection between entropy and transport processes, which has been observed in both theory and experiment.

GLOSSARY

ABBREVIATIONS

bcc	Body-centred-cubic
BFGS	Broyden–Fletcher–Goldfarb–Shanno minimization algorithm
BLJ	Binary Lennard-Jones
CVD	Chemical vapour deposition
EF	Eigenvector-following
EF/BFGS	Hybrid eigenvector-following / BFGS algorithm
fcc	Face-centred-cubic
FLD	Frustration-limited domains
hcp	Hexagonal-close-packed
INM	Instantaneous normal modes
KA	Kob-Anderson
KMC	Kinetic Monte Carlo
LBFGS	Limited memory version of the BFGS algorithm
LJ	Lennard-Jones
MC	Monte Carlo
MCT	Mode coupling theory
MD	Molecular dynamics
MSB	Monotonic sequence basin
NEB	Nudged elastic band
PES	Potential energy surface
PVD	Physical vapour deposition
QHA	Quasi-harmonic approximation
REM	Random energy model
RMSD	Root mean squared deviation

RRKM	Rice-Ramsberger-Kassel-Marcus
SF	Stoddard-Ford
SPM	Soft potential model
SW	Stillinger-Weber
TLS	Two-level system
VDOS	Vibrational density of states
VTF	Vogel-Tamman-Fulcher
WLF	Williams-Landel-Ferry
WWW	Wooten, Winer and Weaire

SYMBOLS

D_P	The VTF strength parameter when pressure is the control variable
D_T	The VTF strength parameter when temperature is the control variable
E	Potential energy
e	Potential energy per atom
η	Viscosity
$g(\omega)$	Vibrational density of states
$\mathbf{g}$	The gradient vector
f_{dw}	The fraction of unstable diffusive normal modes in INM theory
$\Delta G^{\dagger}$	Gibbs free energy of activation
$\mathbf{H}$	The Hessian matrix
$\mathbf{H}^{\mathbf{MW}}$	The mass-weighted Hessian matrix
I	The number of negative Hessian eigenvalues
k_B	Boltzmann's constant
k_{ij}	The rate constant from state j to i
m_T	Steepness index
n_{neb}	Number of images in the NEB routine
N	Number of atoms in a system
ν_j	The frequency of the jth normal mode
Q_6	Order parameter for crystallinity
Q_j	The jth normal mode coordinate

$S\mathbf{q}$	The static structure factor for the wavevector $\mathbf{q}$.
S	Entropy
S_c	Configurational entropy
$\sigma(e)$	Basin enumeration function
t	Time
T	Temperature
T_0	Vogel-Tammann-Fulcher viscosity divergence temperature
T_2	Gibbs-Dimarzio second-order phase transition temperature
T_c	The critical temperature of mode coupling theory
T_g	The glass transition temperature
T_K	The Kauzmann temperature
T_μ	Microcanonical temperature
θ	KWW stretching parameter
$\mathbf{W}$	The transition matrix in kinetic Monte Carlo simulation
$Z(T)$	The canonical partition function at temperature T
ω_j	The angular frequency of the jth normal mode
$\Omega(E)$	The microcanonical density of states at total energy E

UNITS

Generally, the most appropriate units to use for results described in this dissertation are the 'natural' units, which are defined by the parameters of the potential function:

ϵ	Energy
σ	Distance
m	Mass
$\sqrt{m\sigma^2/\epsilon}$	Time
$\epsilon\sigma^{-3}$	Pressure

CONTENTS

1

THE MYSTERIES OF SUPERCOOLED LIQUIDS AND THE GLASS TRANSITION

> *Had I been present at the Creation, I would have given some useful hints for the better ordering of the universe.*
>
> Alfonso 'The Wise' 1221-84
> King of Castile and Leon 1252-84

There can be little doubt that Alfonso 'The Wise' would have placed the glassy state at the top of his list of handy hits for the Creator. Early in our scientific education, we learnt that liquids freeze *at* their freezing point: and during everyday life we observe little that might contradict this simplistic interpretation. In fact, our science teachers were telling us half-truths: liquids can be 'supercooled', remaining fluid below the temperature at which the solid state becomes thermodynamically favoured. Furthermore, many materials never form their equilibrium solid, instead they exist in an amorphous glassy state, in which they have the mechanical properties and appearance of a solid, whilst at an atomic level retaining the appearance of the liquid from which they were formed. Numerous solid state physicists have been intrigued by the phenomenologies of both this strange 'twilight zone' between solid and liquid, and the supercooled temperature range that precedes it as the material is cooled from the melt.

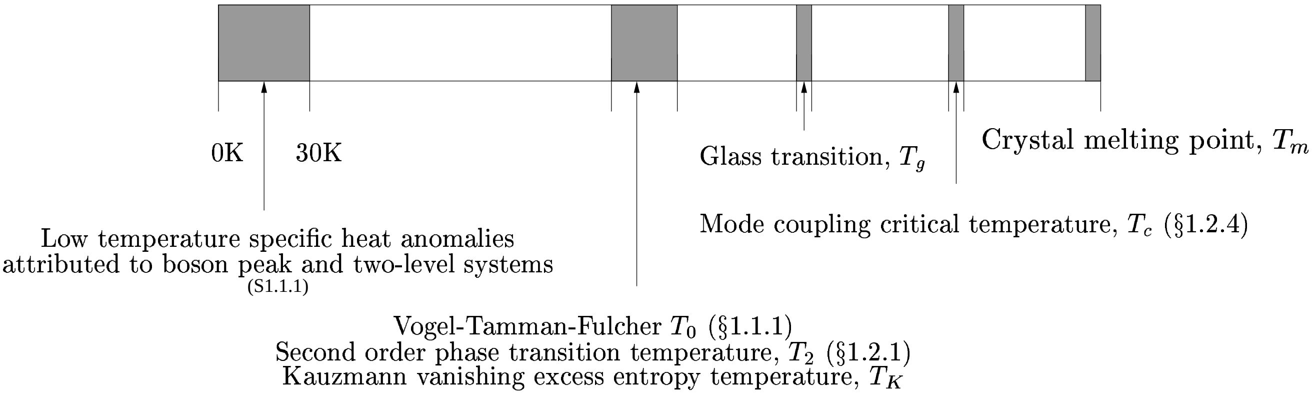

Figure 1.1: Schematic diagram summarising the characteristic temperatures relevant to the phenomenology of supercooled liquids and glasses.

It is surprisingly common for materials to form glasses—amorphous solids—when cooled below their melting point, despite the existence of a crystalline state with lower free energy. The glassy and supercooled liquid states have many anomalous properties: including deviations from the Arrhenius law, 'stretched exponential' relaxation, excess low frequency vibrational states and, perhaps, quantum mechanical two-level tunnelling systems. Two principal questions need to be answered: why do materials form glasses, and what produces their rich phenomenology?

In 1969 Goldstein[1] realised that the behaviour of glass formers at low temperature is a consequence of the form of the potential energy surface (PES). In the landscape dominated[1] regime, the dynamical behaviour takes place on two distinct timescales: fast intrawell oscillations and slow jumps over energy barriers between local minima on the $3N + 1$ dimensional PES. This treatment is applicable at temperatures where the two time scales are distinct. Above this point, the liquid is so fluid that the system does not have time to equilibrate within individual minima.

The work that we are presenting in this dissertation is concerned entirely with energy landscapes of model glasses, in an attempt to understand better the phenomenology of the deeply supercooled and amorphous solid regimes. In the body of this introduction, we will summarise the intriguing properties of glass formers, some key statistical mechanical theories, and outline some recent theoretical studies of energy landscapes.

1.1 PHENOMENOLOGY OF SUPERCOOLED LIQUIDS AND GLASSES

The description of thermodynamic and kinetic properties of glass formers is dominated by a plethora of characteristic temperatures, which are derived from statistical mechanical theories or extrapolations, or are simply the temperatures at which transitions take place. Figure 1.1 is an attempt to summarise these temperatures graphically, for ease of reference.

Starting from the high temperature end, T_m is the melting point of the crystal, below which the liquid is, by definition, supercooled and is in metastable equilibrium. T_c is the temperature at which idealised mode coupling theory (MCT) predicts that the relaxation times will diverge (§1.2.4). T_g is the experimental glass transition temperature, generally defined as the point at which the viscosity of the supercooled liquid reaches 10^{13} poise. T_0, T_K and T_2, although obtained in different ways, are often considered equivalent, and are discussed in §1.1.1, §1.1.2 and §1.2.1, respectively. Finally, in the 0 - 30 K region, anomalies are observed in the specific heat capacity: these are discussed in §1.1.6.

1.1.1 SUPER-ARRHENIUS BEHAVIOUR

The transport properties of many supercooled liquids slow down much more rapidly approaching the glass transition than the Arrhenius law, $\exp\left(-\Delta G^{\dagger}/RT\right)$ might predict. The activation free energies for these processes, $\Delta G^{\dagger}$, appear to increase as the temperature decreases. Several fitting functions have been proposed, of which the Vogel-Tammann-Fulcher equation is probably the most commonly used:[2–4]

$$\tau = \tau_0 \exp\left[A/(T - T_0)\right], \tag{1.1}$$

where τ is the relaxation time, A is a constant, and T_0 is a non-zero temperature at which the relaxation time appears to diverge. The VTF expression is usually a good fit over 2 to 4 orders of magnitude in relaxation time, in the temperature range approaching the glass transition.

Angell has used a T_g-scaled Arrhenius plot of the viscosity to classify liquids as 'strong' or 'fragile'.[5] Figure 1.2 is a schematic illustration of such a fragility plot. Liquids at the strong extreme, for which the activation energy is constant, tend to

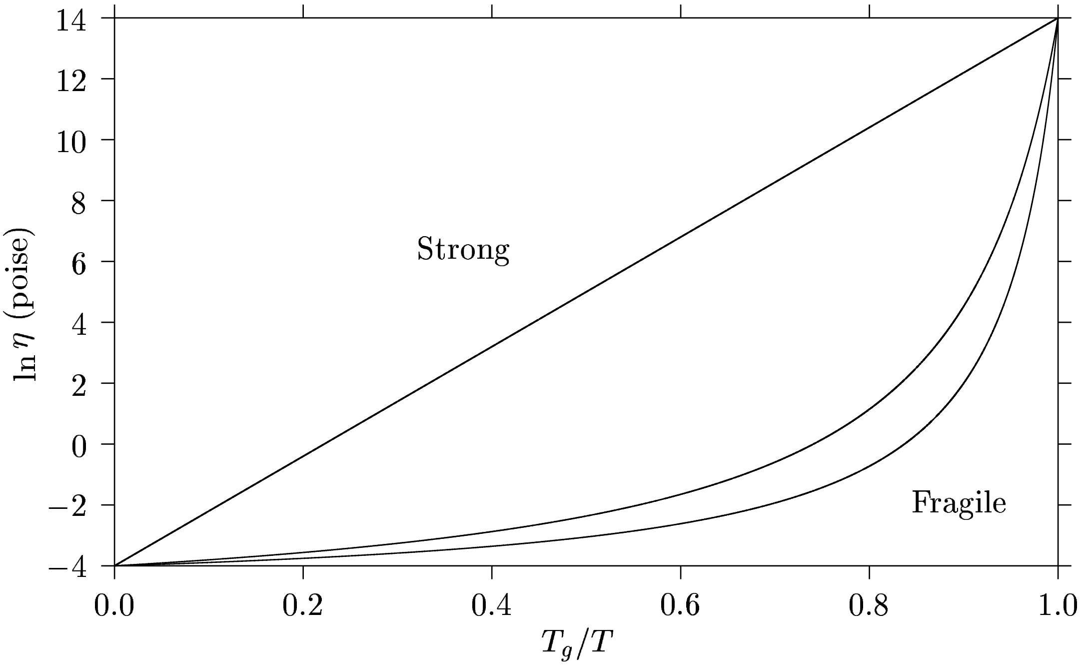

Figure 1.2: Schematic 'fragility plot', after Angell.[5] Relaxation and transport processes in strong liquids have an Arrhenius temperature dependence, with a constant activation energy. As the glass transition temperature, T_g, is approached from above, the activation energy in fragile liquids appears to increase.

be covalent network formers, of which the most familiar example is SiO_2. A strength parameter, D_T, is sometimes defined as $D_T = A/T_0$. D_T tends to infinity for strong liquids, because $T_0 = 0$ for materials that obey the Arrhenius law exactly. An analogous equation can be used to describe the pressure dependence, with a similarly defined strength parameter, D_P.[6,7] Another common definition of kinetic fragility is the 'steepness index',[8] m_T, which is defined as:

$$m_T = \left. \frac{\partial \log \tau}{\partial (T_g/T)} \right|_{T=T_g}, \qquad (1.2)$$

where τ is the characteristic relaxation time of the liquid, and T_g is the glass transition temperature.

It is a reasonable assumption that the dominant process limiting transport and relaxation in SiO_2 is the breaking of the Si−O bond. At the other extreme, the interactions in fragile liquids tend to be weaker and less directional, such as Coulomb or van der Waals forces. In fragile liquids, the glass transition is often marked by a large jump in the heat capacity, a feature that Angell has associated with a higher density of minima on the energy landscape per unit energy increase, with low barriers between them.[9] This discontinuity in the heat capacity defines 'thermodynamic fragility'. This is an example of the apparently coincidental correlations between kinetic and thermodynamic properties that are common in the phenomenology of supercooled liquids and glasses.

Stillinger has hypothesised that the super-Arrhenius behaviour of fragile liquids is due to a potential energy landscape in which the minima are arranged into 'megabasins' or 'craters'.[10] Thus, as the temperature decreases the system spends more time at the bottom of these megabasins, and the effective activation energy increases. At the other extreme, strong liquids would have a 'uniformly rough' energy landscape, leading to Arrhenius temperature dependence.

1.1.2 THE KAUZMANN PARADOX AND THE 'ENTROPY CRISIS'

Liquids have higher specific heats than crystals, and so the entropy difference between the liquid and the crystal decreases as the liquid is cooled. Kauzmann pointed out[11] that extrapolation of experimental data for the excess entropy implied that it would vanish for many liquids at a non-zero temperature, T_K. If this trend were continued below T_K, the entropy of the liquid would eventually become negative! Of course, the idea of such an 'entropy crisis' violates the third law of thermodynamics.

In practice, however, the glass transition intervenes, rapidly decreasing the heat capacity to a value similar to that of the crystal. Kauzmann's paradox is that the glass transition, a kinetic phenomenon, should enable the system to avoid a thermodynamic crisis.

Strong liquids tend not to have very small values of T_K. Indeed, Angell has pointed out that T_K correlates well with the VTF divergence temperature, T_0, and has suggested that $T_0 \equiv T_K$, and that they correspond to the configurational ground state temperature.[12]

1.1.3 STRETCHED EXPONENTIAL RELAXATION

The relaxation of a liquid in response to an external perturbation, such as its polarisation in response to an electric field or the stress due to an applied strain, can be described by a response function, $F(t) = [\sigma(t) - \sigma(\infty)] \, / \, [\sigma(0) - \sigma(\infty)]$, where σ is the measured quantity. In simple liquids, these functions have the conventional Debye form, a single exponential. In many supercooled liquids, they are often better fitted by the Kohlrausch-Williams-Watts (KWW) stretched exponential relaxation function:[13,14]

$$F(t) = \exp\left[-\left(t/\tau\right)^{\theta}\right] \qquad 0 < \theta \leq 1. \tag{1.3}$$

Conventional exponential Debye relaxation corresponds to $\theta = 1$. Fragile liquids tend to depart from Debye behaviour and θ is generally found to decrease with increasing fragility. Palmer et al. found that this type of stretched exponential function can arise from a model with hierarchically constrained dynamics, where some transition states may only be accessed once others have been overcome.[15] Thus slower degrees of freedom constrain faster ones, generating a wide range of relaxation times. This type of relaxation is observed in such a wide variety of systems that it seems likely it is produced by a number of different mechanisms. These have been classified by Edholm and Blomberg as either serial or parallel.[16] Serial mechanisms correspond to the model of Palmer *et al*, where the system proceeds through a number of barriers with different heights; parallel models invoke an ensemble of molecules, each with a different exponential relaxation rate. These authors found that stretched exponential relaxation was reproduced well by a barrier distribution proportional to $\theta \exp\left[\theta x - \exp\theta x\right]$: θ is the KWW exponent and $x = \epsilon - \tau_0$, where ϵ is the energy and τ_0 is a constant. They also derived a stable method to derive the barrier distribution from the exponential function.

1.1.4 α—β BIFURCATION

Johari and Goldstein used dielectric loss spectroscopy to study relaxation processes in rigid molecules, such as chlorobenzene,[17] and then non-rigid molecules, such as aliphatic alcohols.[18] In dielectric loss spectroscopy, a sinusoidal oscillating electric field is applied across the sample. The complex field and displacement[*] are given by $E^* = E_0 \exp(i\omega t)$ and $D^* = D_0 \exp(i\omega t - \delta_\epsilon)$, with D_0 and E_0 their respective amplitudes. A complex permittivity for the dielectric can then be defined by:

$$D^* = \epsilon^* E^* = (\epsilon' - i\epsilon'')E^*. \tag{1.4}$$

---

[*] The electric displacement, $\mathbf{D} = \epsilon_0 \mathbf{E} + \mathbf{P}$ where ϵ_0 is the permittivity of free space, $\mathbf{E}$ is the applied electric field and $\mathbf{P}$ is the polarisation.[19]

The real and imaginary parts of ϵ^* are thus related to the phase angle δ_ϵ by;

$$\epsilon' = |\epsilon| \cos \delta_\epsilon; \qquad \epsilon'' = |\epsilon| \sin \delta_\epsilon; \qquad \epsilon'/\epsilon'' = \tan \delta_\epsilon. \tag{1.5}$$

ϵ'' is known as the dielectric loss factor, as it can be shown that it is proportional to the rate of energy dissipation,[20] and $\tan \delta_\epsilon$ is the loss tangent. ϵ' and ϵ'' are obviously frequency dependent, and it is generally found that ϵ'' exhibits a peak at a frequency Ω_ϵ. ϵ' decreases monotonically from its static value ϵ_R, to a limiting high frequency value ϵ_∞. In the materials studied by Johari and Goldstein, ϵ_R and ϵ_∞ are sufficiently similar that the peak positions in $\tan \delta_\epsilon$ and ϵ'' can be considered equivalent.

It is inferred that the position of the peak in ϵ'' corresponds to the rate of dielectric relaxation in the material, and thus it is inversely proportional to the characteristic relaxation time. Hence an Arrhenius plot, $\ln \Omega_\epsilon$ against T^{-1}, should yield the activation energy for dielectric relaxation.

Johari and Goldstein found that it was apparently a 'near universal' property of glass formers that above the glass transition the position of Ω_ϵ had super-Arrhenius temperature dependence, with the activation energy in the $30 - 110$ kcal/mol range, and that the peak disappeared close to T_g. Above and below T_g, there was an additional peak with Arrhenius behaviour, and an activation energy between 4 kcal/mol and 10 kcal/mol. They labelled these peaks α and β, respectively, and inferred that the α peak corresponded to structural relaxation—which is frozen out at the glass transition— and the β peak corresponded to some form of 'secondary relaxation'. Such a bifurcation had previously been well-documented in polymer glasses,[21] with the obvious mechanism being that primary relaxation corresponded to movement of the polymer chains themselves, whereas the movement of polar side groups produced the secondary relaxation. At high temperatures, polymer glasses tend to exhibit a single peak in the ϵ'' spectrum, with Arrhenius temperature dependence and the same activation energy as the low temperature β processes. Bifurcation cannot be observed directly, owing to the breadth of the α peak. Thus a bifurcation temperature, $T_{\alpha\beta}$, can only be obtained from extrapolation.

While there is a simple and convincing explanation for this bifurcation in polymer glasses, Johari and Goldstein were only able to speculate about possible mechanistic explanations in the molecular glasses that they had studied.[17,18,22]

1.1.5 STOKES-EINSTEIN DECOUPLING

Another decoupling often occurs at a temperature around $1.2\,T_g$.[23–30] Above this temperature, both the translational and rotational diffusion coefficients are inversely proportional to the viscosity, as predicted by the Stokes-Einstein and Debye-Stokes-Einstein equations:

$$D_t = \frac{k_\mathrm{B}T}{6\pi\eta r_s}, \tag{1.6}$$

$$D_r = \frac{1}{6\tau_c} = \frac{k_\mathrm{B}T}{8\pi\eta r_s^3}. \tag{1.7}$$

D_t and D_r are the translational and rotational diffusion coefficients, respectively, r_s is the spherical radius of the molecule and η is the viscosity. The rotational diffusion time, τ_c, is the mean time taken for a molecule to rotate by 1 radian.

Approaching T_g, it is found that D_r and the viscosity remain inversely proportional, as predicted, while D_t is enhanced, sometimes by more than two orders of magnitude.[24,25,31] The size of the enhancement of D_t depends on the choice of probe molecule used to measure translational diffusion: the enhancement is greatest for those of a similar size to those of the substrate, while it is negligible for much larger probe molecules.[25]

The breakdown of the Stokes-Einstein equation is often taken to mean that, on average, the molecules translate further for each rotation. However, Ediger has pointed out that this is only the case if the supercooled liquid is dynamically homogeneous.[26] If the liquid is heterogeneous, Stokes-Einstein breakdown is still possible even if translational and rotational mobility remain proportional to each other within ‘slow’ or ‘fast’ regions. This is because the correlation functions that contribute to the two diffusion constants are averaged differently: D_r is dominated by slowly rotating molecules, while the most important contributions to D_t are from fast-moving molecules. This is because, to a first approximation, experiments measure $\langle\tau\rangle$ for rotation, while they measure $\left\langle\tau^{-1}\right\rangle^{-1}$ for translation.

1.1.6 LOW TEMPERATURE ANOMALIES: BOSON PEAKS AND TWO-LEVEL SYSTEMS

Many thermodynamic properties of glasses are anomalous at low temperatures, for instance the specific heat, which is predicted by Debye theory to be proportional to T^3

as $T \to 0$, has an excess linear term. In the $0-10$ K region, a two-level tunnelling model has been invoked to explain the anomalies,[32–34] while between 10 and 30 K extra low-frequency vibrational states, known as the 'boson peak', are generally accepted to produce the excess.[34–36]

Two-level systems have been suggested as the cause of the anomalous specific heat and thermal conductivity of glasses in the $0-10$ K region.[32–34] A two-level system is a pair of minima separated by a barrier that produces a splitting of around 1K, after tunnelling has been taken into account.[37] Angell has noted that anomalous behaviour in the $0-10$ K and $10-30$ K regions tend to occur together if they are seen at all,[36, 38, 39] and inferred that the same low frequency, anharmonic modes are associated with the boson peak and two-level systems. It is certainly conceivable that the potential will be very anharmonic at the bottom of a minimum that is connected to a low lying transition state, as is the case in a two-level system.

At low frequency, the density of states in Debye theory, $g_D(\omega)$, is expected to be proportional to ω^2. Most crystalline materials follow this behaviour well at low frequencies. In glasses, the boson peak is visible as an excess in $g(\omega)$ at low frequency ($\nu \sim 1$THz) over that predicted by Debye theory. This phenomenon has been observed with a number of experimental techniques, including neutron scattering[40] and Raman spectroscopy.[41]

The analysis of vibrations in crystals is simplified by the periodicity. A wave vector, $\mathbf{q}$, can be introduced, which is related to the size of the unit cell and characterises the vibrational eigenvalues. For a crystal of M unit cells with N atoms in each, there are M values of $\mathbf{q}$, each with $3N$ corresponding values of the vibrational eigenvalue, $\omega_j(\mathbf{q})$. Hence, in a crystal, there are $3N$ 'branches' in the Brillouin zone. Acoustic branches and optic branches are distinguished by the behaviour of the vibrational eigenvalues, the $\omega_j(\mathbf{q})$, as the wavevector $\mathbf{q}$ tends to zero: for the three acoustic branches $\omega_j(\mathbf{q})$ tends to zero in this limit, while for the remaining $3N-3$ optical branches, $\omega_j(\mathbf{q})$ tends to a finite value. In the $\mathbf{q} = \mathbf{0}$ limit, the displacements of the atoms are totally in phase for acoustic modes. The modes can be further subdivided into transverse and longitudinal, depending on the direction of the eigenvector with respect to the scattering vector, $\mathbf{q}$. However, for a general value of $\mathbf{q}$, the modes are a mixture of both optic and acoustic, and longitudinal and transverse components. In amorphous solids the unit cell is essentially infinite, and so the Brillouin zone collapses to $\mathbf{q} = \mathbf{0}$, and for a given branch, as q increases the loci of points in the $\omega - q$ relationship become increasingly smeared out and ill-defined. For a more detailed discussion of vibrations and neutron scattering, see Ref 42.

Although the boson peak has been the subject of much work, its origin remains controversial. Theoretical investigations of the boson peak that can be directly compared to the results presented here, include MD simulations of vitreous silica,[43,44] a soft-sphere glass[45] and the unit density Lennard-Jones glass.[46] These studies tend to suggest that the vibrations responsible for the boson peak are (quasi)localised and anharmonic, although Mazzacurati et al. suggested that the low frequency vibrations in a Lennard-Jones system were best described as a combination of uncorrelated random motion and well defined sinusoidal waves.[46] Schober and Oligschleger observed in their simulations of a soft sphere glass[45] that the number of modes with $\nu < 0.16$ decreased by 6% on ageing at 10% of the glass transition temperature for approximately 5000 vibrational periods.[45] This observation also suggests that at least some of the low frequency modes may be centred around defects, which are annihilated on ageing.

A number of simulations and experiments have suggested that the low frequency modes in silica contributing to the boson peak can be described as strongly anharmonic, localised relative rotations of coupled SiO_4 tetrahedra.[40,47,48] Taraskin and Elliott suggested that these modes may be produced by hybridisation of plane waves and low frequency band-tail states.[44] The band-tails are produced by the disorder, which destroys the band like structure of the crystalline vibrational density of states (VDOS), pushing states up and down in frequency. Thus, the plane waves can either interact with states that originate from a low-lying optic band or from the short wavelength part of the acoustic band. These authors also measured the Ioffe-Regel crossover for this system.[49] This is the point at which the mean free path of a wave equals its wavelength:

$$l_{IR} = \lambda_{IR}. \tag{1.8}$$

At this point, a wave can no longer be readily defined, and so the Ioffe-Regel crossover is a popular criterion for localisation. Using two different methods, they found that λ_{IR} was ≈ 1 THz, extremely close to the boson peak frequency.

The boson peak is almost a universal characteristic of glasses, although its intensity tends to decrease with increasing fragility.[12] Das has suggested in a recent paper that this correlation is due to the speed at which defects relax: long lived defects in strong glasses might give rise to extra intensity at an intermediate frequency following the quasielastic Raman peak.[50] He proposed that in fragile liquids the defects have a shorter lifetime, and so have less effect in the intermediate frequency range.

The soft potential model (SPM) has been used to simulate both the boson peak and two-level systems.[51,52] In this model, it is assumed that there exists a single type of soft structure, which gives to rise to low frequency anharmonic modes and two-level systems. The modes are described using a quartic polynomial in the mass-weighted displacement:

$$\hat{V}(\hat{x}) = \hat{\epsilon}\left[\hat{\eta}(\hat{x}/\sigma)^2 + \hat{t}(\hat{x}/\sigma)^3 + (\hat{x}/\sigma)^4\right]. \tag{1.9}$$

where σ is the length scale of the potential, and $\hat{x}$ is the mass-weighted displacement, $x = \sqrt{m_{\text{eff}}}\hat{x}$. $\hat{\eta}$ and $\hat{t}$ are adjustable parameters, whose variation is described by distribution functions. The soft potential can describe both single and double wells. Schober and Oligschleger used soft modes obtained from MD simulations of a soft sphere glass to form distribution functions for these parameters.[45] Their results agreed well with the assumption of the model that $\hat{\epsilon}$ is described by a narrow distribution, while $\hat{\eta}$ and $\hat{t}$ are described by random variations of the environment around the soft potentials.

1.1.7 EFFECTS OF PRESSURE

Measurements of D_T and m_T are not always consistent: Paluch et al. found in dynamic light scattering studies of the fragile glass former EPON 828 that D_T was pressure independent, while m_T decreased—the liquid became less fragile—as the pressure increased.[53] The sensitivity of the relaxation time and glass transition temperature to the pressure is given by the pressure coefficients $(d\ln\tau/dP)_{P\to 0}$ and $(dT_g/dP)_{P\to 0}$, respectively. In general, both of these increase with increasing fragility.[54]

Experimental studies of transport processes in glasses under high pressure have found that the free volume model of Cohen and Turnbull[55] fits experimental results reasonably well. In this model, the rate of diffusion in a hard sphere mixture depends on the probability of voids opening up through the redistribution of free volume. These authors obtained an equation analogous to the Arrhenius law, $D = A\exp\left[-\gamma v^*/v_f\right]$, in which A and γ are constants, and v^* is the 'activation volume'. $v_f = \bar{v} - v_0$, the difference between the average volume per molecule in the liquid, $\bar{v}$, and the van der Waals volume of the molecule, v_0.

The fragility of some glass-formers is affected by pressure, but the origin of this dependence is unclear. Liquids that are classed as fragile under atmospheric pressure either have fragilities that are not affected by pressure within experimental error, such as ortho-terphenyl,[56] chlorobenzene-decalin,[57] poly(vinyl acetate) and poly(ethyl acrylate);[58] increase with pressure, like glycerol and dibutyl phthalate;[59] or decrease with pressure, like epoxy resin,[7] poly(methyl acrylate), poly(vinyl chloride) and polystyrene.[58] Salol exhibits a maximum in its fragility as the pressure increases, which Schug et al. attributed to increased hydrogen bonding at high densities.[56] The fragility can even be path dependent: Huang et al. found that the for some polymers the steepness index, m_T, at the same (T_g, P_g, V_g) state point depended on whether it had been reached under isobaric or isochoric conditions.[58]

1.2 DOMINANT THEORIES OF THE GLASS TRANSITION

1.2.1 ADAM, GIBBS AND DIMARZIO'S CONFIGURATIONAL ENTROPY THEORIES

The theories of Gibbs and Dimarzio,[60] and Adam and Gibbs[61] suggested an underlying thermodynamic explanation for both the thermodynamics and kinetics of supercooled liquids and glasses, in terms of the configurational entropy.

Gibbs and Dimarzio used the familiar model of semiflexible polymer chains on a lattice, in which each lattice site is either occupied by only one monomer, or is vacant. They extended Flory's expression for the number of ways of packing polymer chains in solution[62] to describe a pure polymer containing vacancies, and thus were able to derive an expression for the canonical partition function of the system. This analysis predicted a second-order phase transition at a temperature T_2, below T_g, as the functional forms of the free energy, entropy and volume of the system were different above and below T_2, but were equal at $T = T_2$. Their model predicted that the configurational entropy of the glass would be zero at T_2, as the glass became trapped in the lowest possible potential energy configuration. Configurational entropy theories and the apparent coincidence of T_0, T_2 and T_K have given rise to the concept of an 'ideal glass'. The glass occupies its configurational ground state: the lowest amorphous potential energy minimum.

Comparison with experimental results for a number of polymer glasses suggested that the glass transition was the laboratory manifestation of the ideal second order transition: increased sluggishness of the supercooled liquid prevented observation of the predicted discontinuities at T_2. However, Stillinger has argued that for glasses of limited molecular weight, with physically realistic potentials, there cannot be either divergence of relaxation times or an ideal second order transition at the Kauzmann temperature.[63] Assuming that there is an ideal glass and a Kauzmann point at positive temperature, he deduced that either (a) structural excitations out of the ideal glass state are localised and require bounded enthalpy, but the number of them is not proportional to N, unlike independent excitations, or (b) that the barriers to excitation diverge as the concentration of excitations goes to zero. Neither of these conditions appear reasonable for glass-formers with small molecular weight and realistic potentials, but his arguments do not necessarily apply to polymer glasses where the mean molecular weight is proportional to the system size. In such systems there may not be configurations that are low in energy that can be created by introducing point defects in the ideal glass.

Adam and Gibbs subsequently developed these ideas, deriving their famous equation, which relates the relaxation time of the supercooled liquid directly to the configuration entropy, S_c:

$$\tau = \tau_0 \exp \frac{C'\Delta\mu}{TS_c}, \tag{1.10}$$

where $\Delta\mu$ is the free energy barrier per molecule or polymer segment in the cooperative group, and C' and A are constants. The derivation treats a polymer glass as a collection of independent subsystems, each composed of z monomers, that rearrange in a cooperative fashion. The next assumption is that the free energy barrier to rearrangement in this cooperative region is proportional to z, i.e. equal to $z\Delta\mu$. While this is reasonable for polymer glasses, in which relaxation takes place by the rotation of polymer segments, it is not obvious why this should necessarily be the case in non-polymeric or non-networking forming glasses with low molecular weight, such as OTP, or the binary Lennard-Jones model glasses discussed later in this dissertation. The temperature dependence of the minimum number of segments that can take part in a rearrangement, z^*, is derived using assumptions about the corresponding minimum configurational entropy, s_c^*, giving the crucial result:

$$z^* = \frac{N_A s_c^*}{S_c}. \tag{1.11}$$

In the simplest case, there are only two configurations available to the rearranging subsystems—'before' and 'after'—and so $s_c^* = k_\mathrm{B} \ln 2$. Thus, z^* is inversely proportional to the macroscopic configurational entropy of the system, S_c, and so the rearranging subsystems appear to increase in size as the temperature is lowered. [†]

The geometric progression for the average transition probability was then truncated at the term in z^*, to yield equation (1.10). VTF [‡] behaviour can be retrieved from equation (1.10) if the specific heat of the glass, C_p, is assumed to be constant and the relaxation time is reciprocally related to the transition probability. Angell has commented on the derivation of the Adam-Gibbs equation that 'the general view of theoreticians [is] that it cannot be understood'.[66]

The mathematics of relating entropy to subsystem volume is robust, but we question whether this shows that the cooperativity of rearrangements necessarily increases as the configurational entropy decreases. The Adam-Gibbs argument would not only apply to amorphous materials. Consider vacancy migration in, say, an fcc crystal. At sufficiently low temperatures, for a subsystem of a given size, only configurations containing one or zero vacancies will contribute significantly to the partition function. At a given temperature, we can define the average volume of crystal that contains a single vacancy, which diverges as we approach absolute zero provided that the crystal remains in equilibrium. However, while this minimum volume of crystal that has configurational entropy s_c^* is diverging, the barrier to diffusion obviously is not. The rearrangements available consist either of migration or destruction of this vacancy. However, these rearrangements involve at most $\mathcal{O}(10)$ atoms, and so it is obviously not the case that the barrier depends linearly on the value of z^* at low temperatures. We argue that the relationship between barrier height and the size of relaxing subsystems inherent in the derivation of the Adam-Gibbs equation is only applicable to polymers, because

---

[†] Adam and Gibbs used a slightly unusual definition for the configurational entropy, $S_c = k_\mathrm{B} \ln W_c(U, V)$, where W_c is the number of configurations corresponding to the macroscopic average potential energy, U, and average volume of the system, V. Thus S_c is the logarithm of the maximal term in the partition function.

[‡] Adam and Gibbs[61] related their model to the Williams-Landel-Ferry (WLF) equation,[64,65] which is mathematically equivalent to the VTF equation (1.1), but more popular for polymer glasses owing to the apparent universality of its parameters.

the covalent bonds and steric hindrance between monomers force them to relax cooperatively. Thus, in our view, it does not follow that glass-formers with low molecular weight should behave similarly.

Dzugutov suggests that interpretation of the cooperative dynamics of supercooled liquids in terms of Adam-Gibbs theory is 'logically incorrect', as the equation contains the configurational entropy—a property of the static structure—from which time-limited cooperativity is decoupled.[67] Johari has correctly pointed out that some care should be taken in the determination of S_c.[68] It is often assumed that at the glass transition the entropy difference between the glass and the crystal, $\Delta S(T_g)$, is is equivalent to the configurational entropy, $S_c(T_g)$. This assumption neglects any excess vibrational contributions to the entropy in the glass, which may be considerable owing to anharmonicity and an excess low frequency density of states.

Notwithstanding some of these counter-arguments, the Adam-Gibbs equation has successfully described the dynamics in several glass forming systems. Sastry's[69] results with the binary Lennard-Jones model are of particular interest to us. He obtained the configurational entropy using the relationship $S_c = S_{total} - S_{vib}$, where S_{vib} is the vibrational entropy within the harmonic approximation. The temperature and configurational entropy dependence of the diffusivity predicted by Adam-Gibbs, $\ln D \sim (TS_c)^{-1}$, was an excellent fit to the simulation results. As shown above, configurational entropy must be proportional to $T - T_0$ if the Adam-Gibbs and VTF equations are to be consistent. Sastry found S_c to be almost linear with $T - T_0$, with a slight increase in slope at lower temperatures.[69]

Hodge has observed that θ, the KWW non-exponential parameter, is proportional to $\ln z^* \, (T_g)$ for some polymer glasses.[70] z^* was obtained from a non-linear variant of the Adam-Gibbs equation, by assuming that $s_c^* = k_\mathrm{B} \ln 2$. The excellent fit obtained, while without theoretical basis, suggests an interesting relationship between cooperativity and stretched exponential relaxation.

1.2.2 UNIVERSAL SCALING LAW FOR DIFFUSION

Dzugutov has produced some remarkable results with a very simple scaling law between the diffusion constant and the difference in entropy between the liquid and the equivalent ideal gas.[71] The collision frequency derived from Enskog theory,[72,73] Γ_E, [§]

[§] The collision rate in Enskog theory is given by $\Gamma_E = 4\sigma^2 g(\sigma)\rho\sqrt{\pi k_\mathrm{B} T/m}$, where σ is the hard sphere diameter, $g(\sigma)$ the magnitude of the radial distribution function (RDF) at the point of contact, and the 'effective' hard sphere diameter σ are used to define a dimensionless diffusion constant, D^*:

$$D^* = D\Gamma_E^{-1}\sigma^{-2}, \tag{1.12}$$

where D is the diffusion constant. The argument is then that the frequency of local structural relaxation is limited by the number of accessible configurations per atom, which is taken to be proportional to $\exp(S)$, where S is the excess entropy - the difference between the system's entropy and that of the perfect gas under the same thermodynamic conditions. In the liquid domain, there appears to be a nearly universal law that $D^* = 0.049\exp(S_2)$, where S_2 is the excess entropy given by the two-body approximation.[74] The relationship even appears to be successful for diffusion of solid Ag in AgI, in which the cations are distributed randomly within a lattice of I^- ions. Agreement was not so good for silicon modelled by the Stillinger-Weber (SW) potential,[75] which was believed to be a consequence of the strong directional element in the interatomic potential invalidating the use of the Enskog collision frequency.

In a recent letter, Dzugutov has further developed his entropic-based theories of transport processes, studying diffusion in a metastable liquid of hard spheres.[76] Obviously, in the hard sphere liquid the free energy barrier to diffusion is entirely entropic, and D, the diffusion constant, is proportional to $\exp(S_a)$, where S_a is the height of the entropy barrier. At high packing fractions ($n_v > 0.5$), the diffusion constant deviates from the behaviour predicted in equation (1.12). Dzugutov envisaged this as a qualitative change in the form of the free energy landscape. At low density all the possible configurations are abundantly connected, and the hard-sphere atoms are able to move in an essentially independent manner. As the system is compressed, the diffusive motion of the hard-spheres are coupled within a certain range, which leads to extra high entropic barriers to diffusion.

1.2.3 FRUSTRATION LIMITED DOMAINS

Kivelson and co-workers have attempted to explain the phenomenology of supercooled liquids and the glass transition with their frustration limited domain (FLD) theory.[77–81] The basis of this theory is the idea that the preferred local structure around atoms in

---

ρ the number density and m the mass. In practice σ and $g(\sigma)$ are taken as the position and magnitude of the first maximum in the RDF.

the melt does not tile space, and is therefore different from the crystal structure. It is well known that this is the case for identical spherical particles, in which the preferred local orientation is polytetrahedral,[82] while the crystal is close-packed.

A crossover temperature, T^*, is proposed, which would be the melting temperature of a crystal with the preferred local structure, were it to tile space. As such a hypothetical crystal would have a lower free energy than the real crystal, $T^* \geq T_m$. Above this temperature, relaxation times follow an Arrhenius law, with an activation energy, denoted E_∞, which has negligible temperature dependence. Below T^*, clusters (domains) of the locally preferred structure form. The supercooled liquid, containing these FLDs is treated as being in equilibrium, although obviously this is metastable below T_m with respect to the crystal.

The derivation of the temperature dependence of the relaxation times below T^* comes from considering the free energy density of a domain with locally preferred structure of size L:

$$\frac{F(L)}{L^3} = \frac{\sigma}{L} - a + sL^2. \tag{1.13}$$

σ is the surface tension, and a is the free energy difference per unit volume between the liquid and the crystal, as in the standard nucleation picture. The additional term sL^2 represents the 'frustration induced strain', with the coefficient s not know *a priori*, but its scaling form is obtained by minimising equation (1.13). Further dynamic scaling arguments yield the following universal scaling expression for the activation free energy:

$$E(t) = \begin{cases} E_\infty, & \text{for } T > T^*, \\ E_\infty + Bk_\mathrm{B}T^*\left(1 - \frac{T}{T^*}\right),^{8/3} & \text{for } T < T^*. \end{cases} \tag{1.14}$$

B is a measure of the departure from Arrhenius behaviour, and thus is a measure of the kinetic fragility of the liquid. Within the FLD model, the larger the value of B, the less frustration.

1.2.4 MODE COUPLING THEORY

Mode coupling theory[83–86] (MCT) is a highly complex mathematical theory of supercooled liquids and glasses. It not relevant to this dissertation to discuss in detail the mathematics of MCT, but instead we will outline its principles and discuss its key results and their relevance to our studies of potential energy landscapes.

MCT relates the dynamics of supercooled liquids to $F(\mathbf{q},t)$, the density autocorrelation function for the wavevector $\mathbf{q}$:

$$F(\mathbf{q},t) = N^{-1} < \delta\rho^{*}(\mathbf{q},t)\delta\rho(\mathbf{q},t) > \tag{1.15}$$

where $\delta\rho(\mathbf{q},t)$ are the fluctuations of the Fourier components of the microscopic density, $\rho(\mathbf{q},t) = \sum_{j=1}^{N} \exp i\mathbf{q}.\mathbf{r}_j(t)$. The equation of motion of $F(\mathbf{q},t)$ is then:

$$\ddot{F}(q,t) + \Omega^2(q)F(q,t) + \int_0^t [M^0(q,t-t') + \Omega^2(q)m(q,t-t')]\dot{F}(q,t')dt' = 0. \tag{1.16}$$

Ω_q is just the vibrational frequency of sound waves with wavevector $\mathbf{q}$, which can be obtained from the static structure factor, $S(\mathbf{q}) = \langle \rho_{\mathbf{q}}\rho_{-\mathbf{q}} \rangle$. The equation is essentially that of a damped harmonic oscillator, with the addition of the nonlinear terms $M^0(q,t)$ and $m(q,t)$, which are known as the 'memory kernel'. $m(q,t)$ becomes the dominant term when the liquid is strongly supercooled.

The key approximations of mode coupling theory in all its forms are in the specification of the kernels $M^0(q,t)$ and $m(q,t)$. In the idealised form of the theory, presented by Bengtzelius, Götze and Sjölander in 1984,[87] $m(q,t)$ is expressed as a product of correlation functions with different wave vectors to second order only: $m(q,t) = \sum_{\mathbf{k}+\mathbf{p}=\mathbf{q}} V(\mathbf{q};\mathbf{k},\mathbf{p})F(\mathbf{k},t)F(\mathbf{p},t)$, where $V(\mathbf{q};\mathbf{k},\mathbf{p})$ are the mode coupling vertices, and can be calculated from the static structure factor. Thus this formulation of MCT describes the dynamics of flow in supercooled liquids in terms of coupling between pairs of phonon-like vibrations. Processes that involve 'hopping' rearrangements, in which a small number of molecules exchange positions or migrate via vacancies, cannot be described in this way, and so are not included in the idealised MCT. This is also the case for nucleation, which is believed to involve four-particle and possibly higher order correlations.[87] Thus MCT in its idealised form treats the liquid as if it were in equilibrium, describing its transport properties and relaxation by the coupling of density fluctuations. Temperature is included implicitly in the mode-coupling equations, as $\Omega^2(q)$, $M^0(q,t)$ and $V(\mathbf{q};\mathbf{k},\mathbf{p})$ depend on temperature.

Götze and Sjögren published the numerical solutions of the idealised mode-coupling equations in 1988.[88] At temperatures close to a critical temperature, T_c, three distinct regimes in the decay of the normalised density autocorrelation function, $\phi(t)$, are visible. In the first regime, $\phi(t)$ decays towards a non-zero value, f^c. Initially, this decay is rapid and essentially independent of temperature, corresponding to the ballistic motion of particles within cages formed by their nearest neighbours. $\phi(t)$ then exhibits an inflexion point in the next regime, which develops into a plateau at temperatures very close to the critical temperature. This is known as the β-regime, where the atoms are trapped within their cages, and so the $\phi(t)$ cannot decay any further. At longer timescales still, provided that $T > T_c$, $\phi(t)$ decays to zero, as these nearest neighbour cages break up and reform. This final decay to zero is known as the α-regime, in which structural relaxation takes place. As $T \to T_c$, the timescale for β-relaxation diverges, and below T_c, the plateau extends to $t = \infty$. The non-zero limit of $\phi(t)$ as t tends to ∞ corresponds to a breaking of ergodicity—the system is now trapped in a glassy state and no longer explores phase space uniformly. One should note that these α and β regimes are defined differently from the Johari-Goldstein α and β processes discussed in §1.1.4, although the α processes are generally taken to be the same in both descriptions. The MCT β is quite different from the Johari-Goldstein β, and these are often referred to as 'fast' and 'slow', respectively.

Hopping processes have been included in an extended version of MCT.[88,89] Coupling to currents is included, but the strength of this coupling, δ, cannot be calculated from measurable properties like the static structure factor, $S(\mathbf{q})$, unlike the parameters in the idealised equations. In this phenomenological model it is found that even below T_c, $\phi(t)$ decays to zero at long times, and thus the inclusion of these hopping processes restores ergodicity at all temperatures.

Since 1984, when the theory was proposed in its idealised form,[86,87] numerous experiments and simulations have been designed to test the predictions of MCT.[¶] In general, MCT appears to be very successful at describing the dynamics of glass formers in the β-regime and at high temperatures. MCT is particularly good at predicting the properties of some polydisperse colloids prepared to have short range steric interactions akin to hard spheres, a favourite model of theoreticians.[91–93] The energy landscape of a hard sphere system is trivial, consisting of an accessible volume of phase space in which no hard spheres overlap and there are no energy barriers, and an inaccessible region in which the potential energy is infinite.

[¶] For an extensive review of recent tests of MCT, see Ref 90.

Kob and Andersen[94–96] used MD to study an archetypal model for a glass former, the $A_{80}B_{20}$ binary Lennard-Jones mixture, which we will discuss in detail in later chapters. Their simulation runs were sufficiently long to verify that the system was in quasi-equilibrium—there was no systematic evolution of the temperature, potential energy or pressure—and thus they could measure a statistically significant diffusion constant. A fit of the temperature dependence to an idealised MCT power law, $D \sim (T - T_c)^\gamma$, yielded $T_c = 0.435$. Notably, the fit to this power law was better than to the VTF equation (1.1). Nauroth and Kob[97] then used partial structure factors to *predict* T_c by calculating coupling constants. Their theoretical value of T_c was around 0.922, a discrepancy which they ascribed partially to hopping processes, which would be implicitly included in the original power law fit. Thus, we might tentatively suggest this theoretical value of T_c as a potential cross-over temperature, where hopping processes become important. This hypothesis is validated by the excitation profiles (§1.3) for this system published by Sastry et al.,[98] as the predicted value of T_c from Ref 97 appears to coincide with the temperature at which the mean value of the inherent structure energy[‖] of the system starts to fall off its high temperature plateau.

MCT is complementary to our studies of the potential energy hypersurface. Its region of applicability is mainly in the moderately supercooled region, where the glass former relaxes via highly collective rearrangements that have barriers low compared to $k_\mathrm{B}T$ and are well described by coupled phonon-like modes. Furthermore, at these relatively high temperatures the interactions between atoms are dominated by their repulsive cores, and so the success of MCT, which in its simplest form only takes account of the first peak in $S(\mathbf{q})$ is unsurprising.

1.3 POTENTIAL ENERGY LANDSCAPES

Theoretical studies of potential energy landscapes tend to focus on the stationary points on the $3N + 1$ potential energy surface, at which the gradient vector vanishes. At minima, all the eigenvalues of the second derivative (Hessian) matrix are positive, and at a true transition state—by Murrell and Laidler's definition[99]—exactly one Hessian eigenvalue is negative.

[‖] The inherent structure of an atomic configuration is obtained by steepest-descent minimisation. Thus, 'inherent structure' is synomynous with 'minimum at the bottom of the basin of attraction in which the liquid's current configuration lies'. The inherent structure method is discussed in more detail in §1.3.2.

Empirical observations and some theoretical arguments suggest that the number of structurally distinct minima of the PES increases exponentially, as the system size, N, increases.[100–102] The number of minima with potential energy per particle, e, in the infinitesimal range between $e \pm de/2$ is thus given by:[102, 103]

$$\frac{d\Omega}{de} = C \exp N\sigma(e), \tag{1.17}$$

where C, and $\sigma(e)$ are N-independent quantities, although they are expected to depend on the density and the material in question. $\sigma(e)$ is the basin enumeration function, and configurational entropy arises from the presence of multiple minima at depth e. A parabolic $\sigma(e)$ gives rise to a Gaussian distribution of minima, which has been observed in simulation and obtained from heat capacity measurements, as expected from the central limit theorem.[69, 103, 104] Heuer and Büchner have argued that, for Lennard-Jones type system the configurational density of states is Gaussian at both global and local levels.[104] Thus, it appears not to be solely a consequence of the central limit theorem, but is a fundamental property of the PES, which arises from the form of the potential energy function.

1.3.1 RANDOM ENERGY MODELS AND INSTANTANEOUS NORMAL MODES

The notion that the configurational density of states is Gaussian is the basis of random energy models (REM), first analysed by Derrida.[105] The model exhibits both an entropy crisis and super-Arrhenius temperature behaviour of the typical escape time from a minimum, and in the mean-field limit can be shown to be mathematically equivalent to mode-coupling theories.[106] Derrida's original proof of the properties of the REM is somewhat involved:[105] here we present a summary of the results based on Wolynes' review.[106]

We start from a Gaussian distribution of states, centred at $E = 0$, with variance ΔE^2:

$$P(E) = \frac{1}{\sqrt{2\pi\Delta E^2}} \exp\left(\frac{-E^2}{2\Delta E^2}\right). \tag{1.18}$$

For simplicity, we use the microcanonical ensemble. The average density of states for a given energy is the product of the finite number of configurations available to the system Ω_0, and the distribution function:

$$\langle n(E)\rangle = \Omega_0 P(E)\,. \tag{1.19}$$

We then obtain an expression for the entropy, S, by approximating $n(E)$ by $\langle n(E)\rangle$, and using the definition for the microcanonical temperature, that $1/T_\mu = \partial S/\partial E$:

$$S = k_{\mathrm{B}} \ln\left(\frac{\Omega_0}{\sqrt{2\pi\Delta E^2}}\right) - \frac{\Delta E^2}{2k_{\mathrm{B}}T^2}. \tag{1.20}$$

This entropy reaches zero at a finite temperature, given by:

$$T_0 = \frac{\Delta E}{k_{\mathrm{B}}\sqrt{2\ln\Omega_0 - \ln\left(2\pi\Delta E^2\right)}}. \tag{1.21}$$

As the system tends to T_0 from above, the heat capacity has a parabolic form, before vanishing at T_0, when the system becomes trapped in a single state. Such an apparent phase transition is known as 'random first order', owing to its lack of any latent heat, but its discontinuity in its similarity order parameter.[106] A crude approximation to the barrier height can be obtained because most minima are surrounded with states with zero energy. At equilibrium at a temperature T, the thermally occupied minima have mean energy $\langle E\rangle = -\Delta E^2/k_{\mathrm{B}}T$. Thus, a crude approximation to the mean barrier to escape from a minimum becomes smaller as the temperature increases, and so the typical escape time is given by,

$$\tau = \tau_0 \exp\left[\Delta E^2/2(k_{\mathrm{B}}T)^2\right]. \tag{1.22}$$

This equation was used by Ferry[107] to describe the viscosity in various liquids, although he subsequently improved his fit by using the VTF law (§1.1.1). Although this model is rather crude, it is appealing inasmuch as it provides a possible explanation for the mysterious correlation between configurational entropy and relaxation, derived heuristically by Adam and Gibbs[61] (§1.2.1).

Recently random energy models have been related to the theories of transport properties based on instantaneous normal modes (INM).[108–114] The INM methodology builds on Zwanzig's theoretical relationship between the hopping rate between minima on the PES and the self-diffusion constant.[115] The INM are the eigenfunctions of the Hessian, the matrix of second derivatives of the energy with respect to mass-weighted atomic or molecular coordinates, and its eigenvalues are the squares of the corresponding instantaneous angular frequencies. The INM are obtained by averaging over an equilibrium distribution of configurations sampled in a molecular dynamics trajectory. At sufficiently high temperatures a significant fraction of the INM will be imaginary, corresponding to negative eigenvalues of the Hessian. INM theory derives a relationship between these imaginary frequencies f_u, and the hopping rate between minima, ω_h. Remarkably, it appears that for many supercooled liquids $D \sim \langle f_u \rangle$. A problem in the application of the theory is that there are INM present in the normal mode spectrum that are just due to anharmonicity within the basins on the PES, and therefore do not contribute to diffusion. Partial minimisation of the configurations appears to filter out most of these irrelevant imaginary frequencies.[116,117]

A relationship between f_u and the configurational entropy, S_c has recently been proposed,[118] and La Nave et al. have found a linear relationship between S_c and $\ln(f_{dw})$, the fraction of imaginary normal modes with double-well potential energy profiles.[119] Keyes then related these observations to the REM described above,[114] by treating the states in the REM as an ensemble of minima and saddles. It is then assumed that a stationary point with I negative eigenvalues is connected to I states of lower energy, and so $f_u(e)$ can be obtained since we know the distribution of states with energy e' connected to a state of energy e. The model reproduces the relationship between between S_c and $\ln f_u$. Qualitatively, this is because f_u for a state of energy e is given by the proportion of states with lower energy: so f_u for the system is approximately given by the fraction of states with energy below the most probable value, e^*. Likewise, a first approximation to the configurational entropy is the logarithm of the number of minima with energy lower than e^*.

In the uncorrelated REM, $P(e|e') = P(e)$ - i.e. the density of states with energy e' connected to a state of energy e is simply the global density of states. From a dynamical point of view, this leads to incorrect scaling with the total number of states, Ω_0, when calculating dynamical quantities. Keyes et al. have developed an alternative expression for $P(e|e')$ that reproduces the correct scaling properties with Ω_0.[113]

Subsequently, the relationship between the fraction of so-called diffusive imaginary normal modes and the configurational entropy has been found to hold for the BKS silica potential, despite the existence of a fragile-to-strong transition.[120] Irrespective of one's opinion of the validity of the INM approach, the suggestion that the correlation between entropy–a thermodynamic quantity—and relaxation times is due to connectivity of phase space is interesting, as it may explain why entropic theories of the glass transition (§1.2.1, §1.2.2) are so successful.

Kohen and Stillinger approximated a glassy energy landscape by mapping the inherent structures onto the vertices of a high dimensional hypercube.[121] The vertices were then projected onto the (x, y) plane according to their Euclidean coordinates. In general, a large number of vertices will be projected onto a single point in the (x, y) plane, and it was assumed that this set of inherent structures is degenerate. Three different functional forms of the potential function, $e(x, y)$, reproduced strong, fragile and 'degenerate' glassy behaviour respectively. The degenerate glass is so-called as it has a degenerate ground state, unlike the potentials used to reproduce strong and fragile behaviour. It also exhibits linear temperature dependence of its low temperature specific heat, within classical statistical mechanics. As discussed in Section 1.1.6, most amorphous materials have a linear contribution to the specific heat in the $0-10$ K region, but it is generally accepted that this is due to quantum mechanical two-level systems. Kohen and Stillinger admit that '...it will be a substantial challenge to determine if any real substances fall into the degenerate glass category.'[121]

Wales and Doye[122] developed a simple model, in which relaxation between groups of minima on a hypothetical PES was treated via transition state theory. A non-ergodic partition function was formulated, which excluded regions of configuration space that were not accessible in a given timescale. A set of seven parameters was used to characterise the topology of the PES and its vibrational properties. The full spectrum of strong-fragile behaviour was reproduced, with fragility being associated with a large number of local minima, lower effective potential energy barriers and higher vibrational frequencies. Increasing free energy barriers to relaxation with decreasing potential energy were a necessary condition for super-Arrhenius dynamics. A system with the thermodynamic properties of a strong liquid and the dynamics of a fragile liquid was produced by increasing the energy density of minima while keeping the vibrational frequencies constant. Such a parameter set may be unphysical as systems with many local minima are also expected to have a high vibrational frequencies. Stillinger and Debenedetti[123] reached a similar conclusion by constructing hypothetical landscapes from single basins with a cosine form. They constructed a number of PES's with the same basin enumeration functions, but with different barrier distributions, implying that there is no *mathematical* reason for the empirical correlation of thermodynamic and kinetic fragility. Instead, they suggested that there was an underlying physical cause. Wales has presented a possible explanation for this correlation in terms of catastrophe theory.[124]

1.3.2 RESULTS FROM QUENCHED SIMULATION TRAJECTORIES

The inherent structure method developed by Stillinger and Weber[10,100,125] has been used to analyse the behaviour of glassy systems in the 'landscape dominated' regime. The inherent structure of a configuration is the local minimum reached by following the steepest-descent path.[100] Molecular dynamics (MD) or Monte Carlo (MC) trajectories can be periodically quenched to yield the minima that the system has visited. Thus monitoring the transitions between inherent structures in simulations confirmed the existence of slow barrier crossings and localised rearrangements at low temperatures, as assumed in the Goldstein picture.[101]

Sastry et al. inferred a variation in the barrier distributions for the binary Lennard-Jones glass from MD simulations.[98] Configurations were quenched to local minima—their inherent structures—during a series of cooling runs following equilibration. The mean energy of the inherent structures was found to be practically independent of temperature for $T > 1\,\epsilon_{\mathrm{AA}}/k_{\mathrm{B}}$. Between $T \sim 1\,\epsilon_{\mathrm{AA}}/k_{\mathrm{B}}$ and $T \sim 0.4\,\epsilon_{\mathrm{AA}}/k_{\mathrm{B}}$ the inherent structure energy decreases with temperature, before reaching a second plateau. The height of the low temperature plateau decreases as the cooling rate slows. The variation of the inherent structure energy with temperature in this way is known as the 'excitation profile'. We have already mentioned the apparent coincidence between these two cross-over temperatures and the MCT critical temperatures derived from theory[97] and fitting to MD results,[?,95] in §1.2.4.

Inherent structures obtained from the runs at different temperatures were raised to a series of excitation temperatures, T_e. The variation in barrier height was inferred from the mean-square distance in configuration space through which the system moved in a given time. However, the mean square distance moved cannot be a simple function of the barrier distribution alone: it is also determined by the connectivity. A key aspect of the present contribution is that this missing factor is properly accounted for.

The excitation profile itself is also interesting. The excitation profile is closely related to the basin enumeration function, $\sigma(e)$. At low temperatures we assume that it is possible to disaggregate the Helmholtz free energy, A, into three distinct contributions:[103,126,127]

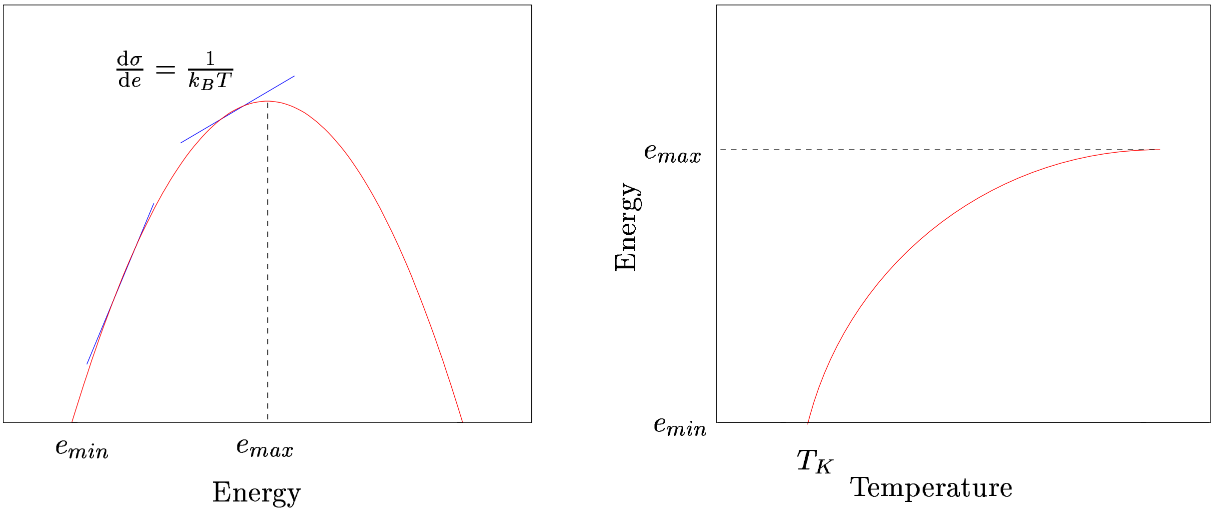

Figure 1.3: Schematic diagram of the relationship between the basin enumeration function $\sigma(e)$ (left panel) and the excitation profile (right panel). Adapted from Ref 103.

$$\frac{A}{Nk_{\mathrm{B}}T} = \frac{\bar{e}}{k_{\mathrm{B}}T} - \sigma(\bar{e}) + \frac{a^v}{k_{\mathrm{B}}T} \tag{1.23}$$

where $\bar{e}$ is the most probable basin energy sampled, $\sigma(\bar{e})$ is the number of basins with energy $\bar{e}$ and a^v is the vibrational free energy within the basins. Assuming that the vibrational contribution to the free energy is constant,[**] we can use the free energy minimisation condition to derive:

$$\frac{\mathrm{d}\sigma}{\mathrm{d}e} = \frac{1}{k_{\mathrm{B}}T}. \tag{1.24}$$

Using this relationship, we can then derive the temperature dependence of the average energy of the basins sampled by the system. Figure 1.3 illustrates the relationship between $\sigma(e)$ and the excitation profile. In the high temperature limit, the system occupies basins at energies close to the maximum of the parabolic $\sigma(e)$, forming a high temperature plateau region, as observed by Sastry et al.[98] At low temperatures, as $\sigma(e) \to 0$, the gradient of the basin enumeration is still finite, and thus $\mathrm{d}\sigma/\mathrm{d}e(e_{\mathrm{min}})$ gives us an estimate of the Kauzmann temperature, T_K. At this point, the system

---

[**] In fact, in later chapters we will find that the vibrational free energy is not constant, which has also been observed elsewhere.[69] However, this effect is not sufficiently large to affect the qualitative relationship between the excitation profile and the basin enumeration function, $\sigma(\bar{e})$.

occupies the configurational ground state minimum, with energy e_{min}. For finite cooling rates, this minimum will never be reached as the system becomes trapped in higher energy minima.

Angell has argued that the excitation profile is closely related to the fragility.[128] The thermodynamic fragility is defined by the magnitude of the heat capacity jump at the glass transition. Therefore fragile liquids will tend to have steeper excitation profiles, again assuming that the vibrational contribution to ΔC_p, the change in heat capacity, is negligible. A steeper excitation profile corresponds to a broad, high peak in the basin enumeration function. Angell has extended this argument to relaxation properties, using a bond lattice model, in which there is 'ideal mixing' between broken and unbroken bonds, deriving a two parameter relationship that performed as well as the VTF equation.[128]

The question of whether inter-basin transitions are Markovian or not is extremely pertinent to the current work. If it is the case that the motion between basins on the PES is Markovian, then the next basin visited is only on dependent on the current basin, not on any previous basins visited in the trajectory. In Chapter 5 we present results from kinetic Monte Carlo simulations, in which transition probabilities between minima are necessarily Markovian. Keyes and Chowdhary have carried out simulations on a 32-atom unit density Lennard-Jones system.[129] Quenching was carried out every five MD time steps, and diffusive motion was characterised by a distance between sequential minima on the trajectory. A 'Markov' diffusion constant, D_0, was derived, in which the diffusion constant was simply a function of the average separation between minima visited on the trajectory. Above a crossover temperature, close to the dynamic critical mode-coupling temperature, T_c, D_0 was an overestimate of the true diffusion constant measured by MD, suggesting that at high temperatures there was a high degree of back-correlation between diffusive rearrangements. At low temperatures, diffusion is well-described a random walk between basins. Furthermore the diffusion constant obtained by including correlations between adjacent minima in the trajectory, D_1 was still significantly greater than the correct diffusion constant, and was only $\sim 10\%$ smaller than D_0, indicating that these correlations might be long-lived. However, the question remained unanswered whether coarse-graining individual basins of attraction into megabasins—as in Stillinger's picture[10]—might recover Markovian behaviour.

Many recent studies have focused on saddle points with more than one negative eigenvalue: for a small subset see Refs. 130–135. Obviously, an explanation of the dynamics of supercooled liquids in terms of crossing higher order saddle points is intimately related to INM theory (§1.3.1). INM theory derives a relationship between the diffusion constant and the fraction of negative eigenvalues of the Hessian, $\langle f_u \rangle$, which must be connected to the average index of saddle points sampled. However, the Murrell and Laidler theorem[99] states that any pair of minima connected by a high index (≥ 2) saddle point must also be connected by one or more true transition states with lower potential energy barriers. Therefore it appears difficult to see why higher order saddles would be sampled significantly in the supercooled temperature range, unless there was a large entropic driving force for this to occur - i.e. the rate at which the number of saddle points grew with increasing index was sufficiently large to overcome the energetic barrier.

The mean index, I, of stationary points sampled in MD trajectories has been found to decrease linearly with decreasing temperature for the supercooled liquid,[131] approaching zero at a temperature close to the mode-coupling critical temperature, T_c (1.2.4). I does not quite reach zero below T_c, indicative of the presence of some low energy barriers at low potential energy. The relationship between temperature, or potential energy, and I suggests that it might be possible to generalise the Murrell and Laidler theorem—i.e. stationary points of index $\leq K-2$ linked by a saddle of index K must also be linked by one or more saddles of index $\leq K-1$ of lower energy.[136]

T_c has therefore been interpreted as a crossover between the deeply supercooled region, in which the system vibrates around local minima, occasionally jumping to other true transition states to other minima: and a moderately supercooled, 'saddles-ruled' region, in which diffusion takes place via excitation to high index saddles, followed by relaxation to minima or lower index saddles.[135] This hypothesis is rather difficult to quantify, as the 'basin' defined by a saddle point, as opposed to a local minimum, is ill-defined; and a rate theory describing transitions between higher index stationary points has yet to be formulated.[137]

A popular method of finding stationary points on the PES is the transformation to the 'squared gradient landscape' $W(\mathbf{x}) = \nabla E(\mathbf{x}) \cdot \nabla E(\mathbf{x})$:[131] all stationary points of the original PES, $U(\mathbf{x})$, are minima of $W(\mathbf{x})$ irrespective of their index. Doye and Wales have pointed out that this approach is rather problematic, partly because most minima of $|\nabla E|^2$ are not stationary points of the original PES.[137] Although this had been previously pointed out,[130,131,135] previous authors had assumed that they were not as significant Doye and Wales' more systematic search revealed. Furthermore, these authors found no evidence that the system resided closer to saddle points than minima at high temperature, using both the $|\nabla E|^2$ mapping and standard eigenvector-following (§2.1.1).[137]

Given the inconclusive nature of the evidence to support theories involving higher-index saddle points, and the problematic nature of these theories, we have decided in the present work to focus on minima and true transition states in our studies of the dynamics. If higher-index saddle points are of dynamic and thermodynamic relevance, this will be revealed by any deficiencies in our results.

1.3.3 ACTIVATION-RELAXATION AND OTHER TECHNIQUES

Barkema and Mousseau have used their activation-relaxation technique[138] to generate local minima and configurations close to saddle points on the potential energy surfaces of amorphous silicon (a–Si)[139,140] and silica[141,142] In this approach, first order saddle points on the PES—transition states—are located approximately by modifying the force vector, $\mathbf{F}$, so that the component parallel to the displacement from the nearest local minimum is reversed. The energy is minimised in the remaining $3N-1$ directions and the redefined force, $\mathbf{G}$, is followed iteratively.

$$\mathbf{G} = \mathbf{F} - (1+\alpha)\,(\mathbf{F}\cdot\widehat{\mathbf{r}})\,\widehat{\mathbf{r}}, \tag{1.25}$$

where $\widehat{\mathbf{r}}$ is the normalised vector parallel to the current displacement from the local minimum and α is a control parameter. When $\mathbf{G}$ changes sign, it is inferred that the system has passed through a saddle point, and the configuration at this point is taken as the approximate transition state. Local minima were obtained using conjugate-gradient minimisation. Using this technique, the barrier distribution for a–Si was found to peak at $4.0\pm0.5\,\text{eV}$.[139,140] Experimental results from conductivity measurements[143] and differential calorimetry[144] give activation energies for these transport processes of around 1–2 eV for a–Si. Their results for the Stillinger-Weber silicon potential are discussed in greater detail in §2.4.2.

Kopsias and Theodorou have used methods similar to those presented here to study a 198-atom homogeneous Lennard-Jones system.[145] Using eigenvector-following techniques, they generated a database of minima and transition states (a full discussion of eigenvector-following is given in §2.1.1). They then used the quasi-harmonic approximation (QHA) to investigate elementary transitions between pairs of local minima and to calculate the isothermal compressibility and elastic constants for the system. The QHA gives the Gibbs free energy of the system as:

$$G = V + \frac{1}{2}\sum_{i=1}^{3N-3} \hbar\omega_i + k_{\mathrm{B}}T \sum_{i=1}^{3N-3} \log\left[1 - \exp\left(-\frac{\hbar\omega_i}{k_B T}\right)\right] - V_0 \sum_{ij} \sigma_{ij}\epsilon_{ij}, \qquad (1.26)$$

where V is the potential energy of the inherent structure, the ω_i are the $3N-3$ vibrational eigenvalues for the system, V_0 is the equilibrium volume of the system in the stress-free state and σ_{ij} and ϵ_{ij} are the ij components of the stress and strain tensors respectively. These free energies can be used to compute transition rates between pairs of minima using elementary transition state theory: the rate from minimum A to minimum B is just $k_{B\leftarrow A} = k_B T/h \exp\left[-\Delta G^{\ddagger}/k_B T\right]$, where $\Delta G^{\ddagger}$ is the difference in free energy between the transition state and minimum A. Significantly, these authors found that the activation energies for transitions from different minima appeared to be independent of the absolute Gibbs energy values of the minima. This result appears to contradict the evidence of Sastry *et al.*,[98] who inferred that the energy barriers are greater lower down on the PES. The volume difference between two connected minima was found to be proportional to the Gibbs energy difference. This observation agrees well with experiments on real amorphous materials, where relaxation is often accompanied by an increase in density.

1.4 THESIS OVERVIEW

It would not be an exaggeration to say that any discussion of the endeavours of theoreticians in this field that is shorter than the Bible is necessarily incomplete. In the previous pages, I have attempted to outline some of the intriguing phenomenology, and highlight areas of research that are particularly relevant to the following chapters.

The aim of the research described in the following chapters was to study the PES's of some model glass formers, by finding representative samples of minima and the transition states that connect them. In the next chapter, we describe the methodology used for finding these stationary points, and the ways in which the data was analysed. The first chapter of results concentrates on global optimisation and crystalline regions of the PES's of the glass formers that we studied. We then move on to qualitative studies of the PES's and the statistics of their properties, focusing on regions of the PES that are low in energy and correspond to glassy configurations. The final chapter outlines kinetic Monte Carlo simulations in the temperature range for which the binary Lennard-Jones system is still a supercooled liquid. We use our stationary point searching algorithms to obtain diffusion constants, and hence we can directly relate the PES to the dynamics observed in MD simulation. In particular, we focus on super-Arrhenius behaviour.

2

METHODS

2.1 EXPLORING THE POTENTIAL ENERGY SURFACE

Stationary points on a PES are points where the gradient vector vanishes. A minimum is a stationary point with no negative Hessian eigenvalues (no imaginary normal mode frequencies). In the present work we follow Murrell and Laidler and define a true transition state as a stationary point with precisely one negative Hessian eigenvalue (one imaginary normal mode frequency).[99] For each transition state two barrier heights are then determined by the energy differences between the transition state and the two minima that are connected to it by steepest descent paths. As usual, we will refer to the larger barrier for a given transition state as the uphill barrier, because it must be overcome to move from the lower to the higher energy minimum. Similarly, the smaller barrier is referred to as the downhill barrier.

2.1.1 FINDING MINIMA AND TRANSITION STATES BY EIGENVECTOR-FOLLOWING

The basis of all the methods that we use to find stationary points on the $3N + 1$ dimensional PES is the well-established technique of eigenvector-following.[146–152] We start with the Taylor expansion to second order of the potential energy, V, at a general point in configuration space, $\mathbf{X}$:

$$V(\mathbf{X}+\mathbf{h}) = V(\mathbf{X}) + \mathbf{g}(\mathbf{X})^T\,\mathbf{h} + \frac{1}{2}\mathbf{h}^T\,\mathbf{H}(\mathbf{X})\,\mathbf{h}, \tag{2.1}$$

where $\mathbf{g}(\mathbf{X})$ is the gradient vector at $\mathbf{X}$, and $\mathbf{H}(\mathbf{X})$ is the Hessian, the matrix of second derivatives without mass-weighting. We can obtain the standard Newton–Raphson step from the condition $dV(\mathbf{X}+\mathbf{h})/d\mathbf{h}=0$:

$$\mathbf{h}_{\mathbf{NR}} = -\mathbf{H}^{-1}\mathbf{g}. \tag{2.2}$$

However it is not useful in this form, because the inverse of the Hessian is undefined, since bulk systems have three zero eigenvalues, corresponding to translational degrees of freedom. This problem can be circumvented by a shifting technique, which has been found to be more efficient for large systems than other alternatives proposed.[153] Analytic eigenvectors corresponding to overall translation can be obtained easily, and for each such eigenvector $\mathbf{e}$, we add a large multiple of $e_i e_j$ to the Hessian element H_{ij}. It is then straightforward to ignore steps along these eigenvectors.

We can solve the eigenvalue problem for the matrix $\mathbf{B}$:

$$\sum_{\beta=1}^{3N} H_{\alpha\beta} B_{\beta\gamma} = \varepsilon_\gamma^2 B_{\alpha\gamma}, \tag{2.3}$$

which enables us to transform to new orthogonal coordinates, $R_\alpha = \sum_{\beta=1}^{3N} B_{\beta\alpha} X_\beta$, giving a Newton–Raphson step and corresponding energy change of:

$$h_{\mathrm{NR},\alpha} = -\frac{g_\alpha(\mathbf{R})}{\varepsilon_\alpha^2} \quad \text{and} \quad \Delta E_{\mathrm{NR}} = -\sum_{\alpha=1}^{3N} \frac{g_\alpha(\mathbf{R})^2}{2\varepsilon_\alpha^2}, \tag{2.4}$$

where $g_\alpha(\mathbf{R}) = \partial E(\mathbf{R})/\partial R_\alpha$. Thus, terms with positive ε_α^2 will lower the energy, while terms with negative ε_α^2 will increase it. To find a minimum, we may have to start at a point with no negative Hessian eigenvalues, while to find a transition state we may need exactly one negative eigenvalue.[154,155] We can avoid these problems by using a Lagrange multiplier to find transition states systematically, which is the basis of the eigenvector-following approach. We use a separate Lagrange multiplier for each eigendirection:[151]

$$L = -E(\mathbf{R}) - \sum_{\alpha=1}^{3N} \left[g_\alpha(\mathbf{R})\, h_\alpha + \frac{1}{2}\varepsilon_\alpha^2\, h_\alpha^2 - \frac{1}{2}\mu_\alpha (h_\alpha^2 - c_\alpha^2) \right], \tag{2.5}$$

which gives the optimal step in eigendirection α

$$h_\alpha = \frac{g_\alpha(\mathbf{R})}{\mu_\alpha - \varepsilon_\alpha^2}, \tag{2.6}$$

and energy change

$$\Delta E = \sum_{\alpha=1}^{3N} \frac{(\mu_\alpha - \varepsilon_\alpha^2/2) g_\alpha(\mathbf{R})^2}{(\mu_\alpha - \varepsilon_\alpha^2)^2}. \tag{2.7}$$

Obviously, minimisation with respect to eigendirection α requires that $\mu_\alpha - \varepsilon_\alpha^2/2 < 0$, while maximisation requires that $\mu_\alpha - \varepsilon_\alpha^2/2 > 0$. We also require that the Newton–Raphson step is recovered in the vicinity of a stationary point—i.e. $\mu_\alpha \to 0$ as $g_\alpha(\mathbf{W}) \to 0$. In the work presented here, we used:

$$\mu_\alpha = \varepsilon_\alpha^2 \pm \frac{1}{2}|\varepsilon_\alpha^2| \left(1 + \sqrt{1 + 4 g_\alpha(\mathbf{R})^2/\varepsilon_\alpha^4}\right), \tag{2.8}$$

plus for minimisation, minus for maximisation, which gives steps:

$$h_\alpha = \frac{\pm 2 g_\alpha(\mathbf{R})}{|\varepsilon_\alpha^2|(1 + \sqrt{1 + 4 g_\alpha(\mathbf{R})^2/\varepsilon_\alpha^4})}. \tag{2.9}$$

In a full eigenvector-following stationary point search, we calculate analytic first and second derivatives at every step. Estimated values of the eigenvalues, $\varepsilon_\alpha^2(\text{est})$ can be obtained from the gradients at the present point, n, and the previous point $n-1$:

$$\varepsilon_\alpha^2(\text{est}) = \frac{g_\alpha(n) - g_\alpha(n-1)}{h_\alpha(n-1)}. \tag{2.10}$$

Comparison of these estimated eigenvalues with the real eigenvalues obtained from the Hessian matrix gives us some indication of the reliability of the steps in each eigendirection. The trust ratio is defined by:[151]

$$r_\alpha = \left| \frac{\varepsilon_\alpha^2(\text{est}) - \varepsilon_\alpha^2(n)}{\varepsilon^2(n)} \right|. \tag{2.11}$$

The maximum allowed step in each direction is either decreased or increased, according to whether r_α is more or less than a specified trust radius.

One of the main advantages of pure eigenvector-following is that it is possible to obtain systematically a large number of transition states connected to each minimum, by following each eigenvector in turn. However, for large systems eigenvector-following becomes prohibitive, because the diagonalisation of the Hessian becomes a computational bottleneck, as the computer time required scales as N^3. Thus, we have to use a hybrid method.

An arbitrary vector, $\mathbf{y}$, can be written as a linear combination of the normalised Hessian eigenvectors, $\mathbf{e}_i$:

$$\mathbf{y} = \sum_i a_i \mathbf{e}_i. \tag{2.12}$$

Hence, multiplication on $\mathbf{y}$ by the Hessian matrix n times gives:

$$\mathbf{H}^n \mathbf{y} = \lambda_1^n \left[a_1 \mathbf{e}_1 + \left(\frac{\lambda_2}{\lambda_1} \right)^n a_2 \mathbf{e}_2 + \left(\frac{\lambda_3}{\lambda_1} \right)^n a_3 \mathbf{e}_3 + \cdots \right]. \tag{2.13}$$

In the limit of large n, the dominant term is

$$\mathbf{y}_n = \lambda_1^n a_1 \mathbf{e}_1, \tag{2.14}$$

where λ_1 is the largest eigenvalue. Renormalisation of $\mathbf{y}_n$ to unity prevents it from becoming inconveniently large. To find the smallest eigenvalue, we shift all the eigenvalues down by λ_1— so that the smallest eigenvalue has the largest magnitude—and iterate again.

Diagonalisation of the Hessian matrix can now be avoided in transition state searches. Munro and Wales developed the hybrid eigenvector-following/conjugate gradient (EF/CG) technique, which uses the above iteration and shifting technique to find the smallest eigenvalue and its corresponding eigenvalue, and then the eigenvector-following formulation to calculate the size of the uphill step.[152] The Polak-Ribiere conjugate gradient (CG) technique[156] was used to minimize in the tangent space, by applying the projector $\hat{\mathcal{P}}\mathbf{x} = \mathbf{x} - (\mathbf{x} \cdot \hat{\mathbf{e}}_{min})\, \hat{\mathbf{e}}_{min}$. Subsequently, the computational speed of this method has been improved, by using Nocedal's limited memory Broyden-Fletcher-Goldfarb-Shanno (LBFGS)[157] routine to carry out the tangent space minimisation. Henceforth, we refer to this hybrid transition state searching method as EF/BFGS.

The disadvantage of this technique is that we may now follow only the 'softest' mode i.e. the eigenvector corresponding to the smallest eigenvalue. If we start a transition state search from a minimum, we are limited to a maximum of two transition states connected to it, corresponding to following the softest mode in both senses. In order to generate more transition states connected to a given starting minimum, we may either randomly perturb the atomic coordinates of the starting configuration before beginning the EF/BFGS transition state search, or use Wales' method based on hard sphere moves to generate a starting point.[158] This technique uses standard code for hard sphere molecular dynamics,[159] with the hard sphere radius taken as half the equilibrium pair separation for the potential in question. The system is given a $3N$-dimensional initial velocity vector of uniform random numbers, and the trajectory propagated until the time, τ, of the first hard sphere collision. Ignoring the potential, the trajectory can be propagated further, to time τ', where the distance between the colliding atoms is the equilibrium pair separation once more. For the bulk systems studied here, it was found that the most efficient starting point for the EF/BFGS transition state search was found to be the configuration at time τ, rather than τ', or $(\tau + \tau')/2$ with the separation of the colliding atoms rescaled to the equilibrium pair distance.[158] Our implementation of the algorithm demands the parameter t_{12}: for $t_{12} \leq 1$ the starting point is set to the configuration corresponding to $t = t_{12}\tau$, otherwise if $t_{12} \geq 1$ then the atoms are moved half way between the entrance and exit of their collision, with their separation rescaled to unity.

Ideally we would use an exact steepest-descent method to generate the paths to the minima that are linked by the saddle point. In practice, taking steps of order $0.01\,\sigma$ parallel and antiparallel to the transition vector, followed by BFGS minimisation almost invariably converges to the same pair of minima, and is much more computationally efficient.

A small number of full eigenvector-following steps (between 1 and 3) was used to converge all the stationary points to a root-mean-square (RMS) force of less than 10^{-6} reduced units. This precaution, which involves full diagonalisation of the analytic Hessian matrix, also assures us that the stationary points in question have the correct number of negative Hessian eigenvalues, namely zero for a minimum, and one for a true transition state. For an RMS force less than 10^{-6} units the energies per supercell are converged to better than ten significant figures for all the stationary points.

2.1.2 NUDGED ELASTIC BAND AND THE CONNECT ALGORITHM

The methods described above can be extended to generate pathways between a pair of disconnected minima.

Jónsson and collaborators have developed the nudged elastic band method, which generates approximate minimum energy paths between pairs of minima.[160] In the original implementation n_{neb} equally-spaced atomic configurations—'images'—are created by interpolation between the two minima. Each image is visualised as a point on an elastic band joining the minima. A force on each image is then defined in terms of components perpendicular and parallel to the nudged elastic band (NEB):

$$\mathbf{F}_i = \mathbf{F}_i^s|_{||} - \nabla V(\mathbf{R}_i)|_{\perp}, \tag{2.15}$$

where the 'true force' perpendicular to the elastic band is given by

$$\nabla V(\mathbf{R}_i)|_{\perp} = \nabla V(\mathbf{R}_i) - (\nabla V(\mathbf{R}_i) \cdot \hat{\tau}_i)\,\hat{\tau}_i. \tag{2.16}$$

where $V(\mathbf{R}_i)$ is the potential energy at the position of the i-th image, and $\hat{\tau}_i$ is the normalised local tangent to the elastic band. The 'spring force', parallel to the elastic band, is given by

$$\mathbf{F}_i^s|_{||} = (|\mathbf{R}_{i+1} - \mathbf{R}_i| - |\mathbf{R}_i - \mathbf{R}_{i-1}|)\,\hat{\tau}_i. \tag{2.17}$$

In the present work, we use a force constant, k, of $|\Delta E|/100(n_{neb}+1)\Delta s^2$, where ΔE and Δs are the energy difference and distance between the minima. The images are then moved, according to the force given by equation (2.15), using the limited memory BFGS optimisation scheme, until either a maximum number of steps has been reached, or the RMS force on the nudged elastic band is less than a predetermined value.

The image with the highest potential energy is then taken as a starting configuration for an EF/BFGS transition state search. It is often the case that the transition state that we find is connected to neither or only one starting minimum via steepest-descent paths. This is especially true if the separation of the end points is greater than the equilibrium pair separation. We therefore use Wales' CONNECT algorithm to generate a connected path of minima and transition states between the two minima.[162] This

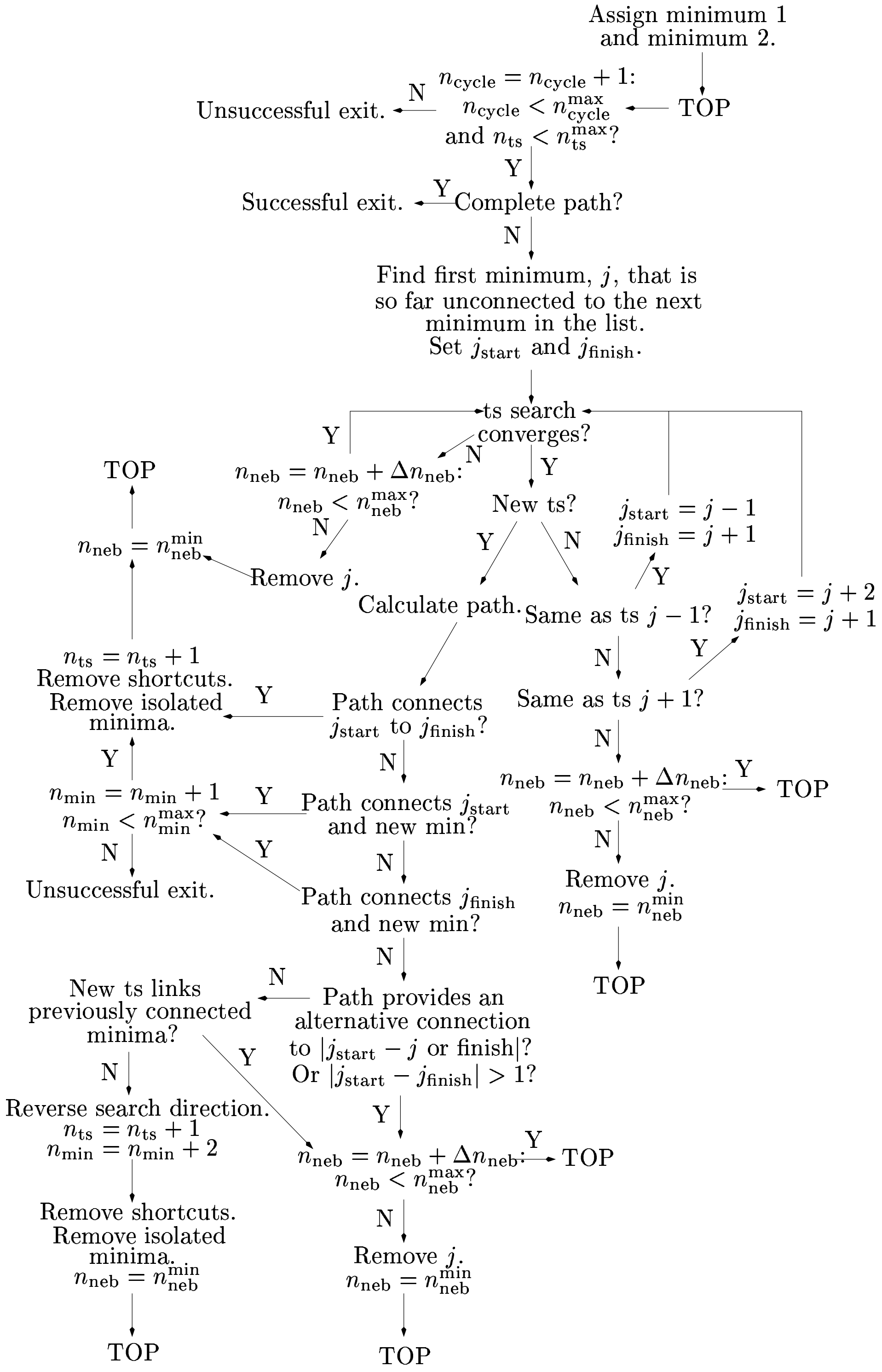

Figure 2.1: Schematic view of the algorithm used for double-ended searches to connect pairs of local minima via combined NEB and hybrid eigenvector-following calculations. Transition state j connects minima j and $j+1$ in the path. Taken from Ref 161, with permission.

scheme is illustrated in Figure 2.1. Essentially, the aim of algorithm is to find transition states connecting pairs of minima in an ordered list, adding new minima if necessary. To calculate the minimum displacement between minima in a bulk system, we simply translate the centres of mass to the origin. When two minima and the intervening transition state are inserted in the list, they are ordered according to the shortest displacement to a neighbouring minimum. Shortcuts—pairs of minima with an overall separation of less than $0.001\,\sigma$—are removed from the list, as are minima that prove too difficult to connect to their neighbours. We can also use the CONNECT algorithm as another method of increasing the number of transition states connected to a given starting minimum. The starting coordinates are perturbed and then minimised to generate a second minimum. A pathway is then generated linking the pair of minima. If desired, the CONNECT run can be halted as soon as there is a transition state linked to the first minimum.

2.1.3 FINDING STATIONARY POINTS ON ENTHALPY SURFACES

The constant volume PES of a system with N atoms and periodic boundary conditions is a $3N+1$ dimensional hypersurface. In constant pressure simulations, the dimensions of the simulation supercell must be allowed to vary independently, and so there are three more degrees of freedom. Rather than study the potential energy surface, we now have an enthalpy surface, where the enthalpy, H, is defined by $H = E + PV$. In our models, the pressure, P is a parameter we define, and V is the volume of the simulation supercell. Our pressure-density dependence is not exactly the same as for isobaric MD studies,[163–165] nor do we expect it to be. Obviously, the minima and transition states are more compact than vibrationally excited instantaneous MD configurations. Nevertheless, we expect our results to reveal the underlying structural rearrangement mechanisms, and the effect of increasing pressure and density.

We divided the degrees of freedom into $3N$-dimensional 'atomic coordinate space', and 3-dimensional 'box length space'. We then successively optimised the atomic coordinates and the box lengths. We minimised the enthalpy with respect to the box lengths using eigenvector-following (§2.1.1), with numerical derivatives of the energy.

The enthalpy gradients with respect to the box lengths were often very large, and we found that the searches converged more quickly if several steps were taken in box length space between each step in atomic coordinate space, to converge the gradient with respect to each box length to less than $10^{-3}\,\epsilon\sigma^{-1}$. $10^{-3}\,\epsilon\sigma^{-1}$ was also the convergence criterion for the gradient with respect to the box lengths at a stationary point. Analytic derivatives of the enthalpy were also programmed (see Appendix), but did not speed up the calculations significantly. All the other parameters and convergence criteria were exactly the same as at constant volume.

Our method of optimising the structure taking account of the pressure differs from that used by Kopsias and Theodorou.[145] They found stationary points keeping the box lengths constant, and then optimised the latter quantities without changing the structure. It is conceivable that minima and transition states found using such a technique would not be linked by steepest-descent paths for which the box dimensions are fully optimised, as the convergence of the two spaces defined above takes place in two distinct stages. This is why the box lengths are optimised between each step in configuration space in our calculations.

2.1.4 SAMPLING THE POTENTIAL ENERGY OR ENTHALPY SURFACES

Various approaches have been described for systematically exploring a PES by moving between local minima.[138, 153, 166–168] Starting from a known minimum we conducted transition state searches using hybrid eigenvector-following and the scheme based on hard-sphere moves described in §2.1.1. For each new transition state the corresponding pathway was calculated. If neither of the connected minima corresponded to the minimum from which the transition state was found, the path was discarded. New connected minima were added to the database and were subsequently used as starting points for transition state searches in the same way, in order of increasing energy. The minima in the set are therefore also connected, i.e. any pair can be interconverted via a series of transition states from the same database. This condition is important for dynamical studies, and for the construction of disconnectivity graphs (§2.3).

We use three sampling schemes in the current work: which we denote SS1, SS2, and SS3.

1. SS1 uses up to forty transition state searches per minimum, accepting downhill moves to new connected minima. We used this sampling scheme to produce databases of essentially crystalline minima for the model glasses studied, mainly to generate crystalline vibrational densities of states (VDOS) for comparison with our amorphous results.

2. SS2 provides a broader overview of a wide range of configuration space, carrying out only eight transition state searches per minimum, and like SS1 accepts moves to lower lying minima.
3. SS3 carries out 400 transition state searches per minimum, starting from a new minimum only if all 400 searches are complete. Thus, SS3 probes a much smaller region of configuration space more thoroughly than either SS1 or SS2.

Comparison of these alternative sampling schemes enables us to ascertain whether the barrier distributions obtained are sensitive to the sampling technique.

The choice of starting minimum, and the criteria that we employ to select subsequent starting minima may well affect the results we obtain. In Chapter 5 we compare results obtained for different initial configurations and sampling schemes.

Attempts to generate databases using SS1 and SS3 from starting minima with residual regions of crystalline structure inevitably led to the crystal being located within the first few hundred minima. This is the expected behaviour for homogeneous Lennard-Jones systems,[169] and the disconnectivity graphs illustrated in §3.1 show that the crystal is readily located once a critical nucleus is present.

2.1.5 TRANSITION STATE SEARCH PARAMETERS

The results of a number of transition state searches from a test set of minima did not vary significantly within a fairly broad range of parameters, and so the choice of parameter set was dictated by computational efficiency. In the hybrid EF/BFGS transition state searches, we allowed up to 100 iterations in the calculation of the smallest Hessian eigenvalue; up to 100 iterations in the calculation of the largest eigenvalue; 10 BFGS steps in the subspace minimisation before the smallest eigenvalue had converged and 100 thereafter. The smallest eigenvalue was deemed to have converged when it changed by less than 0.01% between successive steps. Initial diagonal elements of the inverse Hessian were set to $0.1\,\sigma^2\epsilon^{-1}$.

2.2 GLOBAL OPTIMISATION

We use the 'basin-hopping' approach of Wales and Doye[170] to search for the lowest energy (global) minimum on the PES of the binary Lennard-Jones (BLJ) system (§2.4.1, Chapter 3). This method, which is based on the Monte Carlo plus minimisation method of Li and Scheraga[171, 172] has been used with considerable success in studies of atomic clusters and model polypeptides.[153] A transformed energy landscape is considered

$$\tilde{E}(\mathbf{X}) = \min\{E(\mathbf{X})\}, \tag{2.18}$$

where $\mathbf{X}$ is the $3N$-dimensional vector of atomic coordinates, and min indicates that an energy minimisation is carried out, starting at $\mathbf{X}$. Thus each basin of attraction on the PES is transformed into a plateau, with transformed energy corresponding to the local minimum reached by energy minimisation. For minima on the PES, $\tilde{E}(\mathbf{X}) = E(\mathbf{X})$.

The transformed surface is then searched, using Monte Carlo sampling at a fixed temperature. The current coordinates are perturbed to produce a new configuration. This move is accepted if this perturbation lowers the energy, or if $\exp\left[(E_{old} - E_{new}/k_{\mathrm{B}}T\right]$ is greater than a random number drawn from the interval $[0, 1]$. Better results are obtained if the structure is reset to that of the current local minimum at each step.[153]

2.3 DISCONNECTIVITY GRAPHS

Becker and Karplus invented the 'disconnectivity tree' for illustrating the topology of potential energy surfaces,[174] and the idea has been used extensively by Wales and coworkers.[153, 175] Minima are grouped into disjoint sets, known as superbasins. Superbasins are defined for given energies, E, by the mutually accessible minima at that energy. Energy increases on the vertical scale, and superbasins are then denoted in the disconnectivity graph by nodes, from which lines either go down to nodes representing lower energy superbasins, or terminate at local minima. The horizontal scale is arbitrary. Although the disconnectivity tree is extremely useful for illustrating multidimensional potential energy surfaces, for large numbers of minima it often contains too much information, and producing the diagram is laborious. Another method of illustrating multi-dimensional PES's is to show sequences of connected minima with monotonically decreasing energy.[153, 176, 177] A set of such sequences leading to the same minimum defines a set of minima generally known as a monotonic sequence basin (MSB). The barriers between minima in an MSB give some indication of how efficient a 'structure seeker' a system is, although there is little global information about the form of the PES. Some disconnectivity trees for one-dimensional potential energy surfaces are illustrated in Figure 2.2. In describing these landscapes, we borrow the term 'funnel'

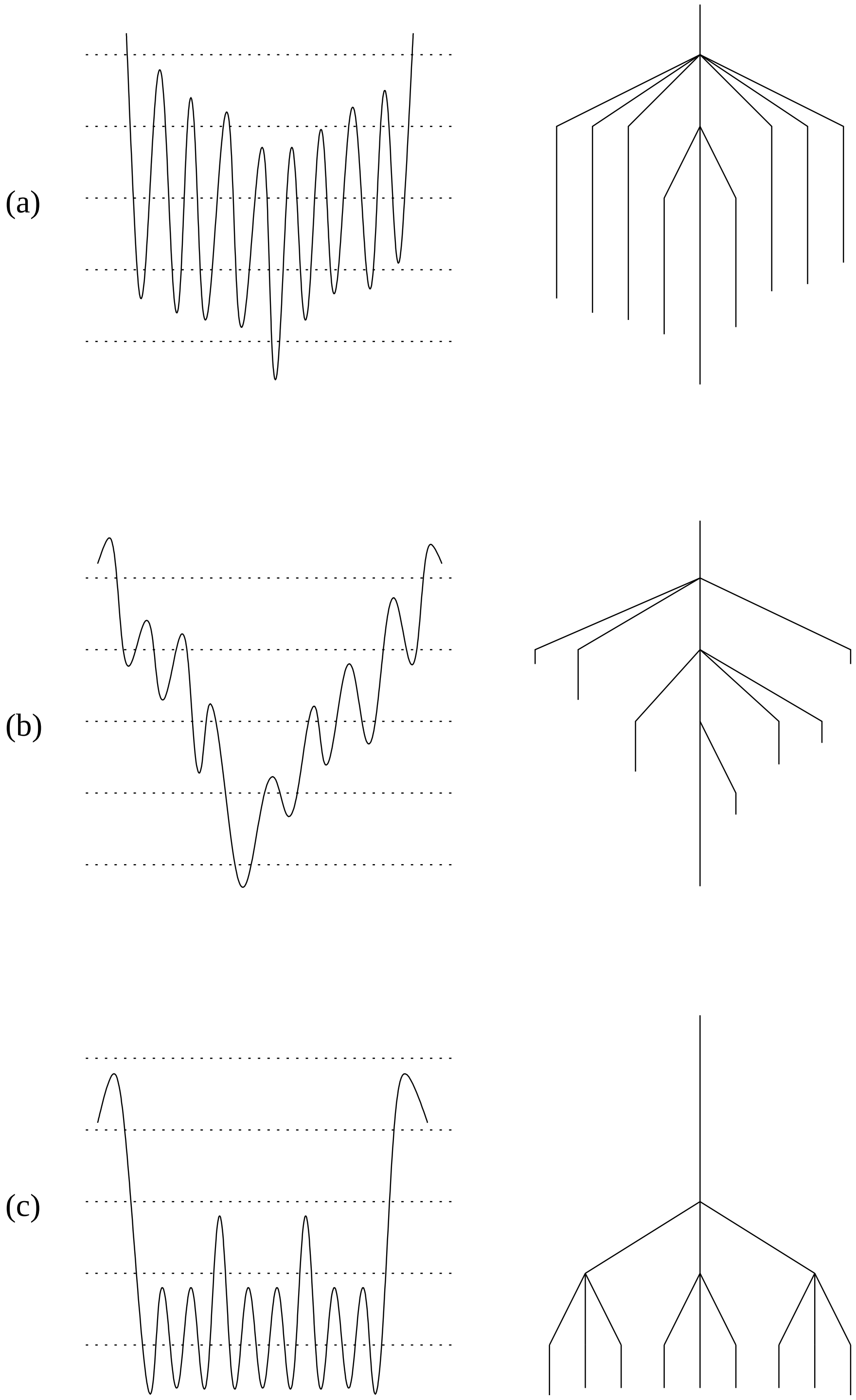

Figure 2.2: Pictorial correspondence between the PES and the disconnectivity graph for three different energy lanscapes. **(a)** The 'weeping willow' results from a gentle funnel with large barriers. **(b)** The 'palm tree' results from a steeper funnel with lower barriers. **(c)** The 'banyan tree' results from a rough landscape. (Reproduced with permission from Ref 173)

from protein-folding literature to describe a set of kinetically convergent pathways that lead to a single low-lying minimum.[178] In the present work this minimum might be the crystalline structure of the glass former, or a very low energy amorphous minimum.

Disconnectivity graphs with several thousand minima often become rather cluttered and their meaning can be thus obscured. Several methods of simplifying the graphs have been developed: plotting only the lowest n minima;[174] representing energetically and structurally similar minima by a single node;[179] or including only those minima that lie at the bottom of MSBs.[180] Alternatively, minima that are only connected to one other minimum can be removed.[181] The method that we use, when simplification is necessary, is due to Mortenson.[173,182] This method uses canonical rate constants between pairs of minima, calculated by, for example, Rice-Ramsberger-Kassel-Marcus (RRKM) theory,[183–185] at a specified temperature, T. A threshold rate constant is then selected, and each pair of minima connected by a single transition state is considered in turn. If the rate constants in both directions exceed the threshold rate, then the line corresponding to the higher energy minimum is removed: this pair of minima are said to have been grouped together. Finally, we consider pairs of minima that have not been grouped together, but are linked by a 'downhill' rate greater than the threshold rate. In this case, the line corresponding to the higher energy group is removed. Thus, we simplify the disconnectivity graph according to the intuitive notions that minima separated by low barriers in both directions are in equilibrium, and high energy minima can be ignored if they relax rapidly to a lower energy structure.

The value of the threshold rate is chosen so that the number of branches of the graph is significantly reduced, without losing the key components of its structure.

2.4 POTENTIALS

Four systems are considered in the present work, as detailed below. In each case we adopt the natural reduced unit system, where energy is measured in ϵ and length in σ (ϵ_{AA} and σ_{AA} for binary Lennard-Jones). The corresponding reduced unit of time is $\sqrt{m\sigma^2/\epsilon}$, and unit masses were also employed throughout. In each case the energy unit corresponds to the pair well depth and $2^{1/6}\sigma$ corresponds to the pair equilibrium separation (for A–A interactions in the binary Lennard-Jones system). Reduced temperatures are defined by $k_{\mathrm{B}}T/\epsilon$ and the unit of frequency is $\sqrt{\epsilon/m\sigma^2}$. Since supercells of different sizes are used for different systems the energies of local minima will be reported in ϵ per atom. However, barrier heights, which are not expected to be extensive quantities, will be reported in ϵ per supercell.

2.4.1 BINARY, UNIT DENSITY AND RELAXED LENNARD-JONES SOLIDS

The Lennard-Jones (LJ) potential[186] for two atoms separated by a distance r is given by:

$$V(r) = 4\epsilon\left[\left(\frac{\sigma}{r}\right)^{12} - \left(\frac{\sigma}{r}\right)^{6}\right]. \tag{2.19}$$

where ϵ is the depth of the potential energy well, and $2^{1/6}\sigma$ is the pair equilibrium separation.

Our unit density Lennard-Jones system (ULJ) contained 256 atoms, and has hexagonal and cubic close-packed crystalline minima.[187] The relaxed Lennard-Jones (RLJ) system has a box length optimised for the face-centred-cubic (fcc) solid with a number density of $0.93\,\sigma^{-3}$, indicating that the ULJ crystal corresponds to a large negative pressure. The cutoff employed for both these systems was 3.17σ.

We also studied the properties of the binary Lennard-Jones system, with parameters first used by Kob and Andersen in 1994,[94] although Stillinger and Weber had previously employed a similar potential in simulations of the metallic glass $\mathrm{Ni_{0.8}P_{0.2}}$.[188] Kob and Andersen modified a parameter set used by Ernst et al.[189] because they found that this binary system, which had previously been used in studies of the glass transition, crystallised at low temperatures.

The system consists of 80% A atoms, and 20% B atoms, with parameters $\sigma_{\mathrm{AA}} = 1.0$, $\sigma_{\mathrm{AB}} = 0.8$, $\sigma_{\mathrm{BB}} = 0.88$, $\epsilon_{\mathrm{AA}} = 1.00$, $\epsilon_{\mathrm{AB}} = 1.5$, and $\epsilon_{\mathrm{BB}} = 0.5$. The units of distance and energy used are σ_{AA} and ϵ_{AA}. Periodic boundary conditions are used, and the most popular number density for constant-volume simulations is $1.2\,\sigma_{\mathrm{AA}}^{-3}$, which we use here. It is worth noting that $\sigma_{\mathrm{AB}} \neq (\sigma_{\mathrm{AA}} + \sigma_{\mathrm{BB}})/2$—a property which one might expect could lead to anomalous behaviour.

In Chapter 3 we present results for global optimisation of 60-, 256- and 320-atom supercells of the BLJ system, and Chapter 4 contains databases of amorphous minima and transition states of 256-atom homogeneous and binary Lennard-Jones systems.

We used a quadratic shifting technique, after Stoddard and Ford,[190] to ensure that the energy and its first derivatives were continuous at the cutoff. The adapted potential, with a cutoff of r_c, is given by:

$$\begin{aligned} V(r) = \; & 4\epsilon \left\{ \left[(\sigma/r)^{12} - (\sigma/r)^{6} \right] \right. \\ & + \left[6\,(\sigma/r_c)^{12} - 3\,(\sigma/r_c)^{6} \right] (r/r_c)^2 \\ & \left. -7\,(\sigma/r_c)^{12} + 4\,(\sigma/r_c)^{6} \right\} , \end{aligned} \tag{2.20}$$

for $r \leq r_c$. Obviously $V(r) = 0$ for $r > r_c$. The shifting function affects the position and depth of the potential well, which can no longer be found analytically.* The choice of cutoff distance can dramatically affect the depth of the potential energy well. We used a cutoff of $3.17\,\sigma$ for the homogeneous systems, which leads to a potential well 1.43 % shallower than that of the standard Lennard-Jones potential. In the binary systems, we used cutoffs of $2.5\,\sigma_{\alpha\beta}$ (256- and 320-atom systems) and $1.842\,\sigma_{\alpha\beta}$ (60 atoms), which have a more significant impact, decreasing the depth of the well by 5.5 % and 28.27 %, respectively. The shortening of the equilibrium bond length with decreasing cutoff is less significant: the three cutoffs of $3.17\,\sigma$, $2.5\,\sigma_{\alpha\beta}$ and $1.842\,\sigma_{\alpha\beta}$ gave values 0.004 %, 0.03 % and 0.31 % longer, respectively.

Most other researchers, notably Kob and Andersen,[94] use a constant to shift the function, which makes only the energy continuous at the cutoff. This shift does not affect the equilibrium pair separation, but makes the potential well shallower by 10.0%, 1.6% and 0.4% for cutoffs of $1.842\,\sigma_{\alpha\beta}$, $2.5\,\sigma$, and $3.17\,\sigma_{\alpha\beta}$, respectively. Therefore, the energies of the low-lying minima we have obtained will often appear to be high when compared to some other authors' results. In Chapter 3, I calculate energies for both the Kob-Andersen (KA) and Stoddard-Ford (SF) cutoffs, for comparison.

2.4.2 THE STILLINGER-WEBER (SW) SILICON POTENTIAL

Amorphous silicon, *a*–Si, has provoked much research, owing to its technological importance as a semiconductor. Experimentally, it is impossible to quench *a*–Si sufficiently rapidly from the melt to form the amorphous solid.[191] Instead, *a*–Si is formed as a thin film, either in its pure form, or doped with hydrogen. Pure *a*–Si is formed using physical vapour deposition (PVD): crystalline silicon is heated to evaporate at as low a

---

[*] Turning points of the energy now satisfy the equality $r^{14}(2\sigma^6/r_c^{14} - 1/r_c^8) + r^6 - 2\sigma^2 = 0$, which can be factorised to give $(r^{*2} - 1)[(2\sigma^6 - r_c^6)(r^{*12} + r^{*10} + r^{*8} + r^{*6}) + 2\sigma^6(r^{*4} + r^{*2} + 1)]$, where $r* = r/r_c$. This result yields the maximum at $r = r_c$, but the equation cannot be factorised further to give an analytical expression for the equilibrium separation.

temperature as possible, and the film is grown on a substrate kept at low temperature. Hydrogen-doped *a*–Si (*a*–Si:H) is prepared with a variety of methods, of which the most important are chemical vapour deposition (CVD) and reactive sputtering. CVD forms *a*–Si on a substrate kept at $200-300\,^\circ$ C from silane ($\mathrm{SiH_4}$) vapour. A number of possible methods can be used to excite the $\mathrm{SiH_4}$ vapour, generating free radicals that react to form the *a*–Si:H thin film. In reactive sputtering, a crystalline silicon target is bombarded with a plasma of argon and hydrogen, with the *a*–Si:H forming on a glass substrate kept at $200-300\,^\circ$C. This technique has the advantage that the hydrogen content can be controlled with great accuracy by varying the $\mathrm{Ar/H_2}$ mixture.

Theoretically, both the amorphous and crystalline forms of silicon have been simulated using ab initio electronic structure calculations, and numerous empirical potentials. Ab initio calculations are currently computationally too expensive for our purposes, and so we must use an empirical potential function. Recent reviews have shown that none of the available empirical potentials capture all the physics of experimental or ab initio silicon,[192–194] but among the best and most commonly used is the Stillinger-Weber potential.[195] The system has been studied extensively, in particular using MD[164,165,196] and ART[138,139,197,198] and so is an appropriate choice for us to study using our techniques.

The SW silicon potential has two- and three-body contributions:

$$\nu_2(r_{ij}) = \epsilon f_2\left(\frac{r_{ij}}{\sigma}\right), \quad \nu_3(r_i, r_j, r_k) = \epsilon f_3(\mathbf{r}_i, \mathbf{r}_j, \mathbf{r}_k). \tag{2.21}$$

ϵ and σ are chosen so that the minimum value of f_2 is $f_2(2^{1/6}) = -1$, and f_2 and f_3 are given by:

$$f_2(r) = \begin{cases} A(Br^{-p} - r^{-q})\exp(r-a)^{-1}, & r < a, \\ 0, & 1 \geq a, \end{cases} \tag{2.22}$$

$$f_3(\mathbf{r}_i, \mathbf{r}_j, \mathbf{r}_k) = h(r_{ij}, r_{jk}, \theta_{jik}) + h(r_{ji}, r_{jk}, \theta_{ijk}) + h(r_{ki}, r_{kj}, \theta_{ikj}), \tag{2.23}$$

$$h(r_{ij}, r_{jk}, \theta_{jik}) = \lambda \exp[\gamma(r_{ij}-a)^{-1} + \gamma(r_{ik}-a)^{-1}](\cos\theta_{ijk} + \frac{1}{3})^2. \tag{2.24}$$

Stillinger and Weber[195] found that the best fit parameters for the diamond structure were $A = 7.050$, $B = 0.6022$, $p = 4$, $q = 0$, $a = 1.80$, $\lambda = 21.0$, $\gamma = 1.20$, $\sigma = 2.0951\,\text{Å}$ and $\epsilon = 2.1682\,\text{eV}$. In the diamond structure all the nearest neighbour bond angles are tetrahedral, so all the cosine terms in the three-body part are equal to $-1/3$, and the sum of the three-body terms vanishes. Hence the effect of the three-body term is to encourage tetrahedral coordination. The melting point is estimated to be $k_{\text{B}}T/\epsilon \approx 0.080$, slightly higher than the experimental value, which is, in reduced units, $k_{\text{B}}T/\epsilon = 0.067$. The optimum number density for the crystal is $0.459\,\sigma^{-3}$, leading to a box length for the 216 atom supercell used here of $7.776643\,\sigma$. The potential has a built-in cutoff at $a = 1.80\,\sigma$.

Despite its simplicity, the SW potential has been found to reproduce the structural properties of silicon rather well. This is not just the case for the diamond structure, but for all of its experimentally observed condensed phases.

The phase diagram of SW Si at zero pressure was calculated using MD by Broughton and Li.[196] They successfully supercooled the liquid, and found a density maximum at $k_{\text{B}}T/\epsilon \approx 0.05$. At $k_{\text{B}}\epsilon \approx 0.04$, the diffusivity practically dropped to zero, signalling the glass transition on the timescale of their MD simulations. The structure of the glass formed, however was not the same as experimental *a*–Si, or that of other models.[199] An Arrhenius plot of the diffusivity in the liquid showed that the activation energy was essentially constant at $0.2\,\epsilon$, down to its apparent glass transition at $k_{\text{B}}T/\epsilon \approx 0.04$. Thus, these simulations suggested that silicon is a strong liquid according to Angell's classification scheme.

Luedtke and Landman[164] studied further the inability of the melt to form *a*–Si directly. They developed a scheme for preparing well relaxed *a*–Si using constant pressure MD simulation. They used a multi-stage cooling process from the equilibrium melt, and encouraged tetrahedral coordination in the cooling phase by increasing the value of λ by 50%. In a later paper, they managed to show that previous attempts to prepare *a*–Si directly from the melt failed because the quench rates employed were too fast.[165] It appears that there is a significant energy barrier to formation of the amorphous phase directly from the melt in MD simulations because the liquid and amorphous phases have very different structures. The liquid is 'metallic' and more dense than the crystal because the open network structure collapses. This difference is illustrated well by the change in the distribution of nearest neighbour coordination numbers: Luedtke and Landman found that the majority of atoms had five nearest neighbours (47%), while the rest were mainly four- or six-fold coordinated (29% and 19%, respectively). The amorphous solid was mainly four-fold coordinated (89%) with the rest five-fold (11%), conforming to the model of a continuous random network (CRN). The amorphous structure they obtained was similar to that found by Wooten, Winer and Weaire (WWW),[199] who successfully modelled the experimental structure of *a*–Si by successively swapping the nearest neighbours of pairs of bonded atoms and partially optimising the structure. Luedtke and Landman also prepared a 'glass', by following the same multistage cooling process, but without increasing the three-body term.[164] The distribution of coordination numbers was intermediate between the amorphous solid and the liquid: 41%, 52% and 7% of atoms 4, 5, and 6 coordinated, respectively.

The distinction between the 'glass' and 'amorphous solid' may seem a little tenuous, but is useful inasmuch as the former is essentially the kinetically arrested liquid, while the latter is a quite distinct phase. Surprisingly, the third peak of the crystal RDF is entirely absent from the amorphous solid, glass and liquid.

The amorphous solid melts when heated, undergoing what appears to be a first-order transition. In MD sharp changes in the density and total energy per particle are observed.[164,165] Angell has recently pointed out that this transition is better described as one between two liquids, on the assumption that the diffusivity of the amorphous solid is greater than that of the diamond structure at the same temperature.[200] Experiments by Ansell et al.[201] have supported the existence of this transition and Angell's suggestion that it is between two liquids.

There are striking similarities between the phenomenologies of silicon and water:[202–204] in particular, both substances exhibit a sharply defined density maximum with respect to temperature, and there is considerable indirect evidence that water too exhibits a polyamorphic transition.[205] As discussed more thoroughly in §1.1.6, the presence of this first order transition and the apparent lack of the boson peak and two-level systems[206] (§1.1.6) has led Angell to suggest that well-relaxed *a*–Si may be an example of a class of glass-formers with very low residual entropy, approaching the ideal glass state.[38,207]

Barkema, Mousseau and co-workers have studied the potential energy landscape of amorphous SW silicon in some detail, using a method similar to ours, the activation-relaxation technique (ART)[138,139,197,198] the principles of which I outlined in §1.3.3. They catalogued over 8000 ART 'events', grouping them into three broad classes: 'perfect', in which the coordination numbers of all atoms involved remained the same, 'conserved events' which corresponded to defect diffusion, and finally defect coordination/annihilation events.[139,168] Creation/annihilation events were the most numerous (5325), followed by conserved (1979) and perfect (802).

85% of the 'perfect' events corresponded to the WWW nearest-neighbour exchange, with barriers around 4 eV, with a spread of 2 eV. The barriers to 'concerted exchange' (CE), in which a pair of nearest neighbours swap positions, were higher, peaking at 5.8 eV, with a spread from 3.6 eV to 12 eV. The CE mechanism was proposed by Pandey as a possible diffusion mechanism in the crystal.[208] Comparison with the nudged elastic band methods of Jonsson et al, described in §2.1.2, suggested that single ART events corresponded to pathways containing a number of transition states.[198] The energy barriers obtained using the nudged elastic band method and ART varied by as much as ±2 eV.

APPENDIX: ANALYTIC DERIVATIVES OF THE ENTHALPY WITH RESPECT TO THE BOX LENGTH

We follow Parinello and Rahman,[209] and allow the three box lengths of the supercell to vary independently, while keeping the supercell orthorhombic. Derivatives of the enthalpy with respect to the dimensions of the supercell can be derived using scaled or unscaled atomic coordinates.

SCALED COORDINATES

We define the scaled position vector of atom i in terms of its unscaled coordinates, (x_i, y_i, z_i), and the box lengths, (L_x, L_y, L_z), as follows:

$$(\bar{x}_i, \bar{y}_i, \bar{z}_i) = (x_i/L_x, y_i/L_y, z_i/L_z). \tag{2.25}$$

The distance between a pair of atoms, r_{ij}, is given by:

$$r_{ij}^2 = \Delta x_{ij}^2 + \Delta y_{ij}^2 + \Delta z_{ij}^2, \tag{2.26}$$

where $\Delta x_{ij} = x_i - x_j - L_x \,\mathrm{NINT}\,[(x_i - x_j)/L_x]$. The function $\mathrm{NINT}\,[u] = n$, where n is an integer and $n - 0.5 \leq u < n + 0.5$: i.e. NINT yields the nearest integer to u. The term containing the NINT function is present to ensure that we follow the minimum image convention. If $\Delta \bar{x}_{ij}$ is defined similarly then

$$r_{ij}^2 = \Delta \bar{x}_{ij}^2 L_x^2 + \Delta \bar{y}_{ij}^2 L_y^2 + \Delta \bar{z}_{ij}^2 L_z^2. \tag{2.27}$$

In order to obtain the derivatives of the enthalpy with respect to the box lengths, we have to treat $\mathrm{NINT}\,[(x_i - x_j)/L_x]$ as a constant. Thus $\partial r_{ij}/\partial L_x = L_x \Delta \bar{x}_{ij}^2 / r_{ij}$. The enthalpy, H, is given by $H = E + PV$, where E is the potential energy, P the pressure and $V = L_x L_y L_z$, the volume of the simulation supercell. Using the relation that $\partial E/\partial L_x = (\partial E/\partial r_{ij})(\partial r_{ij}/\partial L_x)$, we obtain:

$$\frac{\partial H}{\partial L_x} = \frac{\partial E}{\partial L_x} + P L_y L_z = L_x \sum_{i<j} \frac{\partial E(r_{ij})}{\partial r_{ij}} \frac{\Delta \bar{x}_{ij}^2}{r_{ij}} + P L_y L_z \tag{2.28}$$

and the second derivatives are:

$$\frac{\partial^2 H}{\partial L_x^2} = \sum_{i<j} \left\{ \left(\frac{\partial^2 E}{\partial r_{ij}^2} - \frac{1}{r_{ij}} \frac{\partial E}{\partial r_{ij}} \right) \frac{\Delta \bar{x}_{ij}^4 L_x^2}{r_{ij}^2} + \frac{\partial E}{\partial r_{ij}} \frac{\Delta \bar{x}_{ij}^2}{r_{ij}} \right\}, \tag{2.29}$$

and

$$\frac{\partial^2 H}{\partial L_x L_y} = P L_z + \sum_{i<j} \left(\frac{\partial^2 E}{\partial r_{ij}^2} - \frac{1}{r_{ij}} \frac{\partial E}{\partial r_{ij}} \right) \frac{L_x L_y \Delta \bar{x}_{ij}^2 \Delta \bar{y}_{ij}^2}{r_{ij}^2}. \tag{2.30}$$

UNSCALED COORDINATES

The derivation is similar if we use unscaled coordinates, (x_i, y_i, z_i). $\Delta x_{ij} = x_i - x_j - L_x \, \mathrm{NINT} \, [(x_i - x_j)/L_x]$, and so $\partial \Delta x_{ij} / \partial L_x = -\,\mathrm{NINT} \, [(x_i - x_j)/L_x]$, and $\partial r_{ij} / \partial \Delta x_{ij} = \Delta x_{ij} / r_{ij}$. Hence:

$$\frac{\partial H}{\partial L_x} = -\sum_{i<j} \frac{\partial E}{\partial r_{ij}} \frac{\Delta x_{ij}}{r_{ij}} \, \mathrm{NINT} \left[\frac{x_i - x_j}{L_x} \right] + P L_y L_z, \tag{2.31}$$

and the second derivatives are:

$$\frac{\partial^2 H}{\partial L_x^2} = \sum_{i<j} \left\{ \left[\left(\frac{\partial^2 E}{\partial r_{ij}^2} - \frac{1}{r_{ij}} \frac{\partial E}{\partial r_{ij}} \right) \frac{\Delta x_{ij}}{r_{ij}} + \frac{\partial E}{\partial r_{ij}} \frac{1}{r_{ij}} \right] \left(\mathrm{NINT} \left[\frac{x_i - x_j}{L_x} \right] \right)^2 \right\}, \tag{2.32}$$

and

$$\frac{\partial^2 H}{\partial L_x L_y} = P L_z + \sum_{i<j} \left\{ \left(\frac{\partial^2 E}{\partial r_{ij}^2} - \frac{1}{r_{ij}} \frac{\partial E}{\partial r_{ij}} \right) \frac{\Delta x_{ij} \Delta y_{ij}}{r_{ij}^2} \, \mathrm{NINT} \left[\frac{x_i - x_j}{L_x} \right] \mathrm{NINT} \left[\frac{y_i - y_j}{L_y} \right] \right\}. \tag{2.33}$$

These two sets of derivatives are not, in general, the same. The difference between the two different first derivatives is given by:

$$\left(\frac{\partial H}{\partial L_x} \right)_{sc} - \left(\frac{\partial H}{\partial L_x} \right)_{unsc} = \sum_{i<j} \frac{\partial E}{\partial r_{ij}} \frac{\Delta x_{ij}}{r_{ij}} \left(\frac{x_i - x_j}{L_x} \right) = \frac{1}{2} \sum_i \sum_{j \neq i} \frac{\partial E}{\partial r_{ij}} \frac{\Delta x_{ij}}{r_{ij}} \left(\frac{x_i - x_j}{L_x} \right). \tag{2.34}$$

We then use the relations $(\partial \Delta x_{ij} / \partial x_i) = 1$ and $\partial r_{ij} / \partial \Delta x_{ij} = \Delta x_{ij} / r_{ij}$ to obtain:

$$\left(\frac{\partial E}{\partial x_i}\right)_{\vec{L}} = \sum_{j\neq i} \frac{\partial E}{\partial r_{ij}} \frac{\Delta x_{ij}}{\partial r_{ij}} \tag{2.35}$$

Separating equation 2.34 into two sums, and substituting in equation 2.35, we obtain:

$$\begin{aligned}\left(\frac{\partial H}{\partial L_x}\right)_{sc} - \left(\frac{\partial H}{\partial L_x}\right)_{unsc} &= \frac{1}{2}\sum_i \frac{x_i}{L_x}\left(\frac{\partial E}{\partial x_i}\right)_{\vec{L}} + \frac{1}{2}\sum_j \frac{x_j}{L_x}\left(\frac{\partial E}{\partial x_j}\right)_{\vec{L}} &(2.36)\\ &= \frac{\vec{x}.\vec{\nabla}E}{L_x} &(2.37)\end{aligned}$$

where $\vec{x}$ is the vector $(x_1, 0, 0, x_2, 0, \dots)$. Thus the overall difference between the box length gradients calculated using scaled and unscaled coordinates is given by the vector:

$$\left(\frac{\vec{x}.\vec{\nabla}E}{L_x}, \frac{\vec{y}.\vec{\nabla}E}{L_y}, \frac{\vec{z}.\vec{\nabla}E}{L_z}\right) \tag{2.38}$$

At a stationary point with respect to the atomic configuration, $\vec{\nabla}E = \vec{0}$ by definition, and so the gradient of the energy with respect to the box dimensions is exactly equal for derivatives calculated with both scaled and unscaled coordinates. We used a test set of ten different starting configurations to search for transition states and subsequently generate paths, for numerical derivatives and analytic derivatives using both scaled and unscaled coordinates. We found the same stationary points in each case, but the stationary point searches converged fastest with the numerical derivatives.

3

GLOBAL OPTIMISATION AND CRYSTALLINE REGIONS OF CONFIGURATION SPACE

We began our investigation of the potential energy surfaces of our chosen model glass formers by generating databases of stationary points for crystalline and nearly crystalline regions of configuration space. We generated these databases in order to compare their properties with those of disordered minima and transition states, which we present in the next chapter.

We were particularly interested in the possibility of the existence of a crystal structure for the binary Lennard-Jones system (§2.4.1). At the time, no crystalline structure had been reported, despite the popularity of the system as a model glass former. As the crystal structure had not been found, the degree of supercooling in MD simulations was unknown.[98, 128, 131, 210–216]

3.1 THE UNIT DENSITY LENNARD-JONES AND STILLINGER-WEBER SYSTEMS

The global minima for the unit density homogeneous Lennard-Jones and Stillinger-Weber systems are well known. The Lennard-Jones system forms both hexagonal- and cubic-close-packed crystals, and the global minimum is face-centred-cubic (fcc) when the system is in a cubic supercell of fixed box lengths and angles. The parameters of the SW Si potential were optimised for the diamond structure, which is the global minimum.

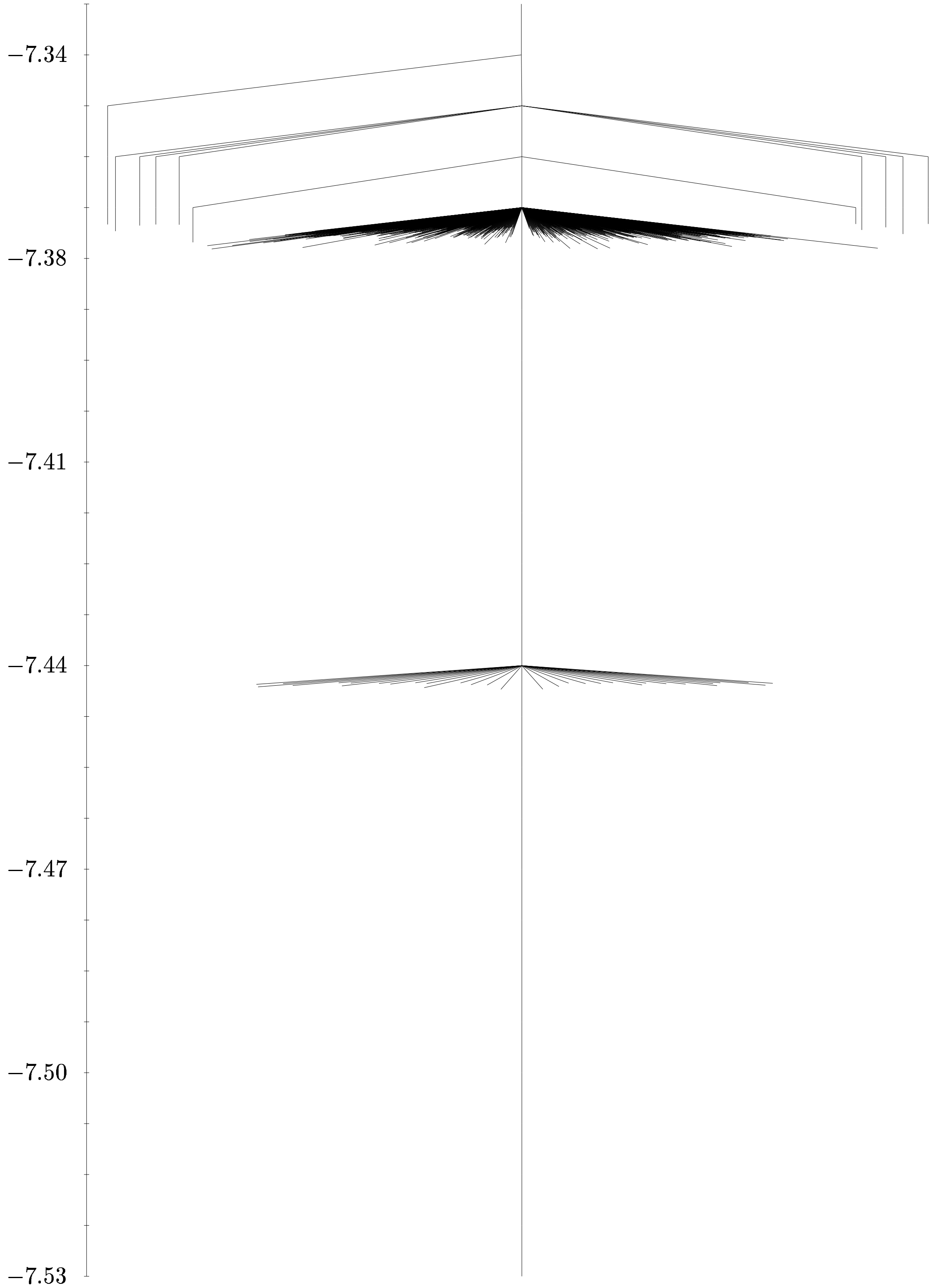

Figure 3.1: Disconnectivity graph containing the lowest 500 minima for the unit density Lennard-Jones system ULJ(x). Energies are in ϵ per atom.

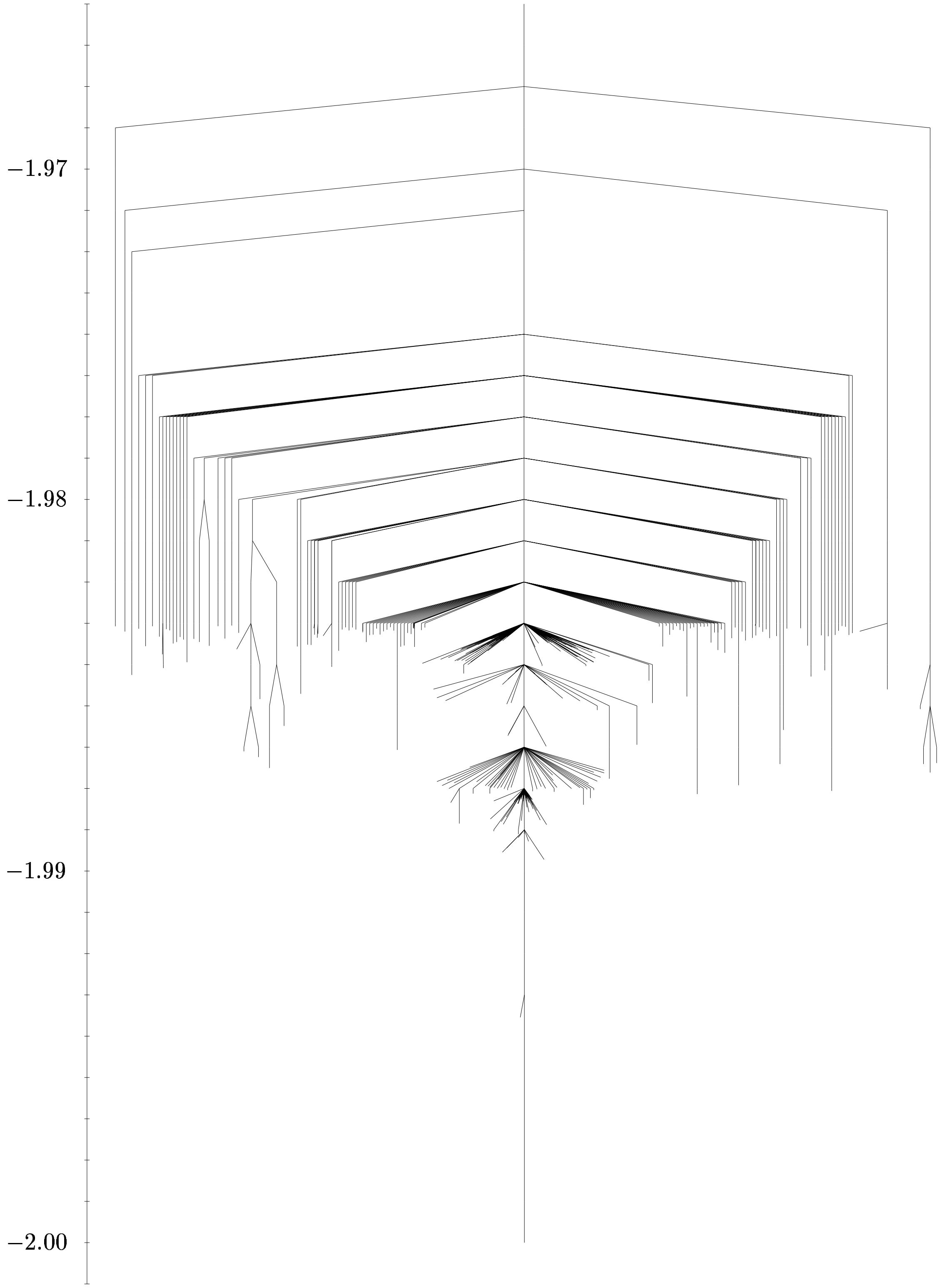

Figure 3.2: Disconnectivity graph containing the lowest 150 minima for the Stillinger-Weber silicon system SW(x). Energies are in ϵ per atom.

Starting from these known global minima, we generated databases of 10000 transition states, using sampling scheme SS1 from §2.1.4 (40 transition state searches per minimum), and the parameter set outlined in §2.1.5. The databases thus generated were used to create Figures 3.1 and 3.2. We illustrated three archetypal energy landscapes in §2.3: the weeping willow, palm, and banyan trees corresponding to gentle and steep funnels, and a hierarchical landscape, respectively. We expect that the disconnectivity graph of a system that readily locates the crystal on cooling—such as the homogeneous Lennard-Jones system[169]—will have the palm tree structure, while a good glass former will probably have a 'weeping willow' structure. In the immediate vicinity of the crystal, the banyan tree form is rather unlikely, as it would require the potential energy of low-lying disordered states to be similar to that of the ordered structure.

Figure 3.1 exhibits the expected palm-tree structure of a good crystal-former. The uphill barriers, out of the funnel, are much larger than their downhill counterparts, and there appear not to be any side-funnels that might act as kinetic traps. The central funnel of Figure 3.2 is also palm-tree like, but as the PES is ascended, increasing numbers of minima appear, and the graph takes a weeping willow form, characteristic of a more gentle funnel.

3.2 THE BINARY LENNARD-JONES SYSTEM

It has been suggested anecdotally that the lowest energy structure for the 80:20 binary Lennard-Jones mixture consists of separate phases of pure A and B atoms. This suggestion is somewhat surprising, as the most energetically favourable term is the A-B interaction, with $\epsilon_{\mathrm{AB}} = 1.5\,\epsilon_{\mathrm{AA}}$ compared to $\epsilon_{\mathrm{BB}} = 0.8\,\epsilon_{\mathrm{AA}}$.

As the most stable structure for the homogeneous Lennard-Jones solid is close-packed, it follows that two hypothetical phase-separated structures must also be close-packed. Obviously, in the bulk, surface effects between the two pure phases can be neglected so we calculated the energy of the phase-separated system by considering two independent subsystems of pure face-centred-cubic A and B atoms. We used the Stoddard-Ford shifting technique, and a cutoff of $2.5\,\sigma_{\alpha\beta}$. The volumes of the two simulation supercells were then varied, subject to the constraint that the mean number density of the entire system was kept constant at $1.2\,\sigma_{\mathrm{AA}}^{-3}$.

The mean energy per atom of the optimised phase-separated system was found to be $-6.025\,\epsilon_{\mathrm{AA}}$. This result is considerably higher than even the liquid-like minima obtained by Sastry et al.[98] for this system. The optimum density of the A phase is $1.12\,\sigma_{\mathrm{AA}}^{-3}$, giving a pair separation of $1.08\,\sigma_{\mathrm{AA}}$, while the corresponding parameters for the B phase are $1.67\,\sigma_{\mathrm{AA}}^{-3}$ and $1.07\,\epsilon_{\mathrm{AA}} = 1.22\,\epsilon_{\mathrm{BB}}$. Obviously the phase separated state lies very high in energy for this system, and so we used basin-hopping to attempt to find the true global minimum.

3.2.1 FINDING LOW-LYING MINIMA USING BASIN-HOPPING

Since the phase-separated minimum is obviously not the global minimum for BLJ we first decided to run a 'basin-hopping' global optimisation search.[170] The transformed landscape was explored starting from phase separated atoms on fcc lattice sites using Monte Carlo sampling of the transformed landscape at a temperature of $0.8\,\epsilon_{\mathrm{AA}}$. The random displacement of atomic coordinates for proposed steps was adjusted to give an acceptance ratio of about 1/2. Figure 3.3 shows the lowest minimum located in a run of 20000 basin-hopping steps. Another global optimisation run of the same length was performed, this time starting from the lowest energy minimum obtained by systematic quenching from a molecular dynamics (MD) trajectory at an energy of $-5.8594\,\epsilon_{\mathrm{AA}}$ per atom, but it did not produce a lower minimum. For a system of this complexity locating the global minimum reliably would require much longer basin-hopping runs than we have used here—we can only be confident that relatively low energy minima have been found. It is therefore not surprising that the two global optimisation runs did not converge to the same structure. Rather, this result suggests that the very lowest minima will probably exhibit some phase separation, and will be rarely sampled in an MD simulation of the liquid.

Our results may be compared with the energy obtained by Angell et al.'s extrapolation[128] of Sastry and coworkers' excitation profile.[98] Using the assumption that the critical temperature of mode-coupling theory, T_c, and the Kauzmann temperature, T_K are related by $T_c/T_K \sim 1.6$, Angell et al. obtained an energy of about $-7.08\,\epsilon_{\mathrm{AA}}$ per atom, which agrees reasonably well with the value of $-7.0541\,\epsilon_{\mathrm{AA}}$ per atom for our lowest energy minimum. The latter structure (Figure 3.3) appears to be a close-packed arrangement of A atoms, with B atoms arranged interstitially and substitutionally. There is a degree of phase separation, with the B atoms more concentrated near the top and bottom of the supercell. Hence the most stable structure for this system seems to be lamellar, as discussed in the next section, although obviously the thickness of the

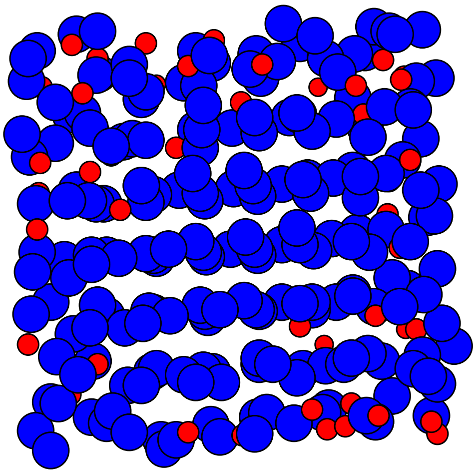

Figure 3.3: Lowest energy minimum found for the binary Lennard-Jones (BLJ) system, showing significant ordering of the larger A atoms and some degree of phase separation.

lamellae will be strongly affected by the size of the supercell and the number density of atoms.

The energy of this minimum depends significantly on the length of the cutoff employed, and whether the energy is shifted by the Stoddard-Ford (SF) quadratic function or by a constant, as discussed in §2.4.1. We present in Table 3.1 the energies of all the low-lying minima discussed in this chapter, calculated for cutoffs of $2.5\,\sigma_{\alpha\beta}$ and $1.842\,\sigma_{\alpha\beta}$ for the SF scheme, and $2.5\,\sigma_{\alpha\beta}$ for the Kob-Andersen (KA) constant shifting method. The data is presented using this variety of cutoffs to allow direct comparison with other results.

3.3 CRYSTALLINE MINIMA FOR BINARY LENNARD-JONES

3.3.1 60-ATOM SYSTEM

An apparently crystalline low-lying minimum for this system was found by Hernandez-Rojas and Wales,[182, 217] using a stochastic global optimisation method, which combined the basin-hopping approach,[170, 171] with kinetic Monte Carlo steps between local minima. They found that the potential energy of this ordered minimum is $-4.71\,\epsilon_{\mathrm{AA}}$

Table 3.1: Energies and symmetries of the crystalline minima for the different binary Lennard-Jones systems studied here. For comparison, we have included the energy of the lowest crystalline minimum found in previous work,[158] and we give the energies for cutoffs of both $1.842\,\sigma_{\alpha\beta}$ and $2.5\,\sigma_{\alpha\beta}$. For the latter cutoff, we have calculated the energies for the Kob-Anderson (KA) shifting method,[94] as well as for the Stoddard-Ford (SF) method.[190] The energies are in units of ϵ_{AA} per atom.

	$r_c = 2.5\,\sigma_{\alpha\beta}$ (SF)	$r_c = 2.5\,\sigma_{\alpha\beta}$ (KA)	$r_c = 1.842\,\sigma_{\alpha\beta}$ (SF)
60-atom supercell	-7.08	-7.68	-4.71
256-atom supercell	-7.20	-7.87	-4.74
320-atom supercell	-7.33	-7.99	-4.90
256-atom (amorphous)	-7.05	-7.72	-4.59

per atom. The energy of the lowest amorphous minimum for the 256-atom system described above (§3.2.1), with the energy recalculated for a cutoff of $1.842\,\sigma_{\alpha\beta}$ is considerably higher, at $-4.59\,\epsilon_{\mathrm{AA}}$. At first glance the 60-atom crystal structure appears to consist of cubic-close-packed regions of A atoms, which meet coherently at the (010) and (020) planes. The B atoms rest in trigonal prismatic holes, produced by the coherent boundaries. The 60-atom supercell appears to consist of three 20 atom unit cells, with unit cell dimensions, of $\mathrm{a} = \mathrm{b} = 3.684\,\sigma_{\mathrm{AA}}, \mathrm{c} = 1.228\,\sigma_{\mathrm{AA}}$ packed parallel to the z axis.

However, the interatomic distances vary between the three unit cells by 1-4%, and there appears to be some buckling of the structure. The three unit cells become identical when the structure and box lengths are optimised at a constant pressure of $0.6087\,\epsilon_{\mathrm{AA}}\sigma_{\mathrm{AA}}^{-3}$, which gives a number density of $1.2\,\sigma_{\mathrm{AA}}^{-3}$, but different box lengths. The dimensions of the 20-atom unit cell of the lowest energy structure are $a = 3.7708\,\sigma_{\mathrm{AA}}$, $b = 3.9255\,\sigma_{\mathrm{AA}}$ and $c = 1.1246\,\sigma_{\mathrm{AA}}$, and with a cutoff of $1.842\,\sigma_{\alpha\beta}$ the 60-atom supercell has an energy of $-4.85\,\epsilon_{\mathrm{AA}}$ per atom. Hence we conclude that the broken symmetry of the three unit cells is a consequence of forcing the structure into a cubic supercell.

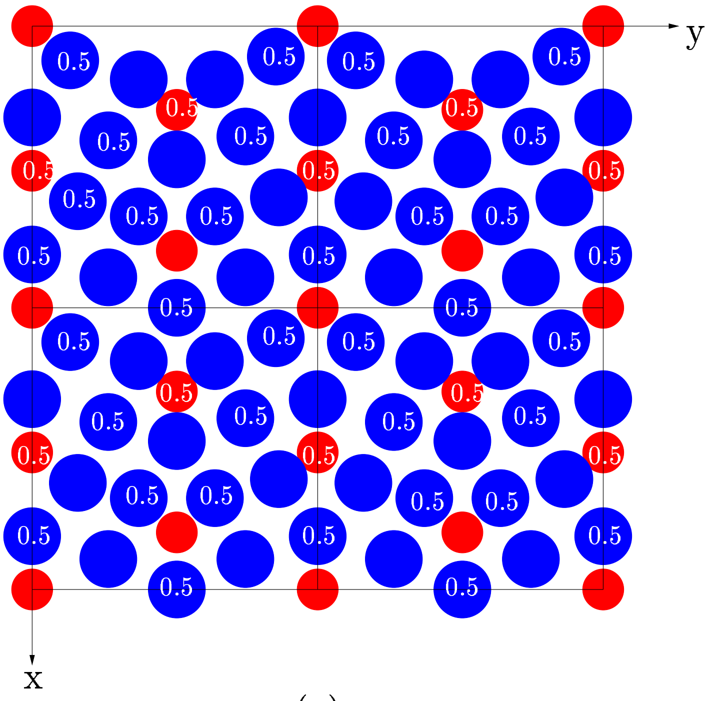

(a)

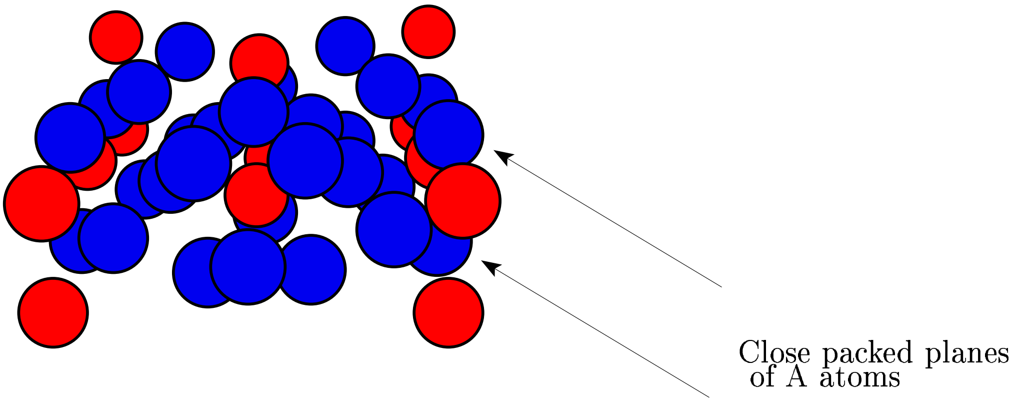

(b)

Figure 3.4: (a) Projection of four unit cells for the 60-atom supercell on the (001) plane. Each unit cell contains 20 atoms, with $a = 3.771\,\sigma_{AA}$, $b = 3.926\,\sigma_{AA}$ and $c = 1.125\sigma_{\mathrm{AA}}$. (b) Perspective view of one unit cell, looking down the (100) direction.

3.3.2 256-ATOM SYSTEM

We carried out a 'basin-hopping' global optimisation search[170] for a 256-atom system. It is impossible to create an exact 80:20 mixture with this number of atoms, but nevertheless this system size has been popular in previous simulation studies.[69,98] We created a starting configuration that was essentially face-centred-cubic A, with a unit cell dimension one quarter of the supercell box length, and one A atom replaced by a B atom in 51 of the fcc unit cells. Obviously it was impossible to spread the B atoms completely uniformly, because there were 51 B atoms and 64 fcc unit cells in our simulation box. The geometry was explored, starting from this configuration, using Monte Carlo sampling of the transformed potential energy surface (PES) at a temperature of $0.8\,\epsilon_{\mathrm{AA}}k_B^{-1}$. The random displacement of atomic coordinates for proposed steps was adjusted to give an acceptance ratio of about 0.5. Figure 3.5 shows the lowest minimum located in a run of 20 000 basin-hopping steps.

The lowest minimum has energy $-7.20\,\epsilon_{\mathrm{AA}}$ per atom, significantly lower than the energy of the lowest-lying amorphous minimum of this system, $-7.05\,\epsilon_{\mathrm{AA}}$ (§3.2.1). It is highly crystalline, again based upon fcc A atoms, but here one layer of the lattice has been replaced by B atoms. The remaining B atoms are spread throughout the supercell, where the B atoms replace A atoms in the fcc lattice. The B atoms in the layer are each surrounded by an approximate square prism of A atoms, with separations between $0.90\,\sigma_{\mathrm{AA}}$ and $0.92\,\sigma_{\mathrm{AA}}$. This range compares favourably with the equilibrium pair separation for the AB interaction of $0.898\,\sigma_{\mathrm{AA}}$.

3.3.3 320-ATOM SYSTEM

It is not possible to obtain an ordered minimum with a unit cell any smaller than the supercell for the 256-atom system, simply because there are 51 B atoms and 205 A atoms. We therefore created a 320-atom system, which consisted of 10 face-centred-square (fcs) layers of atoms stacked parallel to the z axis to create an fcc lattice. The first and sixth fcc layers were B atoms. Using this as a starting configuration, we carried out another basin-hopping global optimisation run, using the same parameters as in §3.3.2. The lowest energy structure found was qualitatively the same as the starting configuration. We then reoptimised this structure allowing the box lengths to vary, keeping the x and y box lengths equal, and the number density constant at 1.2. We converged the box lengths to a precision of $10^{-8}\,\sigma_{\mathrm{AA}}$.

The box length and subsequent geometry optimisation produced the structure illustrated in Figure 3.6. It has energy of $-7.33\,\epsilon_{\mathrm{AA}}$ per atom, significantly lower than that of the 256-atom system. For comparison with the 60-atom system, we shortened

Table 3.2: Coordination shells in the 320-atom supercell. Distances are given in units of σ_{AA}. $\sigma_{\mathrm{AB}} = 0.8$ and $\sigma_{\mathrm{BB}} = 0.88$, so the equilibrium pair distances for AA, AB and BB interactions are $1.1225\,\sigma_{\mathrm{AA}}$, $0.8980\,\sigma_{\mathrm{AA}}$ and $0.9878\,\sigma_{\mathrm{AA}}$, respectively. The bracketed numbers are the ratios of the interatomic distances in the crystal and the corresponding equilibrium pair separation, $2^{1/6}\,\sigma_{\alpha\beta}$ where α, β are A or B.

		A_1	A_2	B
Nearest Neighbour	Atom type	B	A_2	A_1
	Coordination number	4	4	8
	Coordination geometry	Square pyramid	Square planar	Square prism
	Distance	0.9321 (1.038)	1.0907 (0.9716)	0.9321 (1.038)
2^{nd} Nearest Neighbour	Atom type	A_1	A_1	B
	Coordination number	1	4	4
	Coordination geometry		Square pyramid	Square Planar
	Distance	1.0471 (0.933)	1.1232 (1.001)	1.0907 (1.104)
3^{rd} Nearest Neighbour	Atom type	A_1	A_2	A_2
	Coordination number	4	4	2
	Coordination geometry	Square planar	Square pyramid	Linear
	Distance	1.0907 (0.9716)	1.1274 (1.004)	1.3402 (1.492)
4^{th} Nearest Neighbour	Atom type	A_2	B	B
	Coordination number	4	1	4
	Coordination geometry	Square pyramid		Square Planar
	Distance	1.1232 (1.001)	1.3402 (1.194)	1.5424 (1.7527)
5^{th} Nearest Neighbour	Atom type	A_1	A_2	A_2
	Coordination number	4	4	4
	Coordination geometry	Square pyramid	Square planar	Square Prism
	Distance	1.5120 (1.347)	1.5424 (1.3741)	1.7279 (1.9242)

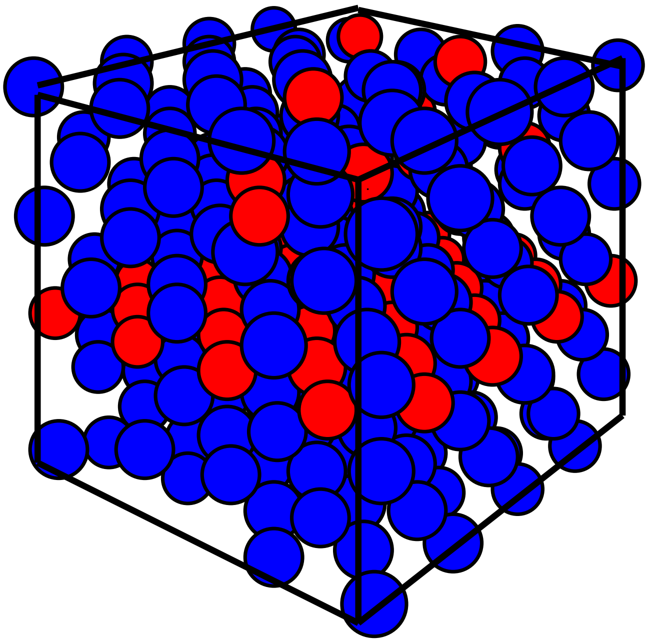

Figure 3.5: Perspective view of the 256-atom crystalline system. The single layer of B atoms in the fcc lattice and the single B atoms coordinated by eight A atoms are clearly visible.

the cutoff to $1.842\,\sigma_{\alpha\beta}$, and reoptimised the geometry. The energy was $-4.90\,\epsilon_{\mathrm{AA}}$, significantly lower than the $-4.71\,\epsilon_{\mathrm{AA}}$ of the 60-atom system. The unit cell is illustrated in Figure 3.6. It contains eight A atoms, and two B atoms, and has $a = b = 1.091\,\sigma_{\mathrm{AA}}$, and $c = 7.003\,\sigma_{\mathrm{AA}}$. The space group is *I4/mmm*. The positions of the atoms, given in terms of the unit cell dimensions are: A atoms at Wyckoff 4e positions, with coordinates $(0, 0, 0.327)$ and $(0, 0, 0.191)$, and B atoms at Wyckoff 2a positions, with coordinates $(0, 0, 0)$.[218] We label the A atoms of the former type A_1 and the latter A_2. The first to fifth nearest neighbours are described in detail in Table 3.2, and it is worth noting that in this structure the A atoms form a square prism around the B atoms, with distances

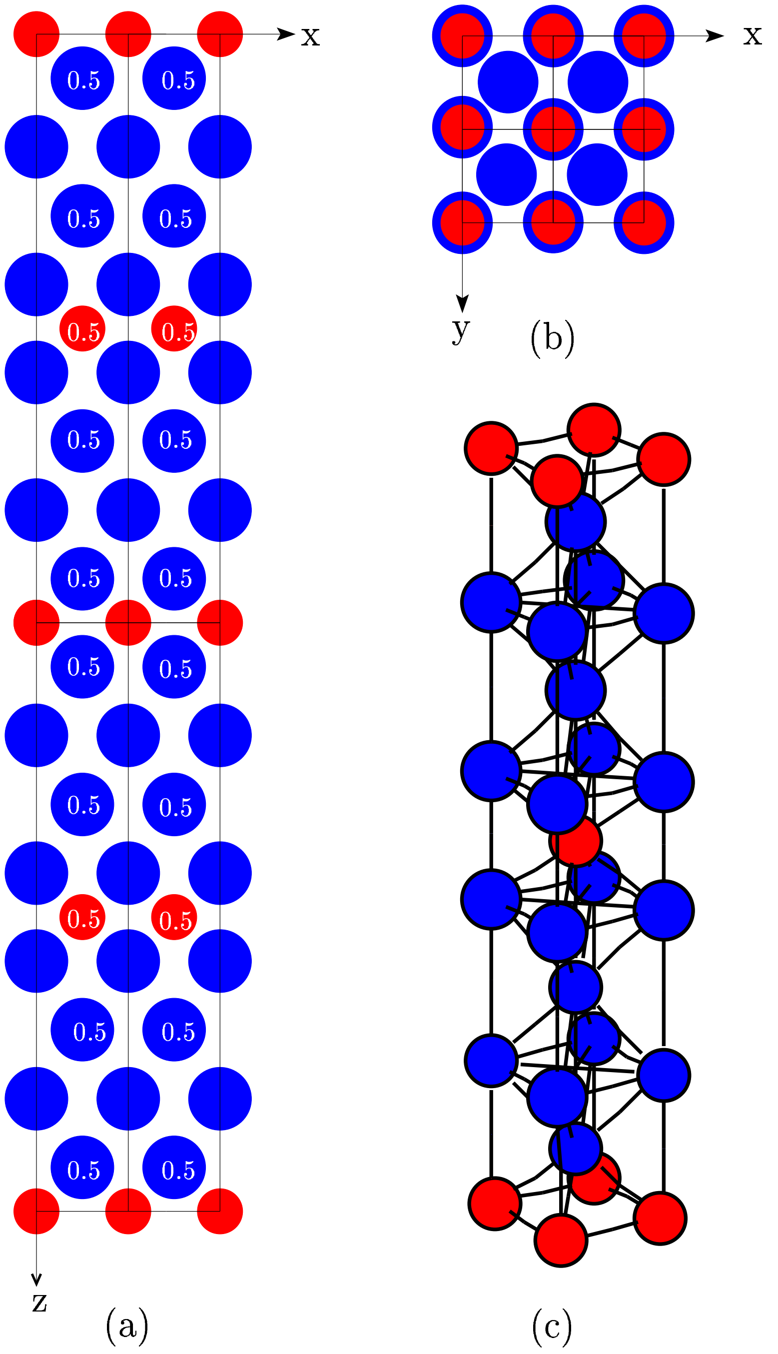

Figure 3.6: Illustrations of the lowest energy crystal structure for the 320-atom supercell: (a) projection of four unit cells on the (010) plane; (b) projection of four unit cells on the (001) plane; (c) perspective view of one unit cell. This structure has space group $I\ 4/mmm$, with $a = b = 1.091\sigma_{\mathrm{AA}}$ and $c = 7.003\sigma_{\mathrm{AA}}$.

$0.9921\,\sigma_{\mathrm{AA}}$, which is 4% larger than the equilibrium pair separation for this interaction. This basic crystal structure has previously been seen for $\mathrm{Ir(UC)_2}$ where the Ir atoms are in the B positions, and the U and C atoms are approximately in the A_1 and the latter A_2 positions, respectively.[219,220] Atomic coordinates for this minimum are available from the Cambridge Cluster Database.[221]

Calvo has attempted to calculate the melting point of this crystal using the moving interface method, with canonical MD.[222] Preliminary results suggest that $k_{\mathrm{B}}T_m \sim 0.65\,\epsilon_{\mathrm{AA}}$, which is consistent with the empirical relation that $T_g \sim 2T_m/3$, if we consider that Kob and Andersen's value of T_c, $0.435\,\epsilon_{\mathrm{AA}}/k_{\mathrm{B}}$, is the glass transition temperature on the MD simulation timescale. At a temperature of $0.65\,\epsilon_{\mathrm{AA}}/k_{\mathrm{B}}$, the region of the landscape that the system explores is considerably lower in energy than the high temperature plateau on Sastry's excitation profile.[98] The temperature dependence of the diffusion constant is super-Arrhenius, and so rearrangements in the melt that lead to crystallisation take place on timescales much longer than that of MD.

We used this low energy minimum as the starting point for a series of searches for transition states and connected local minima to investigate the surrounding PES at constant volume, using the box lengths of the lowest energy crystal. Obviously the constant volume constraint is somewhat artificial, but all the stationary points in our database are sufficiently similar that it is unlikely to affect our results significantly. As before, we sampled minima according to SS1, described in §2.1.4.

Figure 3.7 was obtained using Mortenson's simplification method based on canonical rate constants, outlined in §2.3. The temperature used for the calculation of the canonical rate constants was $0.6\,\epsilon_{\mathrm{AA}}k_B^{-1}$, and the rate threshold used to group the minima was $10^{-8}\ \left(\epsilon_{\mathrm{AA}}/m\sigma_{\mathrm{AA}}^2\right)^{1/2}$, assuming unit mass for both A and B atoms. The graph shows the lowest 250 minima left in the database after the grouping was carried out. Visual comparison of the 'full' disconnectivity graph of 5011 nodes (not shown here) confirmed that its essential features were retained when the graph was coarse-grained using this technique.

Within the energy range considered all the minima exhibit a high degree of crystallinity. The minima with energies around $-7.30\,\epsilon_{\mathrm{AA}}$ generally contain one permutation of an A and a B atom, and those with around $-7.28\,\epsilon_{\mathrm{AA}}$, contain two such defects. Figure 3.7 shows that high barriers exist between some of these defective crystalline minima, resulting in a 'willow tree' pattern described in §2.3, illustrating that this region of the PES acts as a gentle funnel towards the lowest crystalline minimum.

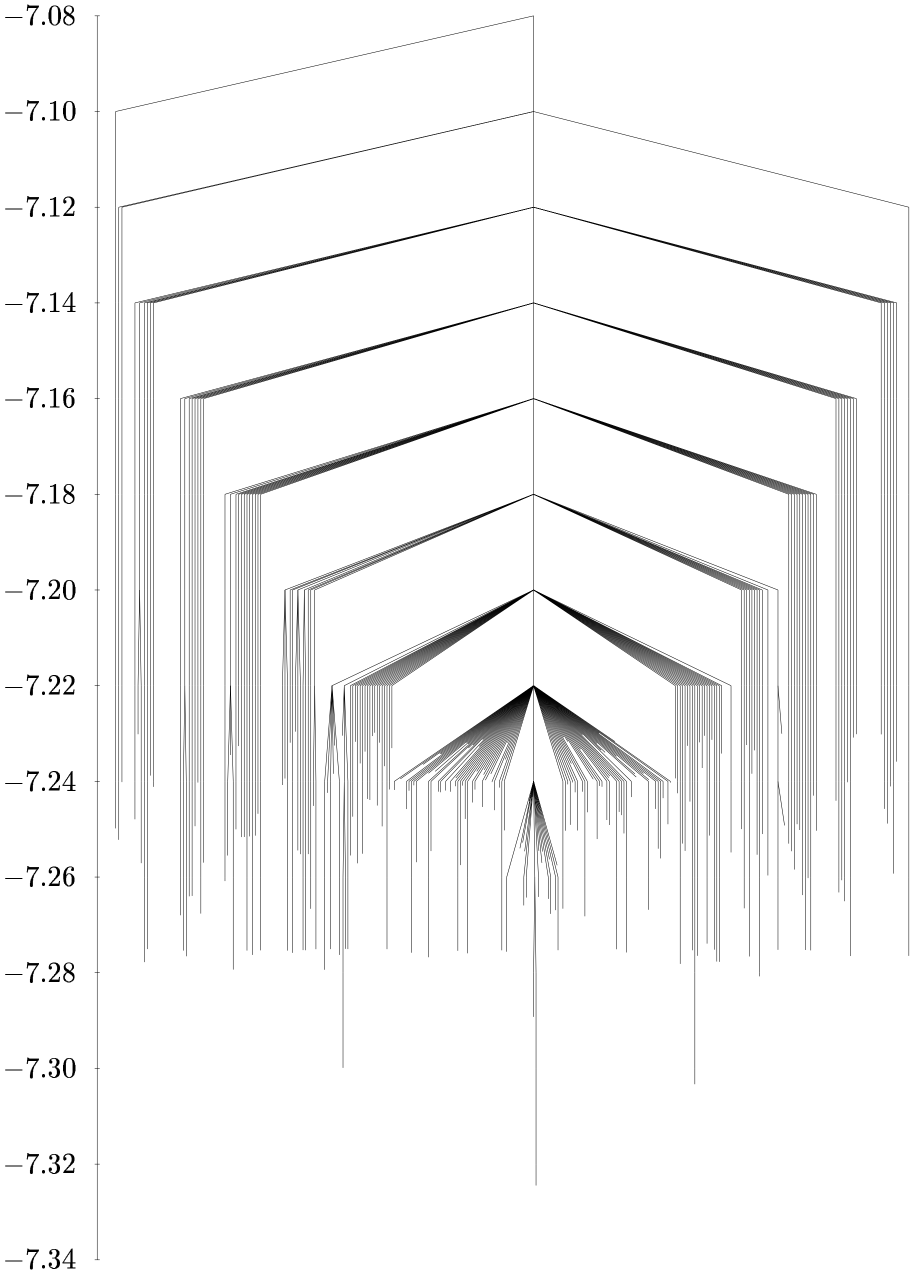

Figure 3.7: Disconnectivity graph produced using the grouping algorithm for the 320-atom supercell with optimised box lengths. The threshold rate was $10^{-8}\sqrt{\epsilon_{\mathrm{AA}}m}/\sigma_{\mathrm{AA}}$, the temperature used to calculate the canonical rate constants was $0.6\,\epsilon_{\mathrm{AA}}/k_{\mathrm{B}}$, and only the lowest 250 minima are shown here. The salient features of the 'full' tree, which contains 5011 minima, are retained in this simplified diagram. The energy scale is in ϵ_{AA} per atom.

It is obvious, even from the simplified disconnectivity graph, that the energy density of minima increases rapidly as the PES is ascended—even in the predominantly crystalline portion depicted in Figure 3.7—owing to the large number of possible relative positions of permuted atoms. This willow tree pattern is qualitatively different from the strong funnel of the unit density Lennard-Jones system, illustrated in Figure 3.1. The presence of a large number of low-lying minima provides a first indication of how the resistance to crystallisation of the binary Lennard-Jones system arises at an atomic level.

3.4 SUMMARY

We have characterised the regions of configuration space for our glass formers in the immediate vicinity of their crystalline global minima. In the case of the binary Lennard-Jones system, we have found new crystals, for 256- and 320-atom systems, and characterised in detail the crystalline minimum of the 60-atom system.

Following our publication of the BLJ results presented in this Chapter,[182] Fernández and Harrowell improved the structure.[223] They correctly interpreted our 320-atom structure as alternating layers of the CsCl structure and pure A atoms. They allowed the density to vary and found that the the optimal layered structures at a number of different A:B ratios were those that minimised the number of interfaces between the fcc A and the CsCl AB structure. Thus the crystal structure with the 10-atom unit cell was improved further by creating a single layer of the AB CsCl phase, and the energy could be improved further by increasing the unit cell size and allowing thicker alternating layers to form. Their findings give us further insight into the excellent glass forming properties of this system: layer formation from the melt is likely to be kinetically slow with significant entropic barriers, and therefore will not be observed on the timescale of feasible MD simulations.

The qualitative differences between the disconnectivity graphs of the homogeneous Lennard-Jones, SW silicon and binary Lennard-Jones systems illustrate the ease or difficulty with which these systems crystallise. In particular, the rapid increase in the number of minima of the BLJ system as the landscape is ascended, even in the immediate vicinity of the crystal, indicate that there is a very large entropic component to the free energy barrier to crystallisation, compared to its homogeneous counterpart.

We will further examine the effects of decreasing order in the following chapter, and the low-lying BLJ minima obtained here by basin-hopping will serve as starting points for some more detailed study of the potential energy landscape.

4

Exploring the Potential Energy Surface

Our next step was to generate databases of minima and transition states for the binary and homogeneous Lennard-Jones systems and the Stillinger-Weber (SW) silicon potential. The rearrangement pathways thus generated can help to explain the mechanisms of relaxation and transport processes, both in the glass and the supercooled liquid.

In order to be confident that our results were truly representative of the dynamics of the systems studied, we produced databases both at constant volume, and allowing the box lengths to vary using the methods described in §2.1.3. We also sampled the binary Lennard-Jones system using two different sampling schemes (SS2 and SS3), and used starting configurations generated from basin-hopping and MD.

This chapter has two principal sections, detailing results at constant volume and constant pressure, respectively.

4.1 Labelling system for databases of stationary points

As we outlined in Chapter 2, we used three different sampling schemes to generate our databases of minima and connecting transition states. We also used four different potentials, and generated databases under both constant volume and constant pressure conditions.

In order to clarify the presentation of our results, we use the labelling system explained below and detailed in Table 4.1. The system operates as follows:

1. The interatomic potential is represented by a two or three letter code: Stillinger-

Table 4.1: Details of the labelling system for the databases of minima and transition states that we obtained. The modified SW silicon potential has the three-body term increased by 50% (§2.4.2). The number densities and pressures at which the databases were generated are included for the results at constant volume and pressure, respectively. The units for number density (ρ) are σ^{-3}, and those for pressure (P) are $\epsilon\sigma^{-3}$. The 'Approximate Crystallinity' column refers to the most crystalline minimum in the database: and is an approximate figure obtained by inspection (§4.2.1). The starting configuration is the first minimum used to generate the database, and is obtained from basin-hopping global optimisation (§2.2), manual construction or from another database.

Database	Potential	ρ	P	Approximate Crystallinity	Source of starting configuration	Sampling scheme
BLJ1-3	binary Lennard-Jones	1.20		0%	Basin-hopping	SS2
BLJ4-10				0%	BLJ1-3	SS3
BLJ11-14				0%	MD	SS3
LJ(x)	homogeneous Lennard-Jones	1.0		100%	Construction	SS1
ULJ1				80%	MD	SS3
ULJ2				50%	MD	SS3
ULJ3				0%	MD	SS3
RLJ1-2		0.93		0%	MD	SS3
SW(x)	Stillinger-Weber silicon	0.46		0%	MD	SS1
SW1-3				0%	MD	SS3
SW1.5	Modified SW			0%	MD	SS3
BLJLP(x)	binary Lennard-Jones		0.6	100%	Basin-hopping	SS1
BLJLP1				0%	BLJ11	SS1
BLJLP2				0%	BLJ12	SS1
BLJLP3				0%	BLJ13	SS1
BLJHP			1.2	0%	BLJ11	SS1
SWP1	Modified SW		4×10^{-5}	100%	SW2	SS1
SWP2				0%	MD	SS1

Weber silicon (SW), binary Lennard-Jones (BLJ), unit density Lennard-Jones (ULJ) or homogeneous Lennard-Jones relaxed to the optimum density for the face-centred-cubic (fcc) crystal (RLJ).

2. If the database was generated at constant pressure, an additional alphabetical code is added: 'HP' for the high pressure BLJ database, 'LP' for the low pressure BLJ databases and 'P' for all other constant volume databases.

3. A number then follows for amorphous databases, or '(x)' for crystalline databases.

4.2 SELECTION OF STARTING CONFIGURATIONS FOR DATABASE GENERATION

Database BLJ1 was obtained using SS2 (up to eight searches per minimum) by starting from the lowest energy amorphous BLJ minimum described in §3.2.1. Databases BLJ2 and BLJ3 were generated using SS2 starting from two of the minima obtained by quenching every $\sqrt{m\sigma_{\mathrm{AA}}{}^2/\epsilon_{\mathrm{AA}}}$ time units from an MD trajectory of length 1000 $\sqrt{m\sigma_{\mathrm{AA}}{}^2/\epsilon_{\mathrm{AA}}}$ at total energy $-3.906\,\epsilon_{\mathrm{AA}}$ per atom. The energies of the starting minima for the two samples were selected to produce databases of minima that fully span the range of inherent structure energies studied by Sastry et al.[98] Apart from the energy range, the selection of these starting minima was random.

To check the dependence upon the sampling scheme and the starting minimum we generated databases BLJ4-10 using SS3 (400 searches per minimum). The starting minima were selected randomly from databases BLJ1-3: except that their energies were chosen to span the full range of the latter databases, and that the BLJ4 starting configuration was the very low energy minimum used as the starting point for BLJ1.

As one final check of the statistics we generated databases BLJ11-14 using SS3 and starting minima obtained from a further set of short MD trajectories suggested by the cooling schedules of Sastry et al.[98] The system was initially equilibrated for 5000 steps at a total energy of $-1.875\,\epsilon_{\mathrm{AA}}$ per atom, with a time step of 0.003 $\sqrt{m\sigma_{\mathrm{AA}}{}^2/\epsilon_{\mathrm{AA}}}$. It was then cooled by successive runs of 100 steps at progressively lower total energies. The energy was reduced each time by $0.07188\,\epsilon_{\mathrm{AA}}$ per atom by rescaling the velocities, corresponding to a cooling rate of $4.219 \times 10^{-3}\,\epsilon_{\mathrm{AA}}{}^{3/2} m^{-1/2} \sigma_{\mathrm{AA}}{}^{-1}$ per atom. This cooling rate corresponds to the fastest schedule used by Sastry et al. Cooling was continued until the total energy was essentially equal to the potential energy of the (unquenched) configuration. Databases BLJ11-14 correspond to configu-

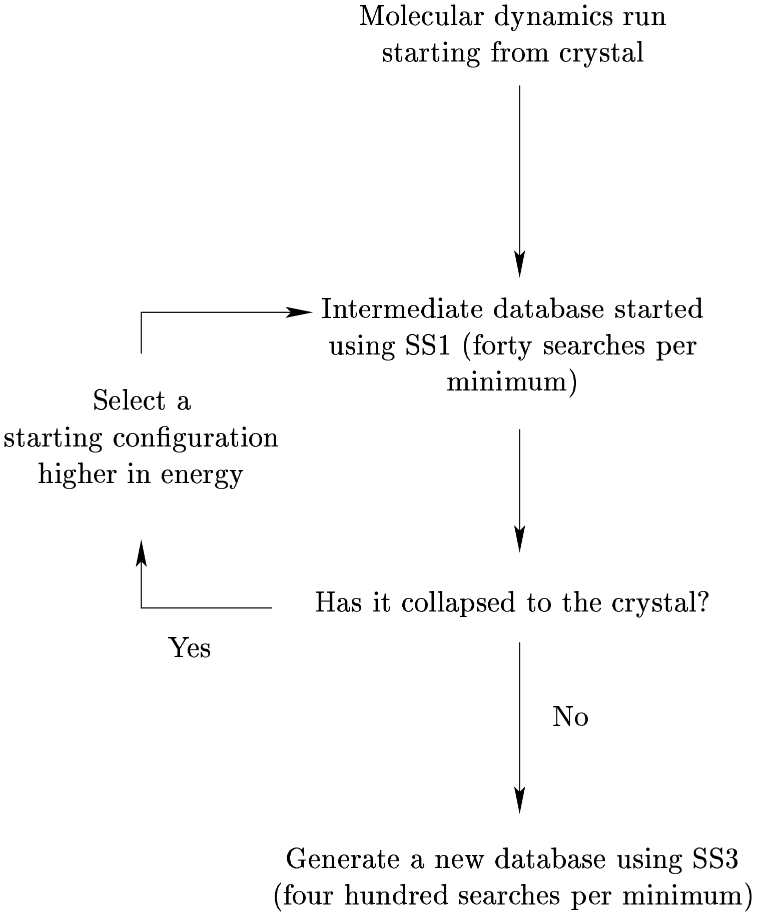

Figure 4.1: Method used to select starting configurations for the databases of stationary points for the homogeneous Lennard-Jones and SW Silicon systems.

rations obtained by starting from minima with total kinetic and potential energies of $-6.8344\,\epsilon_{\rm AA}$, $-5.3969\,\epsilon_{\rm AA}$, $-4.6781\,\epsilon_{\rm AA}$ and $-2.1625\,\epsilon_{\rm AA}$ per atom, respectively.

To generate starting minima for the Stillinger-Weber and the unit density (ULJ) and relaxed (RLJ) Lennard-Jones systems, we used the method illustrated in Figure 4.1. First, we conducted standard MD runs of increasing total energy starting from the appropriate crystal. Quenches were performed at regular intervals to determine when the (superheated) system first escaped from the crystal. The quench minima following escape were each used as the starting points for exploration of the PES using the SS1 sampling scheme (§2.1.4). We found that initial minima containing even small regions of crystallinity collapsed to the crystal after a few hundred minima (or less) had been sampled. However, eventually a starting minimum was always located where the crystal

Table 4.2: Details of the databases studied. E_1 is the energy of the initial minimum, E_{low} and E_{high} are the energies of the lowest and highest lying minima, N_{min} is the number of minima in the database, and N_{ts} is the number of transition states. All the energies are in ϵ per atom (§2.4). $\langle E_{\text{min}} \rangle$ and $\langle E_{\text{ts}} \rangle$ are the mean energies of the minima and transition states, respectively.

Database	E_1	E_{low}	E_{high}	N_{min}	$\langle E_{\text{min}} \rangle$	$\langle E_{\text{ts}} \rangle$
binary Lennard-Jones, sampling scheme SS2						
BLJ1	−7.0541	−7.0541	−6.8546	9275	−6.9784	−6.9695
BLJ2	−6.9377	−6.9811	−6.8280	9485	−6.9197	−6.9115
BLJ3	−6.8560	−6.9846	−6.8185	9571	−6.9176	−6.9097
binary Lennard-Jones, sampling scheme SS3						
BLJ4	−7.0541	−7.0541	−6.9285	7867	−7.0070	−6.9930
BLJ5	−7.0336	−7.0444	−6.9206	8126	−6.9949	−6.9802
BLJ6	−7.0137	−7.0514	−6.8958	8161	−6.9889	−6.9766
BLJ7	−6.9948	−7.0242	−6.8906	8455	−6.9737	−6.9605
BLJ8	−7.0016	−7.0220	−6.8916	8434	−6.9694	−6.9564
BLJ9	−6.9531	−6.9716	−6.8519	8435	−6.9277	−6.9155
BLJ10	−6.9350	−6.9585	−6.8218	8810	−6.9131	−6.9013
binary Lennard-Jones, sampling scheme SS3						
BLJ11	−6.9723	−6.9846	−6.8699	8419	−6.9356	−6.9235
BLJ12	−6.9439	−6.9734	−6.8434	8708	−6.9245	−6.9124
BLJ13	−6.9218	−6.9598	−6.8252	8674	−6.9029	−6.8900
BLJ14	−6.8936	−6.9427	−6.8177	9109	−6.8866	−6.8745
unit density Lennard-Jones, sampling scheme SS3						
ULJ1	−7.3444	−7.3456	−7.2186	4460	−7.3141	−7.3038
ULJ2	−7.2513	−7.3456	−7.1579	7541	−7.2595	−7.2349
ULJ3	−7.0147	−7.3957	−6.9774	9212	−7.0580	−7.0319
relaxed Lennard-Jones, sampling scheme SS3						
RLJ1	−6.9711	−7.4908	−6.8775	8355	−7.0614	−7.0005
RLJ2	−6.9072	−7.7067	−6.8751	8249	−7.0512	−7.0392
Stillinger-Weber Si, sampling scheme SS3						
SW1	−1.8949	−1.8966	−1.8838	6939	−1.8921	−1.8920
SW2	−1.8796	−1.8857	−1.8779	5834	−1.8807	−1.8803
SW3	−1.8631	−1.8750	−1.8623	5883	−1.8660	−1.8654
adjusted Stillinger-Weber Si potential, sampling scheme SS3						
SW1.5	−1.8496	−1.8892	−1.8251	8716	−1.8485	−1.8452
largely crystalline ULJ and SW samples, sampling scheme SS1						
SW(x)	−1.9937	−2.0000	−1.9601	7664	−1.9784	−1.9777
LJ(x)	−7.5392	−7.5392	−7.2473	3367	−7.3641	−7.3619

was not found in the SS1 procedure, even after sampling several thousand minima. The starting minima used in the generation of the final databases were chosen from these intermediate databases that did not collapse to the crystal. The intermediate databases were then discarded.

Databases SW1-3 were generated using SS3 (§2.1.4) starting from minima at the bottom, middle and top of the intermediate SS1 database, respectively, in terms of their energy. Database SW1.5 was generated using SS3 starting from the same minimum as for SW1, but reoptimised with the new potential, in which the three-body term is increased by 50% (S2.4.2). Increasing the three-body term has the effect of increasing the energetic favourability of tetrahedral coordination.[164] Databases ULJ1-3 were generated using SS3 starting from minima at the bottom, middle and top of the intermediate SS1 databases, as for SW1-3. Databases RLJ1 and RLJ2 were generated using SS3 starting from minima at the bottom and top of the intermediate SS1 database.

Although the intermediate SS1 database for ULJ did not collapse to the crystal, it nevertheless managed to reach minima containing significant crystalline character. The starting configurations for the ULJ1 and ULJ2 databases appear from inspection to be about 80% and 50% crystalline, respectively, although their values of the crystallinity order parameter, Q_6* are similar, but their barrier distributions are not very different from ULJ3. All the other starting minima and the corresponding databases, including ULJ3, have no atoms in crystalline environments. Table 4.2 contains some statistics for each of the databases.

4.2.1 CRYSTALLINITY

The Stillinger-Weber and homogeneous Lennard-Jones systems have crystalline global minima: the diamond and hcp structures respectively. Q_6 is a particularly useful order parameter to measure the degree of close-packing, as it has a value of exactly zero for the liquid, and has a similar value for all common crystalline structures, namely 0.57452 for fcc, 0.48476 for hcp, and 0.51069 for body-centred-cubic (bcc). Thus, values close to zero represent a highly disordered structure, while values in the range $0.4 - 0.5$ are

---

[*] Q_6 is an order parameter introduced by Steinhardt et al.,[224] which can be used as a measure of crystallinity. It is based on on the sum of sixth order spherical harmonics for all the N_b bonds in the supercell, using the minimum image convention. The value of Q_6 is a little sensitive to the choice of cut-off, which determines which atoms are bonded: the value we used was 1.24 times the nearest neighbour distance for the fcc structure, as used in previous work.[225]

indicative of crystalline order.

The average values of Q_6 for our ULJ samples are 0.45 for ULJ1, 0.46 for ULJ2 and 0.17 for ULJ3. All the values for the BLJ samples are less than 0.1, and those for RLJ1 and RLJ2 are 0.24 and 0.21, respectively. Q_6 is not applicable as a measure of crystallinity with tetrahedral coordination, and so it cannot be applied to the SW system.

4.3 Properties of the PES at constant volume

4.3.1 Barrier distributions

Every transition state is associated with an uphill (larger) and a downhill (smaller) barrier (§2.1), except for degenerate rearrangements[226] where these are the same. We present the barrier height distributions using a Gaussian for each data point:

$$f(b) = \frac{1}{n}\sum_{i=1}^{n}\frac{e^{-(b-b_i)^2/2s^2}}{\sqrt{2\pi s^2}}.$$

This convolution produces a smooth function when the Gaussian width, s, is chosen appropriately. An approximate representation of the probability distribution, $f(b)$, for the barrier height, b, is thereby obtained from the n observed barrier heights, b_i, in the database.

We will focus on the downhill (§2.1) barrier distributions for brevity. For any pathway the uphill barrier is equal to the downhill barrier plus the energy difference between the higher and the lower lying minima. The uphill barrier distribution is therefore largely determined by the distribution of energy differences between minima. We also expect relaxation towards equilibrium to be more dependent upon the downhill barrier distribution.

Uphill and downhill barrier distributions for the different databases are illustrated in Figures 4.2-4.7. Table 4.3 summarises the maxima in the uphill and downhill barrier distributions. For the most extensively investigated BLJ system it is apparent from Figures 4.2–4.4 that there is no dramatic variation in the downhill barrier distributions we have obtained for different searching methods or choices of starting configuration.

Figure 4.3 shows that a smaller number of searches from each minimum tends to bias the distribution towards lower energy barriers. Databases BLJ1-3 were generated using SS2 with eight searches from each minimum: databases BLJ4-10 span the same energy range. The maxima in the downhill barrier distributions, in Table 4.3, are similar

Table 4.3: Mean values of the integrated path lengths, $\langle S\rangle$, in σ (§2.4); separations of connected minima, $\langle D\rangle$, in σ; and cooperativity indices, $\left\langle \widetilde{N} \right\rangle$, for all the databases studied. These quantities are defined in §4.3.2. $E_{\max}$(up) and $E_{\max}$(down) are the energies of the largest maxima in the distributions of uphill and downhill barriers, respectively, in ϵ per supercell.

Database	$\langle S\rangle$	$\langle D\rangle$	$\left\langle \widetilde{N} \right\rangle$	$E_{\max}$(up)	$E_{\max}$(down)
		binary Lennard-Jones, sampling scheme SS2			
BLJ1	4.13	1.47	5.58	0.09923	0.05077
BLJ2	4.48	1.59	8.18	0.14628	0.05078
BLJ3	4.46	1.60	8.40	0.14655	0.04564
		binary Lennard-Jones, sampling scheme SS3			
BLJ4	5.99	1.88	4.71	5.31484	0.03397
BLJ5	5.79	1.84	4.51	5.17010	0.03877
BLJ6	6.14	1.91	6.68	0.55880	0.05481
BLJ7	6.50	1.96	6.80	0.68001	0.03279
BLJ8	5.77	1.82	5.17	4.66479	0.04504
BLJ9	6.72	2.01	7.86	0.28832	0.03022
BLJ10	6.96	2.13	9.88	0.73759	0.04985
		binary Lennard-Jones, sampling scheme SS3			
BLJ11	7.11	2.12	8.06	10.61102	0.05453
BLJ12	7.08	2.11	10.09	0.99954	0.05040
BLJ13	7.24	2.18	10.84	1.08445	0.04902
BLJ14	6.80	2.14	11.19	0.78742	0.04485
		unit density Lennard-Jones, sampling scheme SS3			
ULJ1	3.91	1.57	2.74	0.17093	0.06135
ULJ2	5.92	2.02	3.50	1.56803	0.04799
ULJ3	12.30	3.54	36.53	1.50377	0.05206
		relaxed Lennard-Jones, sampling scheme SS3			
RLJ1	13.25	3.57	22.96	6.94788	0.04900
RLJ2	9.11	3.05	45.85	2.50320	0.04395
		Stillinger-Weber Si, sampling scheme SS3			
SW1	2.43	0.95	8.18	0.02010	0.00412
SW2	2.26	0.90	16.68	0.00639	0.00317
SW3	2.54	0.94	17.25	0.00634	0.00243
		adjusted Stillinger-Weber Si potential, sampling scheme SS3			
SW1.5	3.74	1.35	5.17	0.01366	0.00795

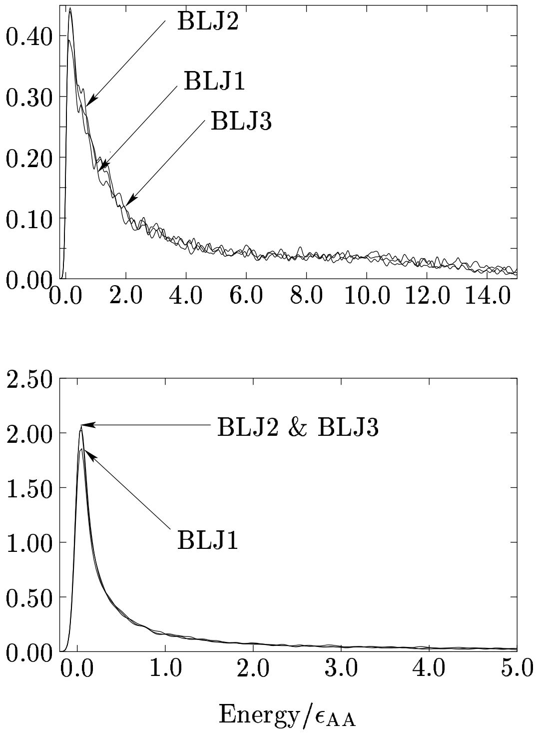

Figure 4.2: Uphill and downhill barrier distributions for binary Lennard-Jones (BLJ) databases BLJ1-3 generated using the first sampling scheme SS2 described in §2.1.4 (maximum of eight transition state searches per minimum). The Gaussian width $s = 0.05\,\epsilon_{AA}$ and the barriers are in ϵ_{AA} per supercell.

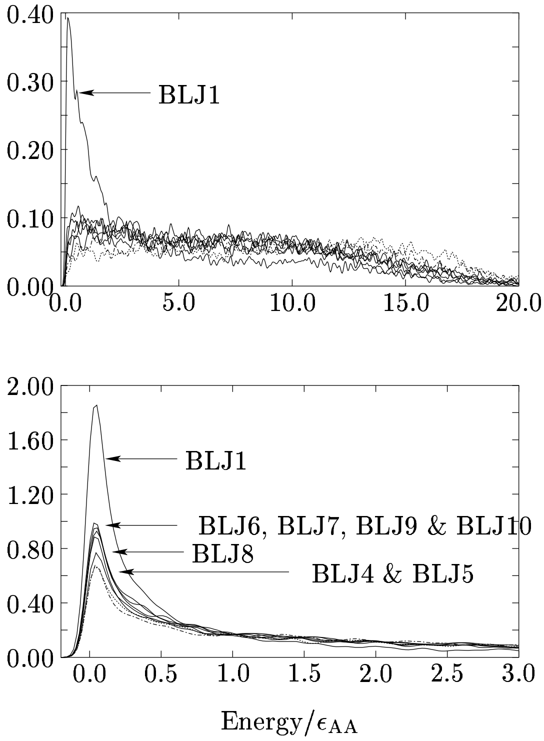

Figure 4.3: Uphill and downhill barrier distributions for binary Lennard-Jones (BLJ) databases BLJ5-10 generated using the second sampling scheme SS3 described in §2.1.4 (400 transition state searches per minimum). Database BLJ1 is included for comparison. The Gaussian width $s = 0.05\,\epsilon_{AA}$ and the barriers are in ϵ_{AA} per supercell.

for all the data sets, varying between about $0.03 - 0.05\,\epsilon$, with no apparent pattern. The uphill barrier distributions of samples BLJ1-10 appear to vary with little obvious pattern, except that those for the lowest energy data sets have maxima at energy $5\,\epsilon$, an order of magnitude higher than all the others, except for BLJ8. As before, we report barrier heights as energy differences per supercell, since the relevant barriers should not scale extensively with system size.

It is surprising that the barrier distributions appear to be similar for all the BLJ samples, as Sastry et al.,[98] inferred for the same system that the barriers increase in magnitude as the system explores lower energy regions of the PES. This observation may be partly produced by the change in the uphill barrier distribution: the system becomes trapped in low lying minima, and must surmount large uphill energy barriers to escape. However, it probably the case that the 'barriers' observed by Sastry et al. correspond to the total activation energy for multi-step processes, rather than to single rearrangements. Our results are supported by the work of Kopsias and Theodorou, who found that the free energy barrier heights for a 198 atom homogeneous Lennard-Jones system[145] were independent of the free energies of the minima involved.

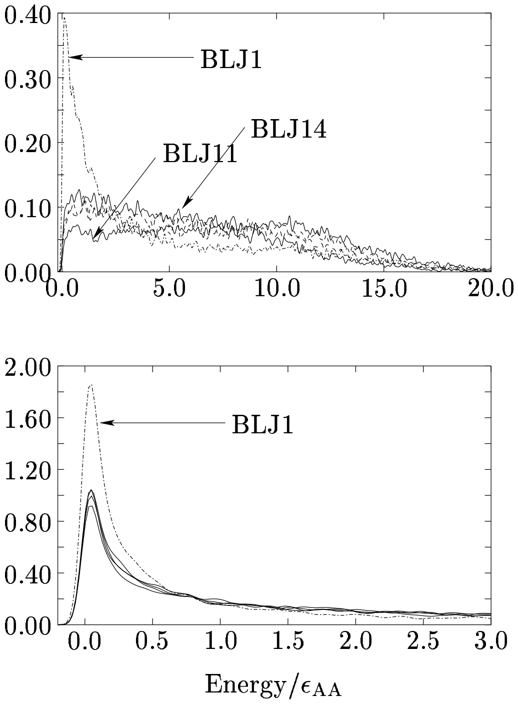

Figure 4.4: Uphill and downhill barrier distributions for the binary Lennard-Jones (BLJ) databases BLJ11-14 generated using sampling scheme SS3 (§2.1.4) (400 transition state searches per minimum) and starting minima derived from an MD cooling run. The Gaussian width $s = 0.05\,\epsilon_{AA}$ and the barriers are in ϵ_{AA} per supercell.

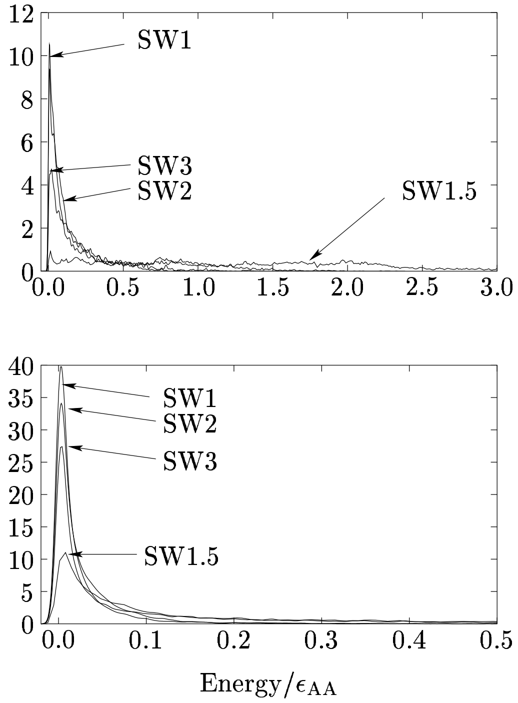

Figure 4.5: Uphill and downhill barrier distributions for the Stillinger-Weber databases SW1-3 and for the modified Stillinger-Weber potential SW1.5 (2.4.2). The Gaussian width $s = 0.005\,\epsilon$ and the barriers are in ϵ per supercell.

Both Figure 4.5 and Table 4.3 show that the energy of the largest maximum in the downhill barrier distribution for databases SW1-3 decreases slightly as the energy of the minima increases. However, this maximum occurs for rather low energies of order $0.004\,\epsilon$ per supercell, which corresponds to only around 0.01 eV. There is a slight increase in the energy of the downhill maxima with decreasing energy of the minima in the samples, but for the lowest energy sample, SW1, the peak in the uphill barrier distribution is at an energy an order of magnitude higher. All the maxima are at very low energies, a result that contrasts strongly with the maxima at around 2 eV found by Barkema and Mousseau,[140] although they also found a significant maximum at low energy. They assigned this low energy maximum to the presence of 'unstable' minima in the sample, although the evidence presented here suggests that these very low barriers are rather ubiquitous. It is possible that the approximations involved in finding transition states by the original activation-relaxation technique (ART) produce a bias towards high energy barriers. The present results are converged to much higher precision, albeit for smaller supercells, and may lead to a bias towards rearrangements with low energy barriers. Malek and Mousseau[227] have subsequently employed a hybrid eigenvector-following technique that should produce essentially equivalent results to ours if the PES is sampled in the same way. Recent discussions with one of these authors suggest that their results are essentially consistent with ours: the apparent differences arise from their tendency to focus on uphill barriers, and ours to focus on downhill barriers.[228]

The low energy peaks we have found in the barrier distributions do not appear to manifest themselves in previous experimental and theoretical studies,[139,140,143,144] and we will comment further on this observation in §4.3.3. When the three-body term is increased by 50%, in sample SW1.5, the downhill barrier distribution retains the same form, although the principal peak is broadened and maximum is shifted to higher energy. The uphill barrier distribution is radically affected, becoming virtually constant, up to an energy of about $2.5\,\epsilon$.

Table 4.3 shows that databases SW1 and BLJ11 have anomalously high peaks in their uphill barrier distributions. In Table 4.2 the lowest energy minimum in sample SW1 is only $0.0017\,\epsilon$ lower than the starting minimum, while for BLJ11 the difference is only $0.012\,\epsilon$. These results suggest that these minima may lie in regions where there are few pathways with low energy barriers that allow relaxation to minima of lower energy. This situation would arise if the minima are at the bottom of deep funnels[153] or the 'megabasins' proposed by Stillinger.[10] In Stillinger's picture such features are expected to exist for the binary Lennard-Jones system, which is reasonably 'fragile', but not for silicon, which is 'strong'. The maxima in the uphill barrier distributions at

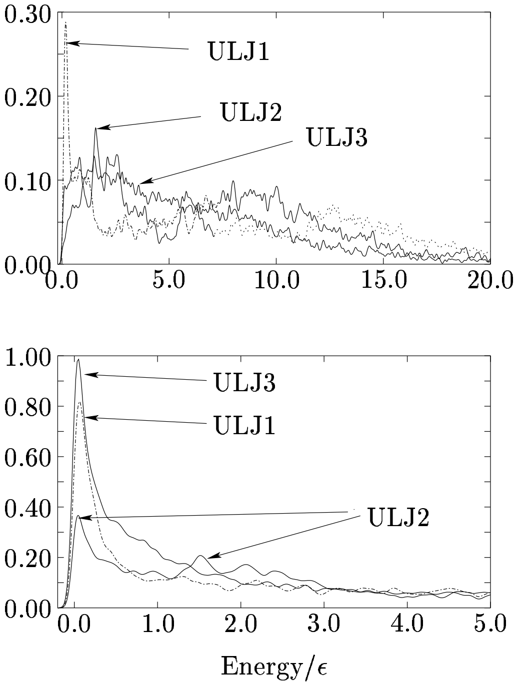

Figure 4.6: Uphill (top panel) and downhill (bottom panel) barrier distributions for the unit density Lennard-Jones databases. The Gaussian width used to construct the distribution was $s = 0.05\,\epsilon$ and the barriers are in ϵ per supercell.

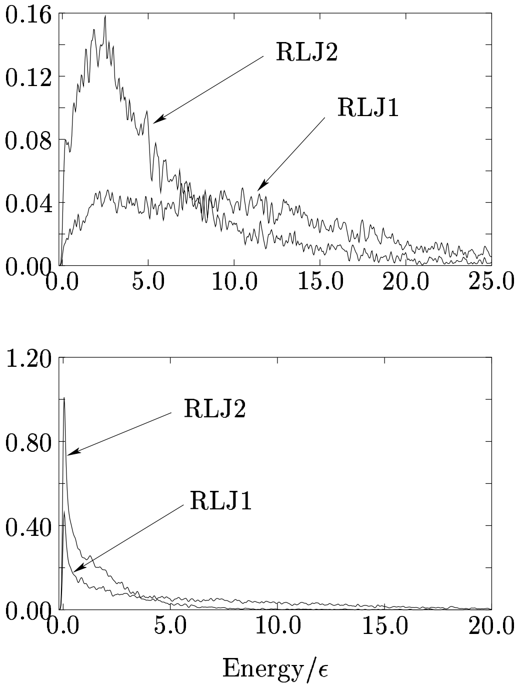

Figure 4.7: Uphill and downhill barrier distributions for the relaxed Lennard-Jones (RLJ) databases. The Gaussian width used to construct the distribution was $s = 0.05\,\epsilon$ and the barriers are in ϵ per supercell.

anomalously high energies, suggest that the regions of configuration space in question are effective kinetic traps.

In fact, the way that databases BLJ11 and SW1 were generated probably explains the above observations. Database BLJ11 was started from the final configuration generated by an MD cooling run, as the temperature of the system approached zero. The starting configuration for SW1 is the lowest in energy from the intermediate SS1 database (see the Appendix), but has no atoms in a crystalline environment. Hence it would not be surprising if both starting configurations lie at the bottom of a funnel or a monotonic sequence basin.[153, 176, 177]

Also of interest is that database RLJ2 contains a minimum of lower energy than all those in RLJ1, despite being started at higher energy. Closer examination of the rearrangements in database RLJ2 shows that there are several highly asymmetric processes, with uphill barriers of order $100\,\epsilon$, and downhill barriers of order $1\,\epsilon$. These processes link high energy amorphous configurations to minima that are predominantly crystalline, with values of the appropriate order parameter, Q_6, increasing from around 0.1 to 0.4. This reveals the presence of fast crystallisation in some regions of the PES.

The general trend of all the uphill barrier distributions, especially for RLJ1 and RLJ2, is that the barrier distributions corresponding to stationary points higher up the PES tend to be peaked at lower energy. This, combined with the relative invariance of the downhill barrier distributions, suggest that these systems have regions of their PES that act as effective kinetic traps.

Two previous studies[211,229] have reported correlated motion of atoms in successive rearrangements for BLJ systems, but we have not investigated this phenomenon in the present work.

4.3.2 PATH LENGTHS, DISTANCES AND COOPERATIVITY INDICES

The PES can be further analysed using the integrated path length, S, and the distance in configuration space, D, between two connected minima. The integrated path length, S, is estimated as a sum over steps, m, from the approximate steepest descent paths:

$$S \approx \sum_m |\mathbf{X}(m+1) - \mathbf{X}(m)|, \tag{4.1}$$

where D is simply the modulus of the $3N$-dimensional vector separating the two minima in configuration space.

A measure of the localisation of rearrangement i is given by the cooperativity index, $\widetilde{N}_i$,[181,230] defined as N/γ_i, where γ_i is the moment ratio of the displacement:

$$\gamma_i = \frac{N \sum_\alpha^N |\mathbf{r}_\alpha(s) - \mathbf{r}_\alpha(t)|^4}{\left(\sum_\alpha^N |\mathbf{r}_\alpha(s) - \mathbf{r}_\alpha(t)|^2\right)^2}. \tag{4.2}$$

$\mathbf{r}_\alpha$ denotes the position vector of atom α, and s and t are the initial and final configurations in rearrangement pathway i. $1 \leq \widetilde{N} \leq N$: $\widetilde{N} = 1$ corresponds to a totally localised event, in which only one atom moves, while all atoms move an equal distance in the other extreme.

There seems to be little variation of S, D, and $\widetilde{N}$ between the binary Lennard-Jones databases, except that the less extensively searches databases (BLJ1-3) have slightly lower average path lengths, but in the unit density homogeneous system (ULJ) there is a striking increase in all three with increasing energy of the minima in the database, i.e. from ULJ1 to ULJ3, probably owing to the increasing disorder of the samples. This result suggests that rearrangements with large path lengths, distances and cooperativity indices will become more accessible as the sample becomes more disordered. We also note that databases ULJ1 and ULJ2 contain minima with significant crystallinity, so it is perhaps surprising that their properties are not more different. The only other significant trend is that increasing the three-body term in Stillinger Weber silicon by 50 % appears to increase the distances and path lengths between minima, and decreases the cooperativity of the rearrangements.

Using a 1000-atom supercell Barkema and Mousseau[140] characterised rearrangements in amorphous silicon as highly cooperative, with typically about 50 atoms moving more than 0.1 Å. This number is larger but of a similar order to $\widetilde{N}$ for representative rearrangements found in the present work for the same system using a smaller supercell.

4.3.3 Nondiffusive and diffusive rearrangements

The peaks in the overall barrier distributions that we have obtained tend to be at surprisingly low energy. This is particularly true for Stillinger-Weber silicon, where Barkema and Mousseau have previously provided a systematic classification of the rearrangements that they characterised for *a*–Si,[140, 142] and they found that the barrier distribution tended to peak at around 4 eV. Experimental evidence suggests that there is a lower bound for the barrier to relaxation in *a*–Si of 0.23 eV.[143]

There is a slight 'double-hump' form to the barrier distributions for the unit and relaxed homogeneous Lennard-Jones systems (ULJ and RLJ, Figures 4.7 and 4.6), with a principal maximum at an energy of about $0.1\,\epsilon$ per supercell and a subsidiary maximum or point of inflection around an energy of $1.4\,\epsilon$ per supercell. This is particularly pronounced for the ULJ2 database. Examining animations of the rearrangement pathways revealed that the two maxima correspond to different processes. We describe the mechanisms corresponding to the principal maximum as 'nondiffusive': although atoms move, there is essentially no change in the nearest-neighbour coordination. These mechanisms are similar to the 'cage-rattling' processes observed in a system of hard spheres by Doliwa and Heuer,[231] who suggested that they correspond to the 'fast' β

process observed in the region of T_c, the critical temperature of mode-coupling-theory. These authors suggested that α processes correspond to mechanisms in which particles leave their cages. Despite the similarities between cage-rattling processes and the rearrangements we have found here they are not identical because cage-rattling processes correspond to vibration about a single potential minimum. The nondiffusive rearrangements found in the present work correspond to distinct minima separated by energy barriers. As the size of the effective cage increases, the rearrangements become more like the vacancy migrations previously characterised for fcc solids.[232,233] Mechanisms corresponding to readjustments of 'tight' cages—with radii similar to the mean nearest-neighbour distance—are unlikely to contribute significantly to diffusion or other transport processes, as there is no real change in the coordination of the atoms. We will therefore refer to them as 'nondiffusive'. We also suggest an alternative definition for megabasins (or 'metabasins'):[234,235] these are sets of minima that are only internally connected by nondiffusive rearrangements. This corresponds with the observation that diffusion is a random walk between megabasins, provided that the inter-basin barriers are much greater than those corresponding to intra-basin transitions.

The second maximum does indeed correspond to the movement of atoms between adjacent coordination shells, and these mechanisms are clearly 'diffusive'. Intuitively this result makes sense, as the activation energy is of the order of ϵ per supercell, the pair well depth of the Lennard-Jones model. An example of a rearrangement similar to vacancy creation in crystalline solids is illustrated in Figure 4.8. Free volume in minimum 1 is changed into a vacancy in minimum 2. These rearrangements will contribute to diffusion much more than the nondiffusive processes, as the nearest-neighbour contacts change, although they entail higher activation energies.

The tails of the barrier distributions of the homogeneous Lennard-Jones systems ULJ and RLJ contain more exotic rearrangements, such as the one illustrated in Figure 4.9, in which a pair of atoms exchange positions in a reasonably crystalline local environment. This degenerate rearrangement[226] (between permutational isomers) has a barrier of $18.7\,\epsilon$ (per supercell), and a cooperativity index (§4.3.2) of 2.00. A significant degree of bond stretching in the transition state is visible, reflecting the high barrier. In other parts of the supercell, not shown in this figure, there must exit a corresponding degree of compression, causing the high barrier.

The nondiffusive rearrangements can be quite successfully separated from the diffusive processes by counting the number of atoms whose positions at the end points of

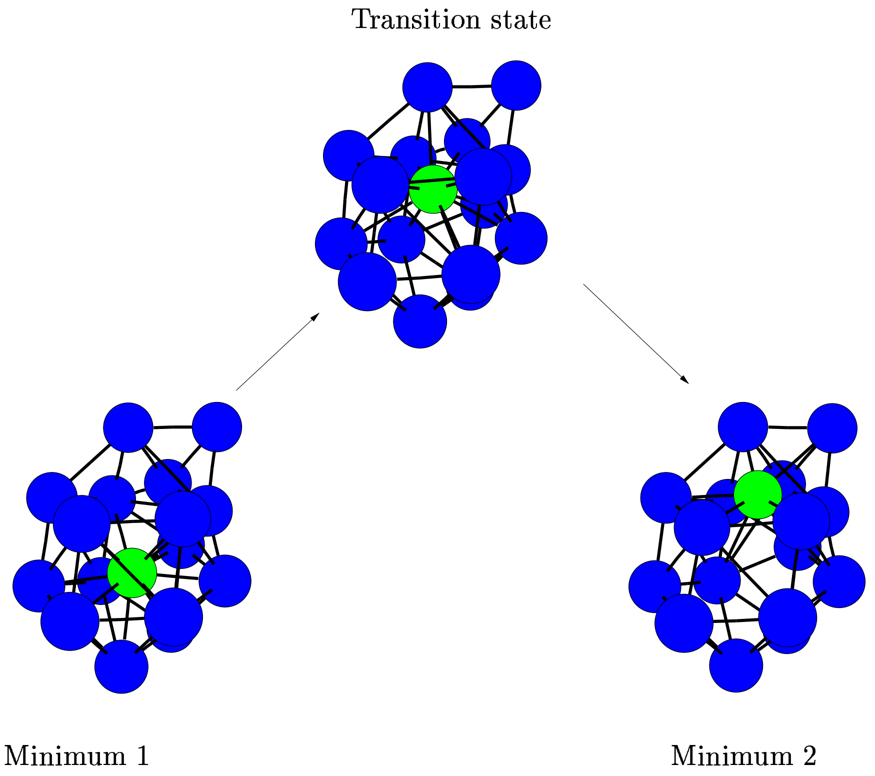

Figure 4.8: Rearrangement illustrating a change in coordination of the highlighted atom and vacancy creation in unit density Lennard-Jonesium (ULJ). The downhill barrier is $1.55\,\epsilon$ and the uphill barrier is $6.07\,\epsilon$ per supercell. The distance between the two minima is $D = 1.01\,\sigma$ and the cooperativity index is $\widetilde{N} = 1.13$. These quantities are defined in §4.3.2.

the rearrangement differ by a threshold value. We define nondiffusive rearrangements as those in which no atoms move by more than the threshold distance, and all other rearrangements are then classed as diffusive. A suitable threshold distance corresponds to about half the equilibrium pair separation, depending on the potential. Obviously there are many rearrangements whose classification is sensitive to the precise value of the threshold distance. These are intermediate between nondiffusive rearrangements and vacancy migrations. Nevertheless, separate barrier distributions with distinct peaks can be obtained using the above definition.

The uphill and downhill barrier distributions for diffusive and nondiffusive processes for database SW3 using a threshold distance of $0.8\,\sigma$ are shown in Figure 4.10. Although the distributions overlap, they peak at significantly different energies, suggesting that the ‘threshold distance’ criterion is meaningful. Furthermore, the diffusive downhill barrier distribution peaks at around $0.5\,\epsilon$, corresponding to about $1\,\mathrm{eV}$, agreeing fairly

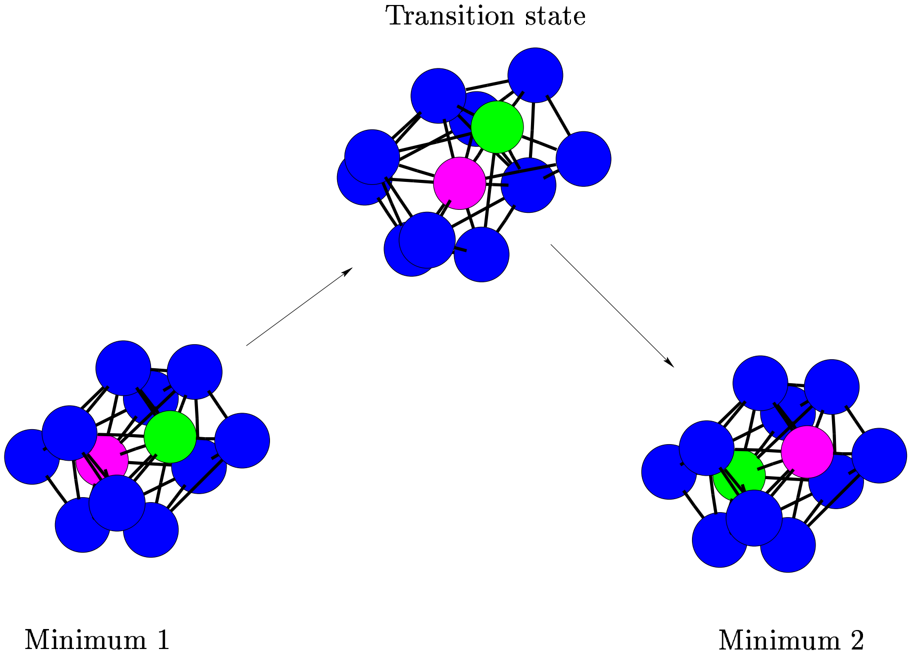

Figure 4.9: Degenerate rearrangement[226] illustrating the exchange of two atoms (shaded black and white) in unit density Lennard-Jonesium (ULJ). The configurations involved in this rearrangement are reasonably crystalline. The barriers are both 18.70 ϵ per supercell, the distance between the two minima is $D = 1.54\,\sigma$ and the cooperativity index is $\widetilde{N} = 2.0$. These quantities are defined in §4.3.2.

well with experiment. This result suggests that we would class the mechanisms found by Barkema and Mousseau as diffusive, because they lead to a change in coordination, and that the 'nondiffusive' processes have little direct effect on relaxation. We suggest that the PES for a–Si contains many relatively deep funnels, in which the intra-funnel processes are nondiffusive, and fast, while the inter-funnel processes are diffusive, and slow. Structural relaxation takes place via inter-funnel motion, with inter-funnel barriers corresponding to those observed experimentally[143] and theoretically by Barkema and Mousseau.[140,142] The Arrhenius temperature dependence of relaxation processes in strong liquids such as a–Si suggests that the barrier distribution for *diffusive* processes is similar throughout the PES, which is not inconsistent with our results. However, the present multi-funnel picture contrasts with the 'uniformly rough' view of strong glass formers.[10]

The tetrahedrally coordinated open network structure of a–Si also enables nondiffusive processes to be described as relative motion of tetrahedra, whereas in diffusive

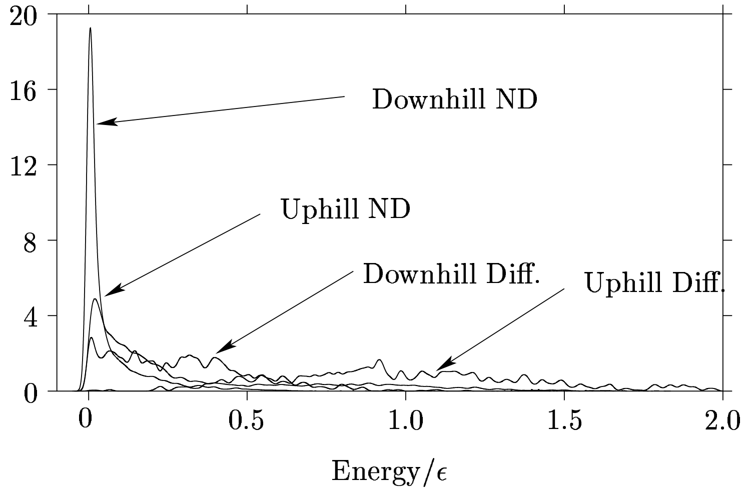

Figure 4.10: Uphill and downhill barrier distributions for Stillinger-Weber Silicon database SW3, with diffusive (Diff.) and non-diffusive (ND) rearrangements separated using a threshold distance of $0.8\,\sigma$. The Gaussian width $s = 0.005\,\epsilon$ and the barriers are in ϵ per supercell.

processes, the coordination of tetrahedra changes. These processes seem analogous to the high and low frequency modes observed by Elliott and Taraskin.[44]

This distinction between the nondiffusive and diffusive rearrangements can also be made for the BLJ systems, although it is not manifested so clearly. The threshold distance criterion is also applicable.

4.3.4 VIBRATIONAL DENSITIES OF STATES, THE 'BOSON PEAK', AND TWO-LEVEL SYSTEMS

The geometric mean frequency of the normal modes, $\prod_{i=1}^{3N-3}(\nu_i)^{1/3N-3}$ is of interest, as it directly affects the rate of crossing of potential energy barriers:[183–185, 236] the higher the geometric mean is, the faster potential barriers are crossed in the limit where the well-to-well dynamics are Markovian.

Furthermore, the vibrational contribution to the entropy at a minimum in the classical limit, S_{vib}, is given by:

$$S_{vib} = k_{\rm B}(3N-3)\left[1 - \log\left(\frac{h\overline{\nu}}{k_{\rm B}T}\right)\right], \tag{4.3}$$

The vibrational contribution to the entropy has recently been related to Angell's classification of glass-forming liquids as 'strong' and 'fragile'.[69, 122] The vibrational frequencies

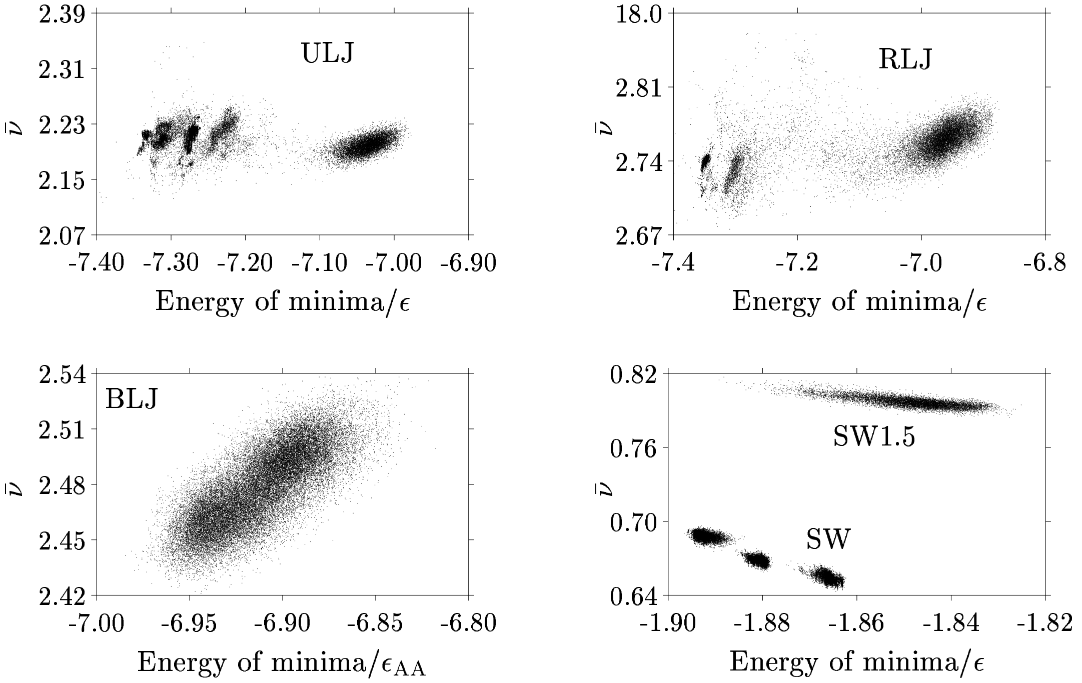

Figure 4.11: Geometric mean normal mode frequencies, plotted against the energies of the minima to which they correspond.

may also contribute to the excess entropy of the glass over the liquid.

The dependence of the frequencies on the potential energy of the local minima is illustrated in Figure 4.11, for all four systems studied. Recent studies of a model for glassy materials by Wales and Doye have suggested that high vibrational frequencies enable the system to relax faster, thus exploring deeper regions of the PES where non-Arrhenius and non-exponential behaviour takes place.[122] Thus, high vibrational frequencies may be related to fragility.

In Figure 4.11, the BLJ system shows a marked increase in the geometric mean of the normal mode frequencies, while the Stillinger-Weber system shows the opposite trend. The behaviour of the homogeneous Lennard-Jones system is intermediate: a small increase in mean vibrational frequency is visible at higher energies. The frequencies in the relaxed system are around 20% higher than those of the unit density system, in agreement with Wales' model for the scaling of the vibrational frequencies with density described in the Appendix to this Chapter and Ref 237.

The above results are consistent with the observed fragility of the BLJ system, and the relative strength of the SW system. However, some caution should be taken in

Table 4.4: Geometric mean normal mode frequencies, and energies for the 60-, 256- and 320-atom lowest lying crystalline minima, at density 1.2, compared with the minimum and maximum values in sample BLJ1. Only energies and frequencies for the Stoddard-Ford truncation with cutoff $2.5\,\sigma_{\alpha\beta}$ are given. The energies are in units of ϵ_{AA} per atom, and the frequencies are in units of $\left(\epsilon_{\mathrm{AA}}/m\sigma_{\mathrm{AA}}{}^2\right)^{1/2}$.

	E_{min}	$\overline{\nu}$
60-atom supercell	-7.08	2.37
256-atom supercell	-7.20	2.47
320-atom supercell	-7.33	2.34
Sample of 9275 amorphous 256-atom minima (minimum and maximum values)	-7.05 , -6.85	2.41 , 2.53

this interpretation, as it is expected that these results may be strongly dependent on pressure. Constant pressure results, detailed in §4.4 will provide verification.

Comparison of the geometric mean vibrational frequencies of the crystalline minima for the BLJ system from the previous chapter with the maximum and minimum values from database BLJ1 are presented in Table 4.4. The phonon wavelengths are bounded by the box lengths of the supercells: hence the normal mode frequencies have a minimum value depending on the supercell size. Naively, one might expect that $\overline{\nu}$ would decrease with increasing supercell size. The values of $\overline{\nu}$ are presented in Table 4.4 for the lowest energy crystalline minima of the 60-, 256- and 320-atom systems. The geometric mean for the partially crystalline 256-atom minimum is in the middle of the range of values of $\overline{\nu}$ for the amorphous minima. The 60- and 320-atom systems have similar, but slightly lower mean vibrational frequencies than the amorphous minima. Thus, the results presented here suggest that the vibrational entropies of the crystalline and amorphous minima are not significantly different in the BLJ system.

Within the harmonic approximation, the eigenvalues of the mass-weighted Hessian yield the normal mode frequencies, and the components of the corresponding eigenvectors are proportional to the atomic displacements. We will focus on the eigenvalues and eigenvectors of the lowest frequency modes, as these may be involved in the boson peak.[51,52]

The vibrational densities of states (VDOS) divided by the square of the frequency,

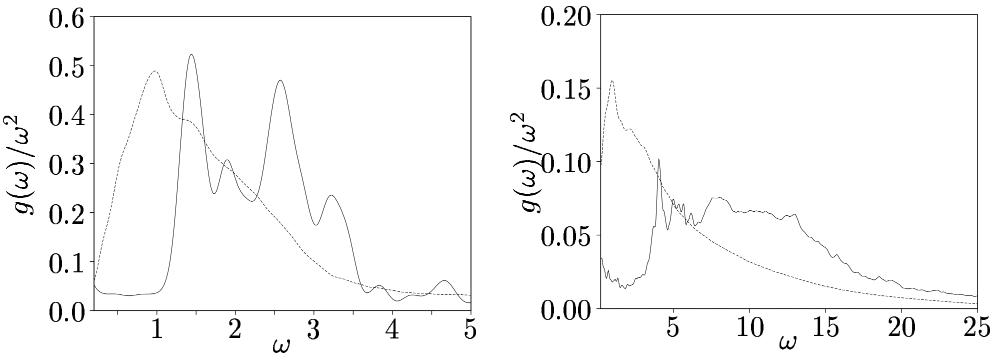

(a) SW3

(b) ULJ3

Figure 4.12: Normalised vibrational densities of states (VDOS) divided by frequency squared ($g(\omega)/\omega^2$, in units of $(m\sigma^2/\epsilon)^{3/2}$) as a function of ω (in units of $\sqrt{\epsilon/m\sigma^2}$) for databases SW3 and ULJ3 (dotted lines) compared with those for crystalline databases of minima (solid lines).

$g(\omega)/\omega^2$, are presented in Figure 4.12 for databases of both nearly crystalline and amorphous ULJ and SW samples (databases ULJ(x), SW(x), ULJ3 and SW3, respectively). The crystalline databases were generated using SS1. The Debye approximation treats the vibrations as sinusoidal waves in an elastic continuum, predicting that $g(\omega) \sim \omega^2$ up to a cutoff frequency, ν_D. For SW silicon, the reduced unit of frequency corresponds to 13.0 THz, and for the Lennard-Jones systems it corresponds to 0.47 THz (using parameters appropriate for argon).

A popular measure of the localisation of vibrational mode j is the participation ratio, p_j, which is essentially N^{-1} times the inverse of the moment ratio of the atomic displacements as expressed in equation (4.2).[43–46, 238] The atomic displacements for the normal modes are obtained from the eigenvectors of the Hessian matrix. p_j varies from one for a completely delocalised mode, in which all atoms move the same distance, to $1/N$ for a mode in which only one atom moves. $p_j = 2/3$ for a sinusoidal standing wave. Several authors have found modes that are combinations of delocalised and localised components.[44–46] These contributions may have a low value of p_j, despite their partially delocalised nature, if the atomic displacements of the localised components are large.

Finite size effects are immediately obvious for the crystals: distinct peaks are visible, and there appears to be a cutoff frequency at the low frequency end of band. These phenomena are due to the finite box length restricting the possible phonon wavelengths.

The vibrational densities of states (VDOS) and variation of participation ratios for

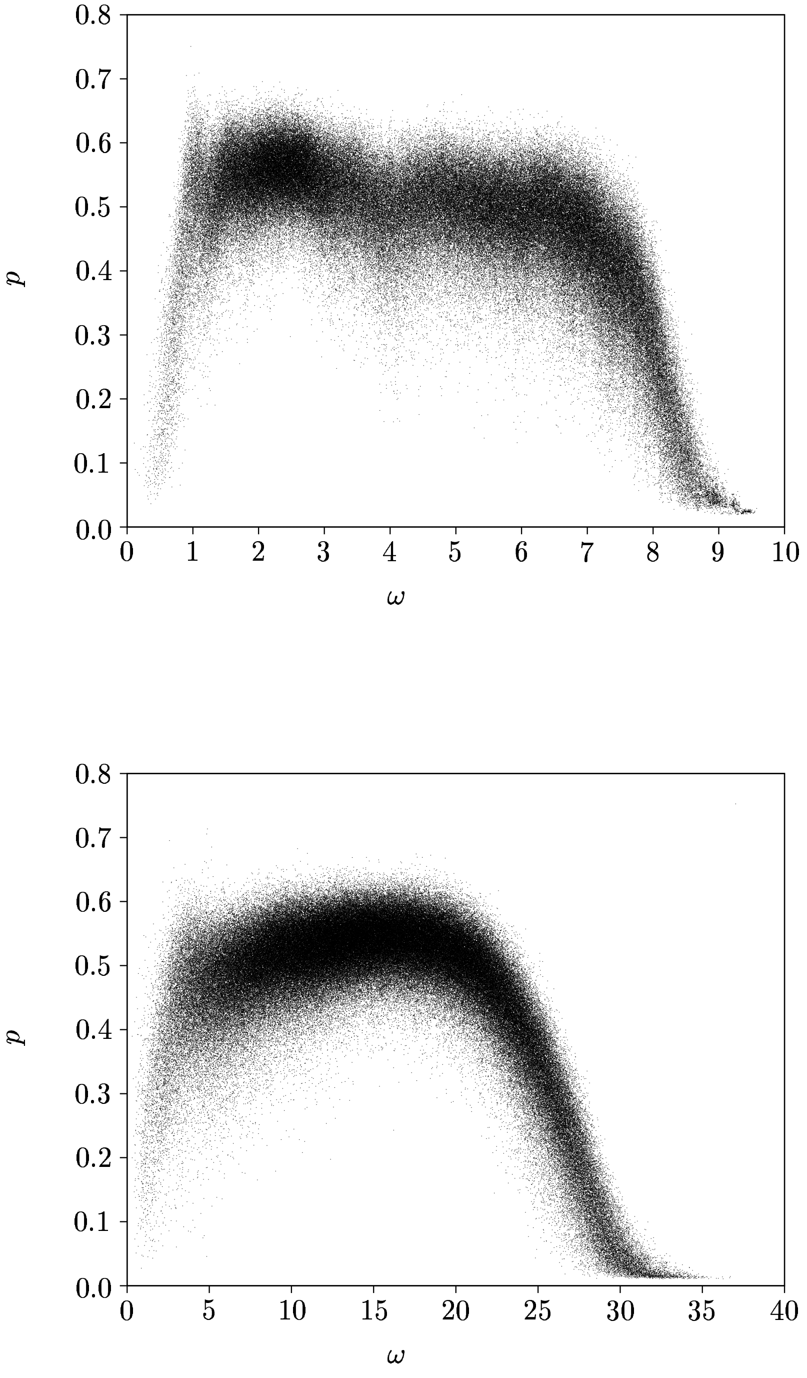

Figure 4.13: Plot of participation ratio, p, against angular frequency (in units of $\sqrt{\epsilon/m\sigma^2}$) for databases SW3 (top panel) and ULJ3 (bottom panel). p is defined in §4.3.4

the amorphous databases agree well with previous work.[46, 239] The effect of disorder on the modes is visible as an increase in $g(\omega)/\omega^2$ in the low frequency region. The participation ratios for the low frequency modes suggest significant localisation. We examined plots of the Cartesian components of the normal mode displacement vectors, $u^j_{x,y,z}$, against the projection of their positions, as used in Refs 44 and 46, but the system had too few atoms for a distinct sinusoidal component to be visible. However, localised random components are present.

If two-level systems (TLS) and the boson peak are produced by the same soft, anharmonic modes, one would expect it to be possible to verify this connection using eigenvector-following.[146–152] A good candidate for a TLS was found in database SW2, although such features are apparently experimentally absent in annealed *a*-Si,[36] so we started eigenvector-following transition state searches from one of its minima. Some adjustment of the parameters in the transition state search was required, as the potential energy surface is very flat: small step lengths ($0.005\,\sigma$) and pushoffs ($0.001\,\sigma$) were needed to prevent the search from overshooting. Minimisation was carried out using the Page and McIver steepest-descent method, with analytic first and second derivatives,[240] to ensure that the correct minima were found.

Table 4.5: Five processes with separations small enough to be two-level systems (TLS), in sample SW2. The table shows the energy of the transition state, the downhill barrier, the difference in energy ΔE, in ϵ and K, the path length, S, and distance, D between the pairs of minima.

Energy/atom	Downhill Barrier/$10^{-6}\epsilon$	$\Delta E/10^{-6}\epsilon$	$\Delta E/K$	S	D
−1.8785	139.245	1.824	0.045	0.150	0.107
−1.8806	204.286	5.4884	0.138	0.148	0.124
−1.8800	5.333	7.9904	0.201	0.067	0.057
−1.8797	18.713	20.9291	0.527	0.083	0.063
−1.8833	0.202	43.0708	1.083	0.074	0.054

Although we failed to reconverge an eigenvector-following transition state search back to the saddle point of the original candidate for a TLS, a number of new pathways were found, all with low barriers. These pathways are shown in Table 4.5. Of particular interest is the pathway with an uphill barrier corresponding to 5.28 K (per supercell) and a downhill barrier of 5.14 K per supercell, as it has an asymmetry of 0.14 K per supercell. Such results provide some evidence to support Angell's hypothesis that the low frequency modes and two-level systems are related.

4.4 CONSTANT PRESSURE

We simulated the Stillinger-Weber system at standard pressure, which corresponds to $4 \times 10^{-5}\,\epsilon\sigma^{-3}$. The pressure was set to $0.6\,\epsilon_{\rm AA}\sigma_{\rm AA}{}^{-3}$ for the binary Lennard-Jones system, because we had found for the 60-atom crystal that this gave a number density close to $1.2\,\sigma_{\rm AA}{}^{-3}$, the most popular density for simulation of this system. A further database was collected at a pressure of $1.2\,\epsilon_{\rm AA}\sigma_{\rm AA}{}^{-3}$, to investigate the effect of increasing pressure on the properties of the PES.

4.4.1 CONSTANT PRESSURE RESULTS

General properties of the databases of stationary points obtained at constant pressure are summarised in Tables 4.6, 4.7 and 4.8. The corresponding data for constant volume stationary point searches has already been presented in Tables 4.2 and 4.3. The lowest minima in databases BLJLP(x) and BLJLP1 are only $0.02\,\epsilon_{\rm AA}$ and $0.03\,\epsilon_{\rm AA}$ lower than the starting minima, respectively, implying that the starting minima are close to the bottom of a funnel. This result is not altogether surprising, as the BLJLP(x) database was initiated from a crystalline minimum obtained by global optimisation in Chapter 3, and the starting minimum for BLJLP1 was found to be close to the bottom of a megabasin at constant volume as well (§4.3.1). The lowest energy minimum in database BLJLP(x) is very similar to the starting minimum, and retained the layer of B atoms coordinated by eight A atoms. The other BLJ databases generated at a pressure of $0.6\,\epsilon_{\rm AA}\sigma_{\rm AA}{}^{-3}$ have achieved a significant degree of relaxation to lower potential energy. The lowest energy minimum in BLJHP is only $5 \times 10^{-3}\,\epsilon_{\rm AA}$ lower than the starting minimum.

The lowest energy minimum in the SWP1 database has energy $-2.000\,\epsilon$, and is a perfect crystal with the diamond structure. Thus, at constant pressure, the crystal was rapidly located using the present sampling scheme. Figure 4.14 is a simplified disconnectivity graph for this database. Once again, we use Mortenson's technique described in detail in §2.3, to group minima according to the canonical rate constants between them. Groups of minima that are joined by transitions with rates above a

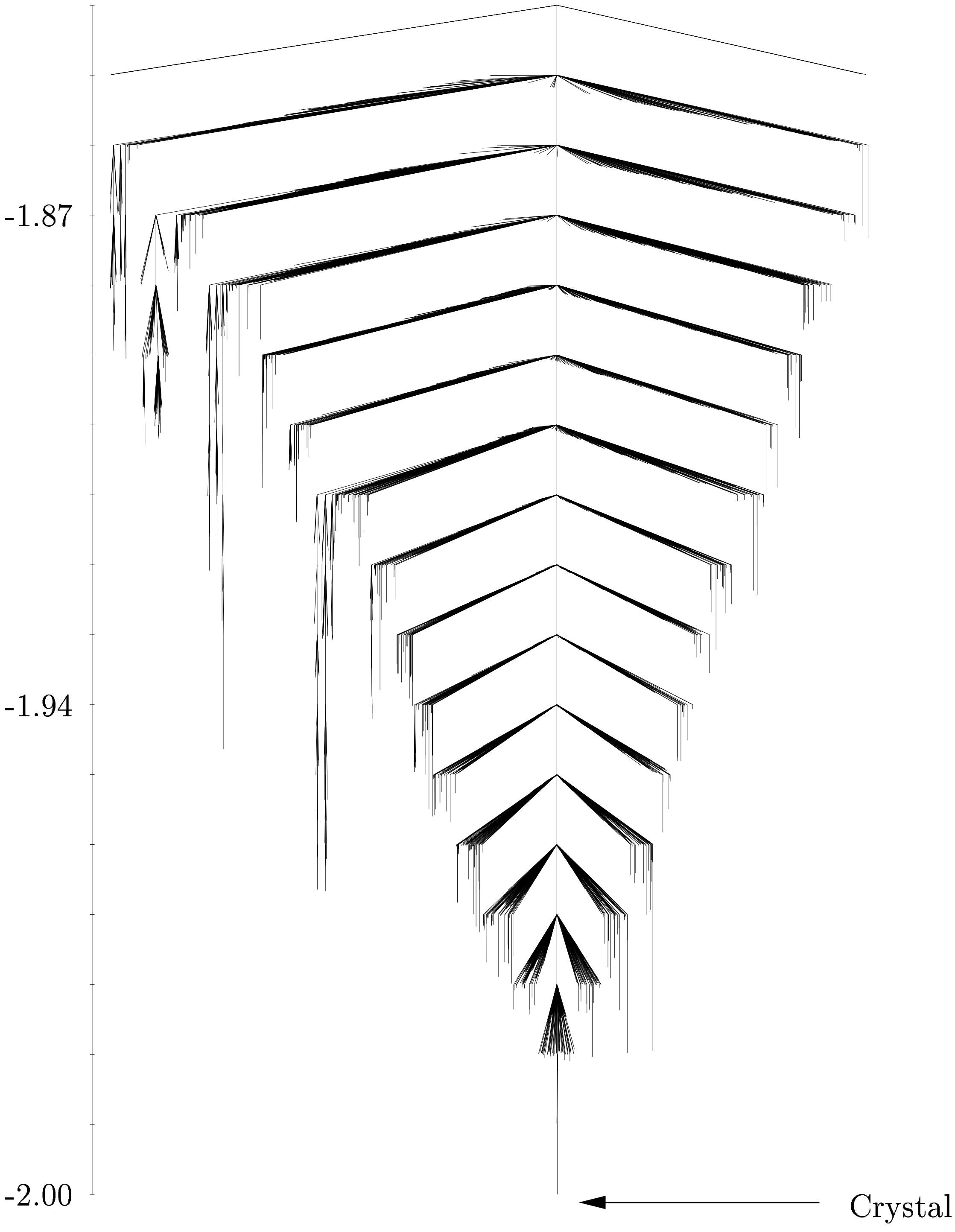

Figure 4.14: Disconnectivity graph for database SWP1. The graph was simplified using Mortenson's method described in §2.3, with a threshold rate for grouping minima of $10^{-2}\,(\epsilon/m\sigma^2)^{1/2}$, and a temperature of $0.07\,\epsilon$. The vertical axis shows the energies of the stationary points, in units of ϵ/atom. The funnelling properties of the landscape towards the crystal are clearly visible.

Table 4.6: Details of the databases studied. h_1 is the enthalpy of the initial minimum, h_{low} and h_{high} are the enthalpies of the lowest and highest lying minima, N_{min} is the number of minima in the database, and N_{ts} is the number of transition states. All the enthalpies are in ϵ per atom for supercells of 256 and 216 atoms for the BLJ and SW systems, respectively. $\langle h_{\text{min}} \rangle$ and $\langle h_{\text{ts}} \rangle$ are the mean energies of the minima and transition states, respectively. The pressure for databases BLJLP(x) and BLJLP1-3 is $0.6\,\epsilon_{\text{AA}}\sigma_{\text{AA}}{}^{-3}$, for BLJHP it is $1.2\,\epsilon_{\text{AA}}\sigma_{\text{AA}}{}^{-3}$ and for the SW databases it is $4 \times 10^{-5}\,\epsilon\sigma^{-3}$.

Database	h_1	h_{low}	h_{high}	N_{min}	$\langle \rho_{\text{min}} \rangle$	$\langle h_{\text{min}} \rangle$	$\langle h_{\text{ts}} \rangle$
BLJLP(x)	-6.7474	-6.7678	-6.5597	8754	1.24	-6.6974	-6.6894
BLJLP1	-6.4827	-6.5104	-6.4076	8994	1.22	-6.4608	-6.4576
BLJLP2	-6.4523	-6.5005	-6.3973	9159	1.22	-6.4620	-6.4586
BLJLP3	-6.3946	-6.4848	-6.3777	9285	1.21	-6.4324	-6.4290
BLJHP	-5.9931	-5.9984	-5.8903	8994	1.22	-5.9531	-5.9487
SWP1	-1.8517	-2.0000	-1.8516	9018	0.45	-1.9121	-1.9113
SWP2	-1.8453	-1.8591	-1.8265	8227	0.44	-1.8464	-1.8457

Table 4.7: Potential energies per atom of the initial, lowest and highest lying minima for the databases of Table 4.6. The potential energy per supercell is given by $E = H - PV$, where P is the pressure, V the volume of the supercell and H the enthalpy. The mean potential energies of the minima and transition states are also given.

Database	e_1	e_{low}	e_{high}	$\langle e_{\text{min}} \rangle$	$\langle e_{\text{ts}} \rangle$
BLJLP(x)	-7.2281	-7.2483	-7.0496	-7.1804	-7.1727
BLJLP1	-6.9743	-7.0010	-6.9041	-6.9540	-6.9508
BLJLP2	-6.9451	-6.9922	-6.8938	-6.9552	-6.9519
BLJLP3	-6.8917	-6.9767	-6.8750	-6.9275	-6.9242
BLJHP	-6.9686	-6.9737	-6.8798	-6.9342	-6.9301
SWP1	-1.8517	-2.0000	-1.8516	-1.9121	-1.9113
SWP2	-1.8454	-1.8591	-1.8265	-1.8464	-1.8457

threshold are considered to be in equilibrium, and are represented by a single node in the disconnectivity graph. In Figure 4.14 we used a temperature of $0.07\,\epsilon$, the melting temperature of the crystal, and a threshold rate of $10^{-2}\,(\epsilon/m\sigma^2)^{1/2}$. This procedure reduced the number of branches in the tree from 9018 to 4119, without losing any of the characteristics of the full tree. The key feature of this graph is the obvious funnel that leads to the perfect crystal. There are a few side funnels visible, which also have

Table 4.8: Pathway statistics for all the databases studied at constant pressure. We give the mean values of the integrated path lengths, $\langle S \rangle$, in σ; separations of connected minima, $\langle D \rangle$, in σ; cooperativity indices, $\left\langle \widetilde{N} \right\rangle$; the mean density of the transition states in the database, $\langle \rho \rangle$ in σ^{-3}; and the volume difference between each pair of minima linked by a single transition state, $\langle |\Delta v| \rangle$ in σ^{-3}. These quantities are defined in §4.3.2.

Database	$\langle S \rangle$	$\langle D \rangle$	$\left\langle \widetilde{N} \right\rangle$	$\langle \rho_{ts} \rangle$	$\langle \lvert\Delta v\rvert \rangle$
BLJLP(x)	2.37	1.10	1.92	1.24	0.23
BLJLP1	2.87	1.23	5.82	1.22	0.15
BLJLP2	2.85	1.19	5.08	1.22	0.15
BLJLP3	2.89	1.24	5.66	1.21	0.14
BLJHP	3.38	1.28	5.11	1.22	0.16
SWP1	1.69	0.84	4.01	0.45	0.71
SWP2	1.48	0.77	4.07	0.44	0.65

considerable crystalline character. It is very likely that there are lower energy pathways that we have not found linking these to the main funnel, increasing its funnelling ability even more. It is tempting to compare this disconnectivity graph to one generated from the constant volume database SW(x), in §3.1. However, the database from which that tree was generated used the crystal as the seed minimum, while SWP1 started from an amorphous minimum, and therefore spans a much larger energy range. Thus, while Fig 4.14 appears to be more funnel-like than its constant volume counterpart, the energy ranges of the two databases (in Tables 4.6 and 4.2 for SWP1 and SW(x), respectively) are sufficiently different to make direct comparison difficult.

The average densities of the minima in the BLJ system show no surprising variations, except that the partially crystalline database BLJLP(x) has a 2% higher density. The mean density of the minima in SWP1 is 0.45, as would be expected for the crystal, while the corresponding result for SWP2 is surprisingly low, possibly signifying the onset of crystallinity in that database too. There is no significant difference in the mean number densities of transition states compared to minima within each database.

4.4.2 BARRIER DISTRIBUTIONS

Comparison of the barrier distributions is informative. The bottom panel in Figure 4.15 shows that the downhill barrier distributions of the amorphous BLJ databases,

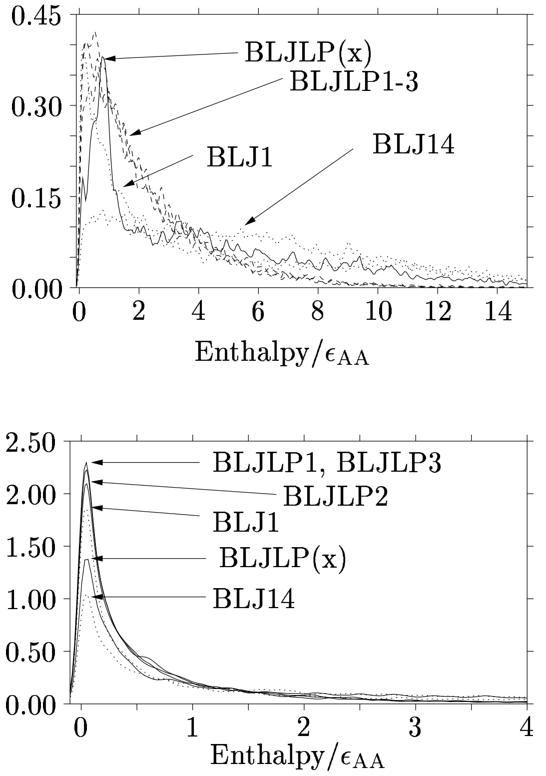

Figure 4.15: Uphill (top panel) and downhill (bottom panel) enthalpy barrier distributions for the binary Lennard-Jones samples. The energy barrier distributions for two databases collected at constant volume, BLJ1 and BLJ14, are included for comparison. The Gaussian width, $s = 0.05\,\epsilon_{AA}$ and the barriers are in ϵ_{AA} per supercell.

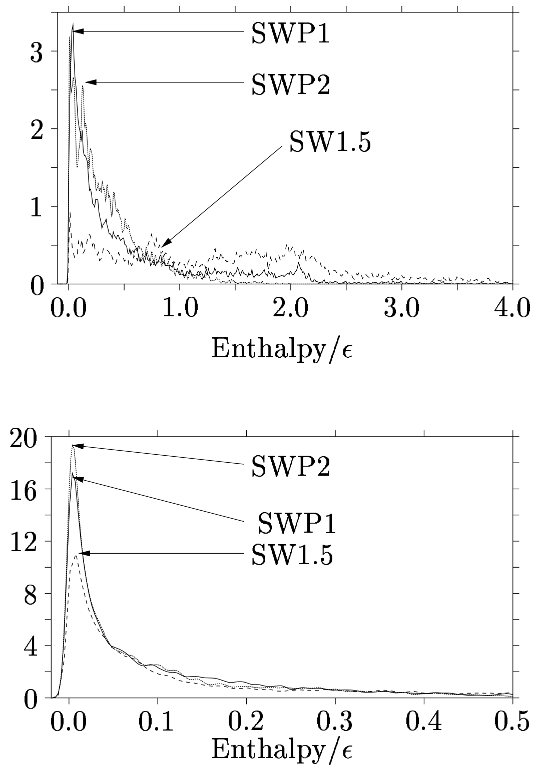

Figure 4.16: Uphill (top panel) and downhill (bottom panel) enthalpy barrier distributions for the two Stillinger-Weber silicon databases. Included for comparison are the corresponding potential energy barrier distributions for the database collected at constant volume SW1.5. The Gaussian width, $s = 0.005\,\epsilon$ and the barriers are in ϵ per supercell.

BLJLP1-3, peak at similar energies to BLJ1 and BLJ14, but with much larger amplitude. Thus, there appear to be many more low barrier rearrangements at constant pressure than at constant volume. The difference between the two sets of conditions is more pronounced in the top panel, where the BLJPV distributions peak at much lower energy than database BLJ14, and with greater amplitude. The results from §4.3.1, where we compared barrier distributions obtained using different sampling schemes, imply that this result might have physical significance.

It is perhaps surprising that the uphill and downhill barrier distributions for database

Table 4.9: Positions of the largest maxima in the downhill and uphill enthalpy barrier distributions, $H_{\mathrm{max}}(\mathrm{up})$ and $H_{\mathrm{max}}(\mathrm{down})$, respectively. The potential energy components of these barriers, $E_{\mathrm{max}}(\mathrm{up})$ and $E_{\mathrm{max}}(\mathrm{down})$, are also given. All energies are in ϵ per supercell.

Database	$H_{\mathrm{max}}(\mathrm{up})$	$H_{\mathrm{max}}(\mathrm{down})$	$E_{\mathrm{max}}(\mathrm{up})$	$E_{\mathrm{max}}(\mathrm{down})$
BLJLP(x)	0.7619	0.0618	0.8210	0.0565
BLJLP1	0.5102	0.0465	0.4807	0.0548
BLJLP2	0.6063	0.0502	0.6112	0.0525
BLJLP3	0.2229	0.0502	0.2123	0.0552
BLJHP	0.2090	0.0353	0.1764	0.0484
SWPV1	0.0390	0.0037	0.0390	0.0037
SWPV2	0.0109	0.0039	0.0109	0.0039

BLJHP both peak at lower energy than for BLJLP1 (Figure 4.18). We will explain this result in the next section (§4.4.3).

Figure 4.17 compares enthalpy and potential energy barrier distributions. In these distributions, which contain all the barriers in the sample, the PV term appears to make only a fairly small difference to the barrier height. Comparison with the constant volume results from §4.3.1 implies that allowing the box lengths to vary stabilises the transition state, thus reducing the barrier height.

The downhill barrier distributions of samples SWP1 and SWP2 appear to differ from sample SW1.5 only in as much as the amplitude of the principal maximum is slightly larger, implying a bias to lower enthalpy barrier rearrangements. The uphill distributions are strikingly different. SWP1 and SWP2 are sharply peaked at low energy in a similar fashion to those of SW1-3 in §4.3.1.

Excluding the surprisingly low energy maxima of the barrier distributions for BLJHP, it seems that allowing the box lengths to vary flattens the landscape: the downhill barriers remain relatively unchanged, while the uphill barriers decrease. In the megabasin picture of strong and fragile liquids,[10] this result corresponds to both systems becoming stronger at lower densities. This conclusion is consistent with results obtained using MD.[69]

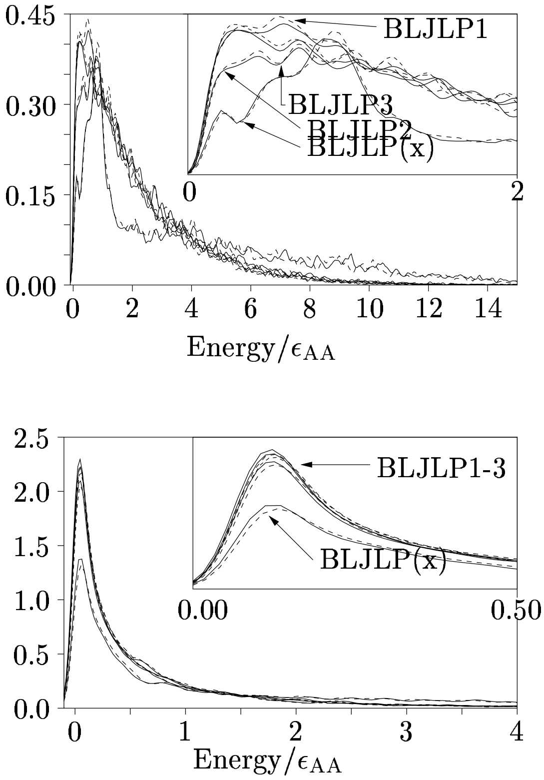

Figure 4.17: Uphill (top panel), and downhill (bottom panel) distributions of enthalpy barriers (continuous lines) and potential energy barriers (dashed lines) for the binary Lennard-Jones samples. The insets show the low energy regions of the distributions, with $0.0 < \Delta E < 2.0$ for the uphill distribution, and $0.0 < \Delta E < 0.5$ for the downhill distribution. This figure clearly shows that for a given database, the enthalpy and potential energy barrier distributions are very similar. The Gaussian width, $s = 0.05\,\epsilon_{\rm AA}$ and the barriers are in $\epsilon_{\rm AA}$ per supercell.

4.4.3 NONDIFFUSIVE AND DIFFUSIVE REARRANGEMENTS AT CONSTANT PRESSURE

In §4.3.3 we identified two types of rearrangement mechanism: nondiffusive, which we believe do not contribute directly to diffusion; and diffusive, which do. We developed a criterion to differentiate between them, by defining nondiffusive rearrangements in which no single atom moves further than a threshold distance.

We investigated the effect of pressure on the two classes of rearrangement by separating the pathways in databases BLJLP1 and BLJHP, and applying the distance criterion with a threshold value of $0.8\,\epsilon_{\rm AA}$. The results are presented in Table 4.10 and Figure 4.19. The maxima in the enthalpy barrier distributions are interesting: there is no significant difference between samples BLJLP1 and BLJHP for the nondiffusive

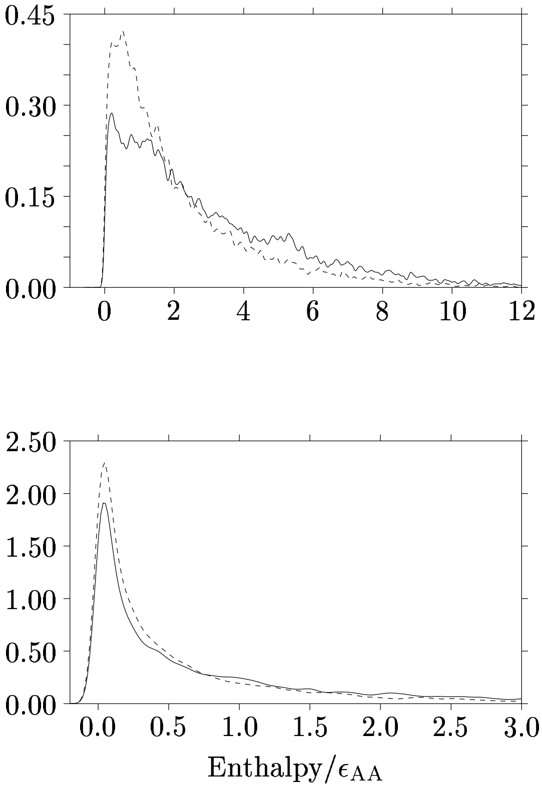

Figure 4.18: Uphill (top panel) and downhill (bottom panel) enthalpy barrier distributions for database BLJLP1 (dashed lines) and BLJHP (full lines). The Gaussian width, $s = 0.005\,\epsilon_{\rm AA}$ and the barriers are in $\epsilon_{\rm AA}$ per supercell.

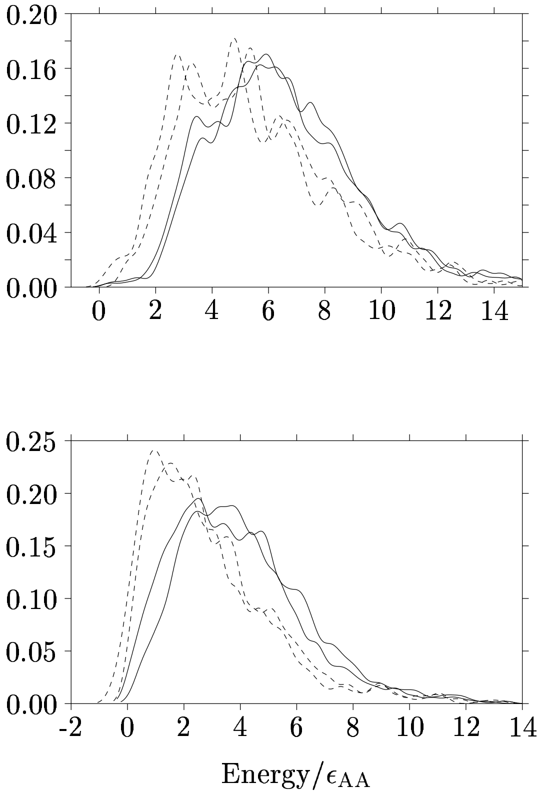

Figure 4.19: Enthalpy and potential energy barrier distributions for diffusive rearrangements in the binary Lennard-Jones system, at pressure of $1.2\,\epsilon_{\rm AA}{\sigma_{\rm AA}}^{-3}$ (full lines), and $0.6\,\epsilon_{\rm AA}{\sigma_{\rm AA}}^{-3}$ (dotted lines). As usual, the uphill distributions are in the top panel, and the downhill distributions in the bottom panel. The potential energy barrier distributions are shifted to lower energy relative to the enthalpy distributions. The barriers have units of $\epsilon_{\rm AA}$ and the Gaussian width, $s = 0.25\,\epsilon_{\rm AA}$.

processes, but the diffusive rearrangements are shifted to higher enthalpy by the increase in pressure. The number of diffusive rearrangements in BLJHP is approximately twice that in BLJLP1: 1147 and 630, respectively. We have no reason to believe that the pressure affects any bias of our searching technique towards either nondiffusive or diffusive rearrangements. Hence our results suggest that increasing the pressure in-

Table 4.10: Peaks in the barrier distributions for separated diffusive and non-diffusive rearrangements in samples BLJLP1 and BLJHP, which were obtained at pressures of 0.6 and $1.2\,\epsilon_{\mathrm{AA}}\sigma_{\mathrm{AA}}{}^{-3}$, respectively.

Database	Process type	$H_{\max}$(up)	$H_{\max}$(down)	$E_{\max}$(up)	$E_{\max}$(down)
BLJLP1	diffusive	5.35	1.54	4.77	0.95
BLJHP	diffusive	5.91	2.51	5.69	3.69
BLJLP1	nondiffusive	0.54	0.15	0.25	-0.13
BLJHP	nondiffusive	0.54	0.16	1.28	0.71

creases the number of diffusive rearrangements relative to nondiffusive rearrangements and increases the barrier heights, especially for the downhill barriers.

The increased separation between the barrier heights of nondiffusive and diffusive rearrangements explains the surprisingly low maximum in the overall BLJHP barrier distribution. In the databases collected at lower pressure, BLJLP(x) and BLJLP1-3, the low energy tail of the diffusive rearrangements and the high energy tail of the nondiffusive rearrangements overlap, creating an overall maximum of slightly higher energy. In BLJHP, the two classes of rearrangement are more separated in energy, and so this overlap is not present.

Mukherjee et al.[163] found in MD simulations that, as expected, increased pressure decreases the diffusion constant, and increases the viscosity. The barrier distributions we have presented here are consistent with that observation. The increase in the barrier heights corresponding to diffusive rearrangements and the constancy of those corresponding to nondiffusive processes support our suggestion in §4.3.3 that only the diffusive processes contribute significantly to transport processes.

It is difficult to draw conclusions about the dependence of fragility on pressure from comparing BLJLP1 and BLJHP. Jagla[241] suggested that 'single particle motion'—i.e. our diffusive processes—are characteristic of strong liquids, while 'cooperative' processes are characteristic of fragile liquids. The term 'cooperative' appears to have been used in many different ways glasses literature: Jagla uses it to describe processes in which the motion of a number of rearranging atoms in a cluster is cooperative and collective. This type of process may correspond to a sequence of nondiffusive rearrangements, in which none of the atoms in a rearranging cluster move a large difference in a single step. Thus, it appears that increasing pressure will make our BLJ system more fragile as observed by Sastry,[69] as the diffusive processes will be frozen out at higher temperature. However, the downhill barrier heights increase more than the uphill barrier heights, implying that the landscape becomes less rugged, which is characteristic of a strong liquid.

Our results can also be discussed in terms of free volume. While that theory was derived for hard spheres,[55] it is obvious that increased density at the transition state will force the rearranging atoms closer together, into the repulsive part of the Lennard-Jones potential, increasing barrier heights and hence slowing down dynamics.

4.4.4 PATHWAY STATISTICS

In Table 4.8, we presented the pathway statistics for the databases. As before, in §4.3.2, S denotes the integrated pathlength between a pair of minima joined by a transition state, D their separation and $\widetilde{N}$ is the cooperativity index. These statistics are presented in Table 4.8. There seems to be little variation of S, D, and $\widetilde{N}$ within databases BLJLP1-3. The difference between BLJLP1-3, and BLJ11, BLJ12 and BLJ13 is striking. The databases obtained at constant volume have much greater values of all three quantities. By Jagla's hypothesis, this result would also suggest that the databases BLJLP1-3 have stronger characteristics than their constant volume counterparts, as the cooperativity of the rearrangements has decreased significantly. This trend also holds for the SW silicon databases. The ratio of $\langle S\rangle$ to $\langle D\rangle$ for BLJHP is considerably higher than for BLJLP1, implying that the greater pressure increases the curvature in configuration space of the transition paths.

$\langle S\rangle$, $\langle D\rangle$, and $\left\langle\widetilde{N}\right\rangle$ are even lower for database BLJLP(x) than for BLJLP1-3. $\left\langle\widetilde{N}\right\rangle$ is slightly less than 2 - from inspection it appears that a very large number of the rearrangements in this database are permutations of one A and one B atom.

The variations in the volume difference between pairs of minima linked by a transition state is small: the only point of interest is that it appears to be significantly greater for the SW system than for BLJ. Other authors[164,165] have observed large pressure and volume dependencies in SW silicon. Given this result, and the increase in the funnelling properties of the PES by allowing the box lengths to vary (§4.4.1), the high value of $\langle|\Delta v|\rangle$ is not surprising.

4.4.5 VIBRATIONAL PROPERTIES AND TWO-LEVEL-SYSTEMS (TLS)

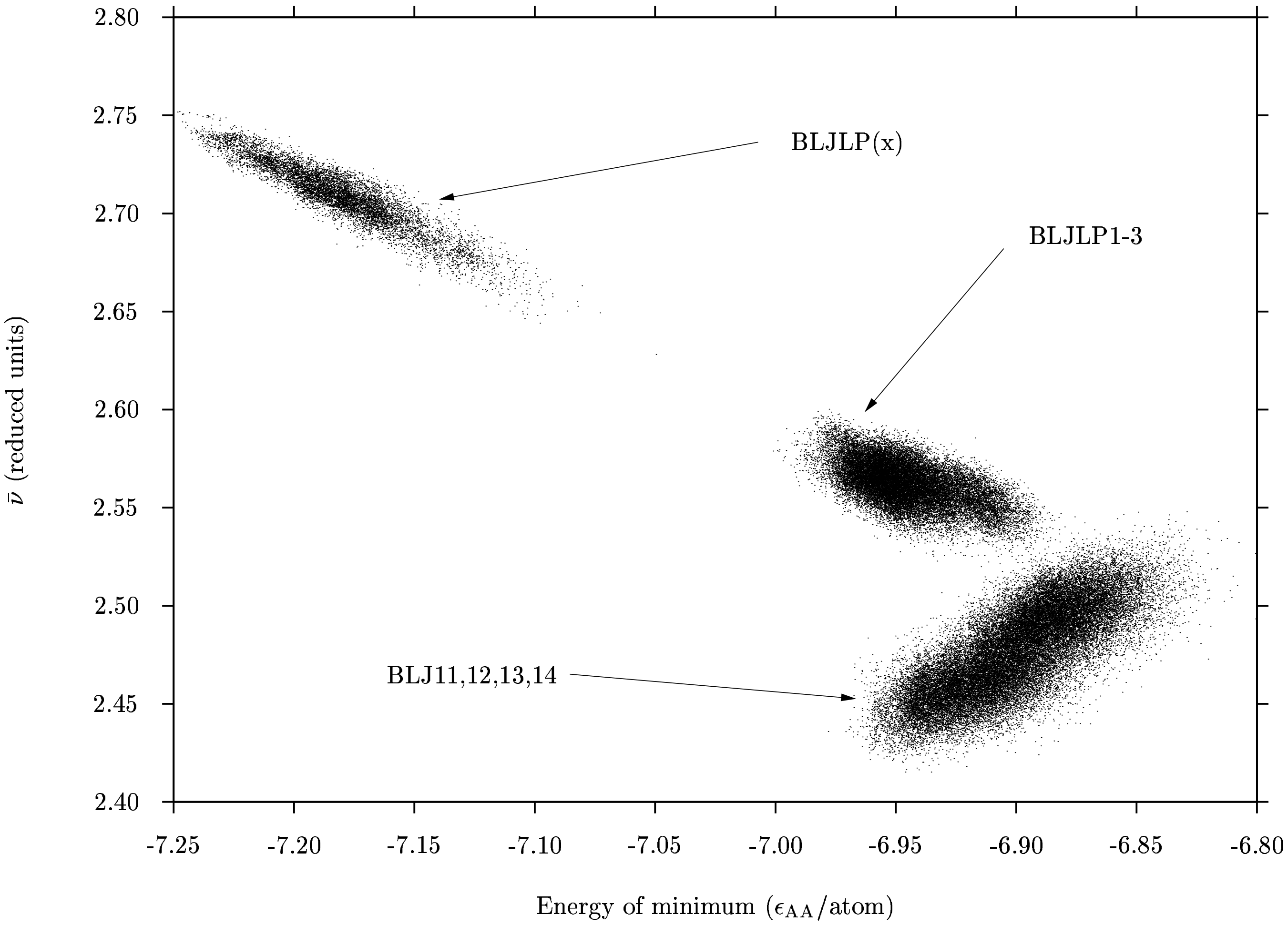

Figure 4.20: Geometric mean normal mode frequencies plotted against potential energy for all the minima in the binary Lennard-Jones databases. Included for comparison are the constant volume databases BLJ11-14. The change from an upward trend with increasing potential energy in the constant volume case to the opposite trend at constant pressure is clearly visible. For clarity, we have omitted the results from BLJHP, which show a similar trend to the other databases collected at constant pressure, but are shifted upwards slightly in frequency.

Figure 4.20 presents the geometric mean vibrational normal mode frequency at each minimum, obtained by diagonalising the matrix of second derivatives of the energy. The geometric mean of the $3N-3$ normal modes, $\bar{\nu}$, is given by $\prod_{i=1}^{3N-3}(\nu_i)^{1/(3N-3)}$. We confirmed the surprising result in that the geometric mean frequency increases with increasing energy of the corresponding minimum for the BLJ system, at constant vol-

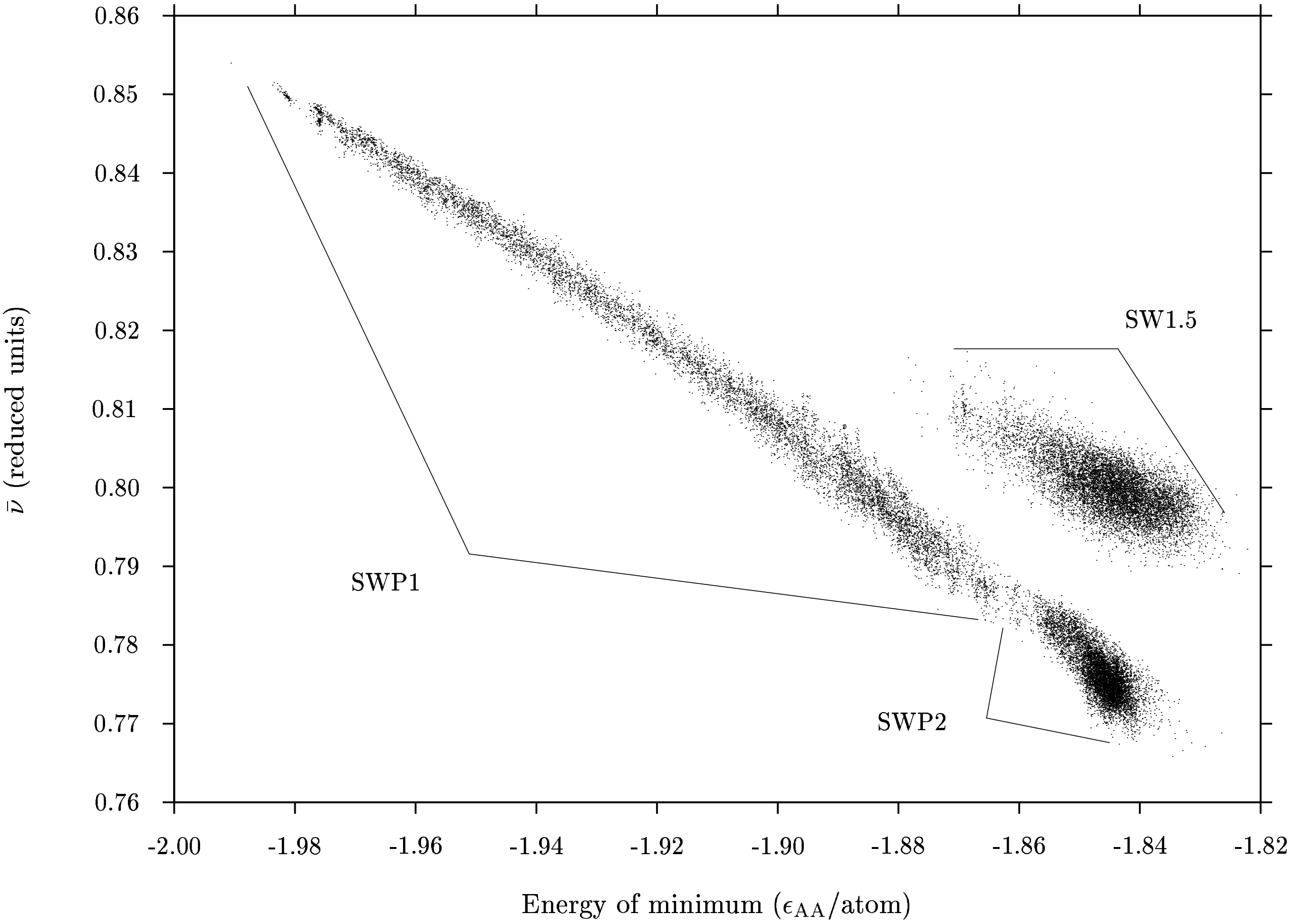

Figure 4.21: Geometric mean normal mode frequencies at each minimum, $\bar{\nu}$, plotted against potential energy for all the minima in the SW silicon constant pressure databases (SWP1 and SWP2), with the constant volume database SW1.5 for comparison.

ume. Sastry had previously obtained the same result,[69] and attributed the increasing fragility of the system as the number density increases to this anomalous behaviour. Here we compare the results for BLJLP(x) and BLJLP1-3 with BLJ11-14 from §4.3.4. The constant volume trend is reversed at constant pressure, as expected. The crystalline database, BLJLP(x), has considerably higher geometric mean frequencies, but appears to follow the same average trend as the amorphous databases, BLJLP1-3. Low frequency modes, which may contribute to the boson peak, affect the geometric mean frequency. The correlation between increasing disorder, increasing energy and increasing amplitude of the boson peak has been reported by Angell.[38] Our results appear to be consistent with this correlation.

For clarity, the results from BLJHP have been omitted from Figure 4.20. They show a similar spread and energy dependence to the results from BLJLP1, with a shift upwards in frequency of 0.04 reduced units.

The vibrational properties of the SW databases exhibit the expected behaviour, with only a downwards shift of about 0.02 reduced units from constant volume to constant pressure. We found only one candidate for a two-level system (TLS) in the SW databases.

4.5 SUMMARY

The classification of the rearrangements as diffusive or nondiffusive reveals a significant difference between the 'strong' system (SW silicon), and the 'fragile' systems (Lennard-Jones). In the LJ systems the diffusive rearrangements generally have barriers about one order of magnitude greater than the nondiffusive, while in the SW system the barriers corresponding to the two types of rearrangement differ by about three orders of magnitude. This observation, if it can be generalised, leads us to suggest a multi-funnel character for the energy landscapes of both strong and fragile glass formers, in contrast to the 'uniformly rough' picture.[10] However, if we coarse grain the picture by averaging over the fast processes that do not contribute to diffusion then the 'uniformly rough' view may be recovered. If this picture is correct then the nondiffusive processes in strong glass formers will be fast, and the α processes may not be seen in dielectric relaxation experiments because they are frozen out. Hence, the effective barriers to transport dynamics such as diffusion would be those for the inter-funnel α processes, which correspond to a number of elementary rearrangements, in accord with Stillinger's suggestion.[10] Experiment suggests that these effective barriers do not vary significantly throughout the PES, in agreement with our results, as relaxation processes tend to have Arrhenius temperature dependence in 'strong' liquids.

In fact, none of our barrier height distributions show much variation with the energy of the local minima involved, a result that highlights the importance of the actual connectivity of the PES for dynamics. In the model fragile liquids considered in the present work, the distinction between diffusive and nondiffusive processes is much less pronounced than in the strong systems. The energy landscape may therefore have shallower funnels, and it could be this feature that leads to non-Arrhenius behaviour and stretched exponential relaxation.

The minima that we have found exhibit the increased low frequency VDOS expected for disordered systems, and we have characterised several two-level systems in the SW databases. The eigenvector-following approach should be able to clarify the relationship of soft vibrational modes to low-lying transition states.

The constant pressure results show that the presence of low barriers is not an artefact of simulation with constant supercell dimensions. The marked decrease of both nondiffusive and diffusive uphill barriers as the pressure is allowed to vary are indicative of a 'flattening' of the PES, implying that the system becomes less fragile according to Stillinger's picture of of the PES.[10] The validity of the threshold distance criterion is reinforced by the insensitivity of the barriers for nondiffusive rearrangements to the pressure, and the large increase in the barriers to diffusive processes as the pressure is raised.

The principal conclusion of the work in this chapter is that the anomalous dynamics of glasses and supercooled liquids cannot be explained by the distribution of barriers to elementary rearrangement pathways alone. The focus of the next chapter will be to identify whether this complex phenomenology is a consequence of the connectivity of minima, or some other properties that cannot be included in the simple picture of the PES as a collection of minimum—saddle—minimum elementary pathways.

APPENDIX: SCALING OF VIBRATIONAL FREQUENCIES WITH DENSITY

In view of the likely importance of the variation in the vibrational frequencies of the system with density Wales has developed a simple theory to predict this property.[237] Consider a single atom that interacts with the walls of a spherical container, radius R, according to a potential V. For an infinitesimal element of the surface distance d from the atom the contribution to the potential energy is

$$\frac{V(d)R^2 \sin\theta d\theta d\phi}{4\pi R^2}, \tag{4.4}$$

where θ and ϕ are spherical polar coordinates. The distance from the surface element, d, and the displacement of the atom from the origin, r, are related by $d^2 = r^2 + R^2 - 2rR\cos\theta$. Hence the integral over the sphere can be performed analytically when V corresponds to a Lennard-Jones or a Morse potential. The Lennard-Jones result is

$$V(r) = -\frac{\epsilon\sigma^6}{10rR}\left\{\frac{5}{(r-R)^4} - \frac{5}{(r+R)^4} + \frac{2\sigma^6}{(r+R)^{10}} - \frac{2\sigma^6}{(r-R)^{10}}\right\}. \tag{4.5}$$

The limit as $r \to 0$ has the usual Lennard-Jones form. This central configuration is always a stationary point with a triply degenerate Hessian eigenvalue of

$$\lambda = 8\epsilon\sigma^6(22\sigma^6 - 5R^6)/R^4, \tag{4.6}$$

so that λ changes from positive to negative as R increases through $R = \sqrt{22/5}\,\sigma$. An analytical expression for the frequency is also available if V has the Morse form,[242] but we will not use it here. The above model predicts that the leading contribution to the density dependence of the frequency should scale as $\rho^{7/3}$.

5

QUANTITATIVE STUDIES OF THE PES

The work described in the previous chapters is essentially qualitative. The next logical step is to attempt to calculate dynamical properties of model glass formers, using our methods of searching the PES. The results thus obtained can be compared to those found from either conventional simulation techniques or experiment.

The aim of this chapter is not necessarily to provide an alternative to conventional MD or MC. Searching for minima and transition states is still a computationally expensive exercise, and so MD remains the method of choice in the moderately supercooled region, in which super-Arrhenius behaviour is observed in fragile liquids. Instead, calculation of dynamical properties will enable us to understand whether the connectivity of the minima, and the magnitudes of the potential energy barriers between them can reproduce the super-Arrhenius behaviour observed in MD simulation.

At a fundamental level, the rich phenomenology of glass formers—both in the glassy and supercooled state—must originate from the PES.[1] At low temperatures, it must be the case that the dynamics are dictated by the connectivity of the minima and the barriers between them. The upper temperature limit of the range in which this interpretation is applicable is still to be determined conclusively.

5.1 KINETIC MONTE CARLO SIMULATION OF DIFFUSION

The standard method of obtaining dynamical information from databases of stationary points is the solution of the master equation (for a recent review see Ref 153), which considers the time evolution of $\mathbf{P}(t)$, where $P_i(t)$ is the probability of the system occupying the potential well corresponding to minimum i at time t. The "master" equation is the coupled set of linear differential equations:

$$\frac{dP_i(t)}{dt} = \sum_{j \neq i}^{n_{min}} \left[k_{ij} P_j(t) - k_{ji} P_i(t) \right], \tag{5.1}$$

where, in conventional chemical notation, k_{ij} is the first order rate constant *from* well j *to* well i. Conventionally, these equations are then solved by forming a transition matrix $\mathbf{W}$, where $w_{ij} = k_{ij} - \delta_{ij} \sum_{m=1}^{nmin} k_{mi}$, so the w_{ii} correspond to the total rate constant out of minimum i. $\mathbf{W}$ is not symmetric but can be symmetrised using the detailed balance condition, that $w_{ij} P_j^{eq} = w_{ji} P_i^{eq}$. Provided that $\mathbf{W}$ cannot be decomposed into block form, it has a single zero eigenvalue, with the corresponding eigenvalue the equilibrium probability vector.[243] Equation (5.1) can be integrated analytically or numerically, thus providing $\mathbf{P}(t)$, given $\mathbf{P}(0)$.

The above method of integrating the master equation is not directly applicable to either of the systems studied here, or to the properties that we wish to calculate. The alternative is solving the master equation using the kinetic Monte Carlo (KMC) technique.

5.1.1 PRINCIPLES OF KMC

In standard Monte Carlo (MC) using importance sampling, new configurations are generated by randomly perturbing the current configuration, and a move is accepted with probability $\mathrm{MIN}(1, \exp[-(E_{new} - E_{old})/(k_{\mathrm{B}}T)])$, where E_{new} and E_{old} are the potential energies of the new and old configurations, and MIN is the smaller of its two arguments. MC is successful for numerical calculation of static properties of the system, but as the method takes no account of barrier heights a 'real' timescale cannot be associated with it, and therefore dynamic properties cannot be calculated. Kinetic Monte Carlo (KMC) uses a different criterion for its importance sampling, thus associating a timescale with each step, allowing dynamic properties to be obtained too.

Fichthorn and Weinberg[244] were the first to put KMC on a firm theoretical footing. Using the theory of Poisson processes, they showed that both static and dynamic properties could be calculated using MC, provided that:

1. There exists a set of transition probabilities, which form a so-called 'dynamical

hierarchy'.[244] For this condition to be satisfied, the transition probabilities must be weighted according to an appropriate rate theory, and obviously $w_{ji} \leq 1$. As above, w_{ji} represents the transition probability from configuration i to j. Thus, the w_{ji} of the Metropolis criterion do not satisfy a dynamic hierarchy, because the transition probabilities to all states of lower energy are unity and equal.

2. Time increments are calculated appropriately.

3. The events are independent: underlying Markovian dynamics are assumed. This means that it is assumed that the w_{ij} are independent of the history in reaching minimum i.

For systems in which the transition probabilities may often be small, the most efficient method of propagating the trajectory is the n-fold method of Bortz, Kalos and Lebowitz.[245] This scheme 'accepts' a move at every trial, by defining the transition probabilities as follows:

$$w_{ji} = \frac{k_{ji}}{\sum_m^n k_{mi}}, \tag{5.2}$$

where k_{ji} is the rate constant from minimum i to minimum j, and there are n transitions from which to choose. We then follow the algorithm represented in Figure 5.1 to propagate the trajectory. It is worth noting that although the rate constants, k_{ij} satisfy the detailed balance criterion, the w_{ji} do not: $w_{ji}P_i^{eq} \neq w_{ij}P_j^{eq}$. The w_{ij} and w_{ji} refer to different waiting times, and when this is taken into account, the detailed balance relation for the k_{ij} is retrieved.

The residence time in the basin corresponding to a given minimum will therefore be the expectation value of the interval between entering the minimum and a transition occurring. In KMC simulation, we consider a much simplified version of the master equation (5.1), since at $\tau = 0$ our occupation probability vector $P_j(0) = \delta_{ij}$, when we make a transition to minimum i. Thus,

$$\frac{dP_i(\tau)}{d\tau} = -\sum_{j \neq i}^{n_{min}} \left[k_{ji}P_i(\tau)\right], \tag{5.3}$$

where τ is the residence time in minimum i, and $P(\tau = 0) = 1$. The solution for this differential equation, is trivial

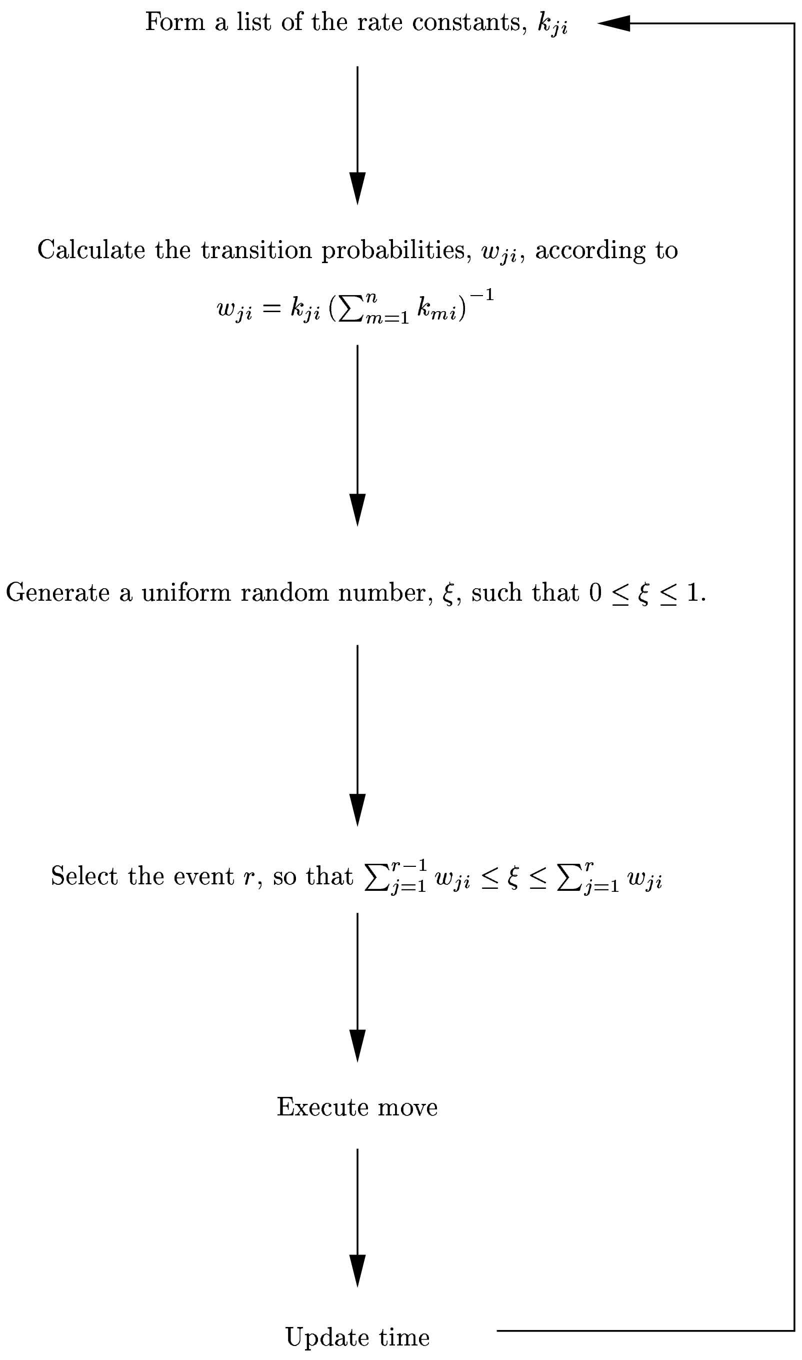

Figure 5.1: Schematic representation of the Bortz, Kalos and Lebowitz n-fold Monte Carlo algorithm.[245]

$$P(\tau) = \exp\left(-\tau \sum k_{ji}\right). \tag{5.4}$$

Thus the expectation value of the residence time is given by:

$$\langle \tau \rangle = \int_0^\infty P(\tau) d\tau = \left(\sum k_{ji}\right)^{-1}. \tag{5.5}$$

Obviously, in order for $\langle \tau \rangle$ to be exact we must obtain the rates for all the transition states connect to minimum i. Of course, even if we have the patience and computer time to search exhaustively, the accuracy of $\langle \tau \rangle$ is limited by the rate law we use to obtain k_{ij}, and the assumption that the rate constants correspond to independent Poisson processes. In practice, a representative sample of transition states is deemed sufficient. If a distribution of residence times is required, then we can invert equation (5.4), to yield

$$\tau = -\frac{\ln P(\tau)}{\sum k_{ji}}. \tag{5.6}$$

Thus, to calculate τ, we draw a number in the range $[0, 1]$ to represent $P(\tau)$. For most purposes, such as calculation of diffusion constants, there is no difference between calculating the residence time in this way and simply using the expectation value, $\langle \tau \rangle$.

5.1.2 THE HARMONIC SUPERPOSITION APPROXIMATION AND RATE CONSTANTS

In order to simulate a system using KMC, we need a method of obtaining rate constants for transitions between minima in the database. We start from the harmonic superposition approximation.[246–250]

We begin by writing the potential energy as a truncated Taylor expansion around the minimum, using normal mode coordinates,

$$E = E_i + \frac{1}{2} \sum_{j=1}^{\kappa} \omega_j^2 Q_j^2, \tag{5.7}$$

where E_i is the potential energy of minimum i, Q_j is a displacement along the jth normal mode of the minimum, with angular frequencies ω_j, and κ is the number of vibrational degrees of freedom: $3N-3$ for a bulk system. By definition, the normal modes are the eigenvectors of the mass-weighted Hessian, $\mathbf{H}^{\mathrm{MW}}$, where $H^{\mathrm{MW}}_{\alpha\beta} = H_{\alpha\beta}/\sqrt{(m_\alpha m_\beta)}$, and m_α is the mass of the atom corresponding to coordinate α. The kinetic energy in mass-weighted coordinates is then $E_K = \frac{1}{2}\sum_{j=1}^{\kappa}\dot{Q}_j^2$, and so the total energy is that of a collection of κ independent simple harmonic oscillators with angular frequency ω_j:

$$E_{tot} = E_i + \frac{1}{2}\left(\sum_{j=1}^{\kappa}\dot{Q}_j^2 + \omega_j^2 Q_j^2\right). \tag{5.8}$$

$\dot{Q}_j$ is simply the momentum of oscillator j as we are using mass-weighted coordinates, and so equation (5.8) is the equation for a hyperellipsoid in phase space with semi-axes $a_j = \sqrt{2\left(E_{tot} - E_i\right)}$ and $b_j = \sqrt{2\left(E_{tot} - E_i\right)}/\omega_j$. The volume of this hyperellipsoid is given by

$$\frac{\pi^\kappa}{\Gamma\left(\kappa+1\right)}\prod_{j=1}^{\kappa} a_j b_j, \tag{5.9}$$

where Γ is the Gamma function, defined thus:

$$\Gamma\left(\kappa\right) = \int_{s=0}^{\infty} s^{\kappa-1}\exp^{-s} ds. \tag{5.10}$$

For integer κ, $\Gamma\left(\kappa\right) = \left(\kappa-1\right)!$. The phase space volume, $G_i\left(E_{tot}\right)$ associated with each minimum, i, at energy E_{tot} can be defined thus:

$$\begin{aligned} G_i\left(E_{tot}\right) &= \frac{\left(2\pi\right)^\kappa\left(E_{tot} - E_i\right)^\kappa}{\kappa!\prod_{j=1}^{\kappa}\omega_j}\theta\left(E_{tot} - E_i\right), & (5.11)\\ &= \frac{\left(E_{tot} - E_i\right)^\kappa}{\kappa!\prod_{j=1}^{\kappa}\nu_j}\theta\left(E_{tot} - E_i\right), & (5.12)\end{aligned}$$

where $\nu_j = \omega_j/2\pi$ is the frequency of normal mode j and θ is the Heaviside step function. The semi-classical approximation then gives a sum of states for minimum i, $F_i\left(E_{tot}\right)$, by dividing through by h^κ:

$$F_i\left(E_{tot}\right) = \frac{\left(E_{tot} - E_i\right)^\kappa}{\kappa!\prod_{j=1}^{\kappa} h\nu_j}\theta\left(E_{tot} - E_i\right). \tag{5.13}$$

Differentiating by E_{tot} then gives the density of states, $\Omega_i\left(E_{tot}\right)$ associated with minimum i at E_{tot}:

$$\begin{aligned}\Omega_i\left(E_{tot}\right) &= \frac{dF_i\left(E_{tot}\right)}{dE_{tot}}, && (5.14)\\ &= \frac{\left(E_{tot}-E_i\right)^{\kappa-1}}{\Gamma\left(\kappa\right)\prod_{j=1}^{\kappa}h\nu_j}\,\theta\left(E_{tot}-E_i\right). && (5.15)\end{aligned}$$

The total partition function for the system is just the sum of the partition functions for each minimum, $\sum_i \Omega_i\left(E_{tot}\right)$, and so the microcanonical equilibrium occupation probability of minimum i is thus,

$$P_i\left(E\right) = \frac{\Omega_i\left(E\right)}{\sum_j \Omega_j\left(E\right)}. \quad (5.16)$$

We can also use equation (5.15) and the thermodynamic definition of the microcanonical temperature,

$$\frac{1}{k_{\mathrm{B}}T_{\mu}} = \left(\frac{\partial \ln\Omega}{\partial E_{tot}}\right)_{N,V} = \frac{1}{\Omega}\left(\frac{\partial\Omega}{\partial E_{tot}}\right)_{N,V}, \quad (5.17)$$

to derive the instantaneous microcanonical temperature associated with minimum i, $T_{\mu,i}$:

$$k_{\mathrm{B}}T_{\mu,i} = \frac{\left(E_{tot}-E_i\right)}{\kappa-1}\,\theta\left(E_{tot}-E_i\right). \quad (5.18)$$

Obviously $\kappa - 1 = 3N - 4$ for the bulk systems studied here.

We use Rice-Ramsberger-Kassel-Marcus (RRKM) theory[183–185] to obtain the microcanonical rate constants for inter-minimum transitions. RRKM theory gives

$$k_i^{\dagger} = \frac{F^{\dagger}\left(E_{tot}\right)}{h\Omega_i\left(E_{tot}\right)}, \quad (5.19)$$

$k_i^{\dagger}$ is the total rate constant out of minimum i, through transition state $\dagger$, and $F^{\dagger}\left(E_{tot}\right)$ is the semi-classical sum of states for transition state $\dagger$ with the single mode with the negative eigenvalue—the reactive mode—removed. We then obtain $F^{\dagger}\left(E_{tot}\right)$ by integrating the density of states for the saddle point:

$$\begin{aligned}F^{\dagger}\left(E_{tot}\right) &= \int_{E^{\dagger}}^{E_{tot}}\Omega^{\dagger}\left(E'\right)dE', && (5.20)\\ &= \frac{G^{\dagger}\left(E_{tot}\right)}{h^{\kappa}}, && (5.21)\end{aligned}$$

where $E^\dagger$ is the potential energy of the transition state †, and $G^\dagger\left(E_{tot}\right)$ is the associated phase space volume, summed over the $3N-4$ non-reactive modes. We then substitute equations (5.12) and (5.13) into equation (5.19) to yield the final RRKM expression for the microcanonical rate constants:

$$k_i^\dagger\left(E_{tot}\right) = \left(\frac{E_{tot}-E^\dagger}{E_{tot}-E_i}\right)^{\kappa-1} \frac{\bar{\nu}_i^\kappa}{\left(\bar{\nu}^\dagger\right)^{\kappa-1}}, \tag{5.22}$$

where, for convenience we write the products of the normal mode frequencies in terms of the geometric mean frequencies, $\bar{\nu}$ and $\bar{\nu}^\dagger$, of the minimum and the transition state with the reactive mode removed, respectively. We used microcanonical rate constants for the KMC simulations presented in this chapter, so that our KMC results would be directly comparable with the equivalent MD runs. Although there are several algorithms for isothermal MD simulations we decided to perform all our simulations using the microcanonical ensemble for simplicity. We have made two major assumptions in the derivation of these rate constants and equilibrium occupation probabilities. Firstly, we assume that the phase space hyperellipsoids associated with each minimum do not overlap, and can therefore be summed independently. The second major assumption is that the harmonic expression for the potential energy about a minimum, equation (5.7), is a realistic depiction of the PES. This assumption might prove problematic, since some near-universal properties of glass-formers, such as the low-temperature specific heat anomalies that have been attributed to the boson peak and two-level systems (§1.1.6), suggest that anharmonicity may be important. Notwithstanding this, Broderix et al. deduced that the harmonic approximation was reasonable below a temperature of $1\,k_\mathrm{B}T/\epsilon_\mathrm{AA}$[131] from MD simulations. The evidence for this suggestion was that the energy per atom of the minima sampled, e_{min}, was approximated surprisingly well by $e - 3k_\mathrm{B}T/2$, where e is the total potential energy per atom, in agreement with the harmonic approximation and classical equipartition theory.

For completeness, we include the derivation of the equivalent canonical rate constants. These were used in Mortenson's method[173] for simplifying disconnectivity trees, outlined in §2.3, and employed in the construction of the graph in §3.3.3.

In the canonical ensemble, we obtain the partition function of the catchment basin associated with minimum i from the Laplace transform of the microcanonical density of states, given by equation (5.15),

$$\begin{aligned} Z_i(T) &= \int_{E_i}^{\infty} \Omega\left(E'\right) \exp\left(-E'/k_{\mathrm{B}}T\right) dE', && (5.23) \\ &= \frac{\exp\left(-\beta E_i\right)}{\left(\beta h \bar{\nu}_i\right)^{\kappa}}, && (5.24) \end{aligned}$$

where $\beta = 1/k_{\mathrm{B}}T$, and the other quantities are defined as before. The canonical rate constants are then obtained by Boltzmann weighting their microcanonical counterparts, and substituting equation (5.22):

$$\begin{aligned} k_i^{\dagger}(T) &= \int_{E^{\dagger}}^{\infty} k_i^{\dagger}\left(E'\right) \frac{\Omega_i\left(E'\right) \exp\left(-E'/k_{\mathrm{B}}T\right)}{Z_i\left(T\right)} dE' && (5.25) \\ &= \frac{k_{\mathrm{B}}T}{h} \frac{Z^{\dagger}(T)}{Z_i(T)} && (5.26) \\ &= \frac{\left(\bar{\nu}_i\right)^{\kappa}}{\left(\bar{\nu}^{\dagger}\right)^{\kappa-1}} \exp\left[-\beta\left(E^{\dagger} - E_i\right)\right], && (5.27) \end{aligned}$$

where $k_i^{\dagger}(T)$ is the canonical rate constant out of minimum i via transition state † at temperature T. The equilibrium occupation probabilities for the canonical ensemble, $P_i^{eq}(T)$ are given, within the harmonic superposition approximation, by

$$P_i^{eq}\left(T\right) = \frac{Z_i\left(T\right)}{\sum_i Z_i\left(T\right)}. \qquad (5.28)$$

It can easily be shown that for both the canonical and microcanonical expressions outlined here, that the detailed balance requirement is satisfied.

5.1.3 IMPLEMENTATION OF KMC 'ON-THE-FLY'

KMC is generally used to simulate spatially ordered systems. The majority of studies in the literature model diffusion, adsorption or aggregation on surfaces, a selection of which are included in Refs 251–254. The order inherent in such systems means that the barriers to the processes of interest can be obtained or guessed before the KMC trajectory is generated. The listing of the transition probabilities at each step in Figure 5.1 therefore only requires calculation of which transitions are possible from the current configuration—i.e. in surface diffusion, which jumps are possible given the occupancy of the adsorption sites.

However, in the current situation, in which we wish to study diffusion in a supercooled liquid or a glass, we have to calculate the transition states at each minimum that we visit: 'on-the-fly'. Two recent examples of such a technique, which has not been attempted frequently, are those of Henkelman and Jónsson[255] and Hernandez-Rojas and Wales,[217] studying growth of the Al (100) surface, and the 80:20 binary Lennard-Jones mixture, respectively. Snurr et al. previously used a similar technique to study diffusion of benzene in silicalite.[256]

The study of the BLJ system[217]—which is, of course, the most relevant to the current work—used a 60-atom supercell, with twenty transition state searches at each minimum. Random configurations were used to initiate each run, and 10^4 KMC steps were taken. The mean energies of minima, structure factors and the number of minima visited in a given number of steps were analysed, but no dynamic properties were obtained. The results were found to be broadly consistent with MD: of particular interest was the observation that the number of minima visited in the the last 5000 steps of the trajectory decreased sharply at around $k_{\mathrm{B}}T \sim 0.45\epsilon_{\mathrm{AA}}$, very close to the critical temperature of mode coupling theory.

A 60-atom system is perhaps a little small, and so there may be some unwanted finite-size effects. However, it is probably close to the largest system that can be studied by KMC at the current time. It is reasonable to expect that a representative sample of transition states will number at least $\mathcal{O}(N)$ for each minimum. This relationship was derived by Doye and Wales by dividing a system of mN atoms into m N atom subsystems.[137] If the PES of each subsystem has $n_{\mathrm{m}in}(N)$ minima, then as long as the sub-systems are independent, then:

$$n_{\mathrm{m}in}(mN) = n_{\mathrm{m}in}(N)^{m}. \tag{5.29}$$

The solution to this equation is the $n_{\mathrm{m}in} = \exp(\alpha N)$. If the rearrangements associated with a transition state can then be located to a single subsystem, the entire mN-atom system will be at a transition state one of the m subsystems is at a transition state, and all the others are at minima. Therefore,

$$n_{\mathrm{t}s}(N) = mn_{\mathrm{min}}(N)^{m-1}\, n_{\mathrm{t}s}(N). \tag{5.30}$$

The solution of this equation is $n_{\mathrm{ts}}(N) = N\exp(\alpha N)$. Thus $n_{\mathrm{ts}}/n_{\mathrm{min}}$ is expected to be linear. For clusters with more than around six atoms, this linear relationship was found to hold reasonably well.[137]

In the last chapter, we found that our techniques are very efficient at locating rearrangements with low barriers: but diffusion appears to take place via high barrier processes. If we do not obtain enough transition states at each minimum visited in the KMC trajectory, nondiffusive rearrangements with low barriers will be selected too often.

5.1.4 IMPROVING EFFICIENCY AND SIMPLIFYING KMC

It is possible to group minima, where minima within a group are treated as being in equilibrium with each other.[122, 173, 256, 257] At first glance, this is appealing in the current situation, as we identified in the previous chapter a very large number of processes with barrier heights much less than $k_\mathrm{B}T$. Thus, our KMC run need only consider jumps between groups of minima—rather than oscillation between a few minima via nondiffusive processes.

It can be easily shown,[173] that the master equation yields an effective rate constant between a pair of groups of minima, denoted A and B:

$$k_{AB}^{\mathrm{eff}} = \frac{\sum_{i\in A}\sum_{j\in B} k_{ij} P_j(t)}{\mathcal{P}_B(t)}, \tag{5.31}$$

where $\mathcal{P}_B(t)$ is the total occupation probability for group B, $\sum_{j\in B} P_j(t)$. The approximation made is that if intra-group motion is much quicker than inter-group motion, then $P_j(t)/\mathcal{P}_B(t) \sim P_j^{\mathrm{eq}}/\mathcal{P}_B^{\mathrm{eq}}$.

The problem with this approach is that in the current situation we have no real way of selecting an appropriate threshold rate constant to determine which minima are in equilibrium, and which are not. In the previous chapter, we obtained continuous distributions of barriers, in which the barriers to both diffusive and nondiffusive rearrangements overlapped. In the Appendix to this chapter, we derive the different timesteps for the grouping method, and the expectation value of the residence time in the group without using this method. In the simplest case, for a group of two minima, the difference is negligible only if the intra-group and inter-group rate constants are orders of magnitude different. In any case, the rate determining step is finding the transition states connected to each minimum, whether we use the grouping algorithm or not. In order for the grouping to work, we still need to search each minimum, and so this grouping algorithm will not speed up the calculation significantly.

An alternative way to make KMC more efficient is to simply neglect low barrier processes. This might seem a strange thing to do, as low barrier processes will be those that are selected most often. However, as we showed in the last chapter, it seems unlikely that these processes will contribute directly to diffusion. The rationale for this technique rests on the assumption that if a pair of minima are linked by a low barrier, then the sets of transition states to which each minimum is connected are likely to be very similar. Thus the low barrier process can be neglected. For the pair of minima considered in the Appendix, it is sufficient that the inter-group rate constants are equal, $k_{\uparrow 1} = k_{\uparrow 2}$ for the timesteps with and without grouping to be both equal to $k_{\uparrow 1}$. On this basis, ignoring the waiting time seems viable, as it could potentially reduce the number of transition state searches necessary. However, the key assumption that minima linked by low barriers are linked by similar transition states is not necessarily valid in a disordered system. We suggested in the last chapter that nondiffusive rearrangements may redistribute free volume: this may well have some effect on the available rearrangements. Therefore, at least in the first instance, we must include the nondiffusive rearrangements.

5.1.5 IMPROVEMENTS IN PES SEARCHING ALGORITHMS

KMC calculations are more demanding of our PES searching algorithms than the simple collection of minima and transition states discussed in the preceding chapter. The results will only accurately reflect the true properties of the system if the searching algorithm finds enough transition states connected to each minimum, which are representative of the complete distribution. It is vital that we find transition states connected to minima on our KMC trajectory as efficiently as possible, while those not connected to it are entirely irrelevant. This situation differs from the characterisation of the PES in standard master equation dynamics[153](§5.1), where instead we want to build up a database of minima that are sufficiently interconnected to form a representative sample of the global PES. It was important that we optimised the parameters and searching methods used for our KMC run, to ensure high quality results, using the minimum of computer time. We therefore used a test set of ten randomly selected minima from MD trajectories to evaluate the relative performance of different searching parameters and techniques. To test parameters other than the number of searches per minimum, we used 50 searches, and then evaluated each parameter set using the criteria of computer time, number of connected transition states found, and the waiting time. Obviously, it is desirable for the waiting time, $\langle\tau\rangle = (\sum k_{ji})^{-1}$, to be as small as possible, as the value we obtain from our incomplete set of minima can only be an upper bound on the true value, given the assumptions we have made in its derivation.

In the previous chapter, we carried out between 40 and 400 hybrid EF/BFGS transition state searches from each minimum. One of the principle disadvantages of using hybrid methods over pure eigenvector-following is that a large number of transition state searches from the same minimum tend to converge to a small number of transition states, wasting a considerable amount of computer time. In §2.1.4 and Ref 158 we outlined in detail a technique based on hard-sphere moves for producing starting configurations for hybrid transition state searches. The system is given a random $3N$-dimensional velocity vector, and a standard hard-sphere MD trajectory is propagated until the first collision between a pair of atoms. A starting point for the hybrid transition state search is then selected from a point on this trajectory. For the 10-minimum test set, we found that there was no significant variation in the number of transition states found per minimum, or the waiting time. We therefore used the default value of $t_{12} = 1$.

An additional way of finding transition states is to use the nudged elastic band algorithm (§2.1.2), which starts a pair of unconnected minima and interpolates between them. n_{neb} equally spaced atomic configurations are created between the pair of minima. These are then visualised as points on an elastic band, and the force each image is defined by the potential surface and the spring constant of the elastic band. The images are then moved according to this force, for a set number of LBFGS steps (n_{nsteps}), or until the RMS force on the band reaches a set threshold. In practice, the number of images, n_{neb}, and the number of LBFGS steps are the most important parameters, since it is computationally cheaper to take only a few optimisation steps for the NEB, and then use the highest-energy image as a starting point for a standard one-ended transition state search. The greater the value of n_{neb}, the closer the highest energy image should be to a saddle point, but the greater the computational expense of the minimisation of the RMS force on the NEB. We are only interested in transition states connected to our current minimum, and so the CONNECT algorithm is set to finish when a connected transition state is found, rather than when a complete path is found. As well as the parameters for the NEB routine, we can set the maximum number of transition states that the CONNECT algorithm (§2.1.2) will find before giving up if none of them are connected to the current minimum. We experimented with values of n_{neb} of 3 & 7, n_{steps} of 40 & 80, and values of $n_{ts}^{\max} = 5$, 10, 20 & 30.

The most important parameter appears to be $n_{ts}^{\max}$ allowed in the CONNECT algorithm. The average numbers of transition states found were $16.4, 17.75$ and 19.1 for $n_{ts}^{\max} = 5$, 10 and 20, respectively. Above 20 steps, the law of diminishing returns applies, and there is no significant advantage in using $n_{ts}^{\max} = 30$. The next most important parameter is the number of images: $n_{neb} = 7$ was consistently better than $n_{neb} = 3$. The difference in the number of transition states found was only $\sim 1\,\%$ for $n_{ts}^{\max} = 5$, but increased to $\sim 15\%$ for $n_{ts}^{\max} = 20$. For all parameter sets, there was no significant difference between using $n_{steps} = 40$ and $n_{steps} = 80$.

Another issue is how we select the starting minima for the double-ended transition state search. Obvious options are (1) using minima we have already found that are not connected to the current minimum, (2) generating new minima by perturbing the entire system and minimising, (3) perturbing a small number of atoms and minimising, or (4) swapping a pair of atoms and if necessary, minimising.* We decided not to use option (1), as this has the potential to bias any pathways found towards minima already in the database. For options (2) and (3), the magnitude of the perturbation is crucial: if it is too small, the system will fail to leave the basin of attraction of the current minimum, and if it is too large the minima that we are trying to connect will be separated by too great a distance. It is also to be expected that the most efficient perturbation size will vary across the PES. Therefore, we varied the magnitude of the perturbation of the coordinates by increasing the magnitude by 5% each time the system failed to leave the current basin of attraction, and decreasing it by the same amount each time the perturbation was successful. Option (4) found, at most, an average of twelve transition states per minimum, with the optimum NEB parameter set. With the same NEB parameter set, options (2) and (3) had similar success rates, both finding an average of 16-17 transition states per minimum, with very similar waiting times. We therefore used option (2) to generate new minima in the actual KMC runs.

We used both the nudged elastic band algorithm and the hard-sphere method for the KMC runs: performing 16 NEB searches and a further 84 hard sphere searches at each minimum. The methods have slightly different biases, and so the most representative set of transition states is found with a combination of both strategies.

---

*Minimisation is only required if we swap the positions of atoms of different types.

We carried out MD and KMC runs for the 60-atom binary Lennard-Jones system at number densities of 1.1, 1.2 and $1.3\,\sigma_{\mathrm{AA}}{}^{-3}$. We adjusted the energies at which the runs were performed so that the diffusion constants measured were in the range $-11 < \ln D < -3$, where D is expressed in units of $\sigma_{\mathrm{AA}}\epsilon_{\mathrm{AA}}{}^{1/2}m^{-1/2}$. This range extends from the moderately supercooled region to close to the minimum diffusion constant that can be measured accurately on the timescale of computer simulations. We used the MD runs both for comparison with the KMC results, and as a means of efficiently generating representative starting configurations for the KMC runs. The MD simulation consisted of three independent microcanonical cooling runs, which each included up to 27 consecutive runs, where the total energy was held constant for 10^5 equilibration steps, followed by 10^6 steps in which we gathered the diffusion data. The final configuration was the starting configuration for the following run, with the total energy decreased by $10\,\epsilon_{\mathrm{AA}}$ ($0.17\,\epsilon_{\mathrm{AA}}$ per atom). A velocity verlet algorithm was used with a time step of $0.005\,(m\sigma_{\mathrm{AA}}{}^2/\epsilon_{\mathrm{AA}})^{1/2}$,[159] giving a cooling rate of $3.0 \times 10^{-5}\,(\epsilon_{\mathrm{AA}}{}^3/m\sigma_{\mathrm{AA}}{}^2)^{1/2}$/atom.

The final configurations from the runs at the appropriate energy were used as the starting configurations for the KMC runs. Fewer KMC runs were carried out, since they were considerably more computationally expensive, at energies varying by $0.33\,\epsilon_{\mathrm{AA}}$. Table 5.1 summarised the energies at which the results were harvested.

	Starting energy (MD)	Finishing energy (MD)	Highest energy (KMC)	Lowest energy (KMC)
$\rho = 1.1$	0.00	−4.83	−1.50	−3.50
$\rho = 1.2$	1.17	−3.17	−1.17	−3.17
$\rho = 1.3$	3.00	−3.00	0.00	−1.17

Table 5.1: Starting and finishing energies for the MD cooling runs and starting and finishing energies for the KMC runs, all expressed in ϵ_{AA} per atom. The energies in the MD cooling runs were changed in decrements of $0.17\,\epsilon_{AA}$, and the KMC runs were carried out at intervals of $0.33\,\epsilon_{AA}$.

The diffusion constant, D, was obtained using Einstein's relation:

$$D = \frac{\langle R(t)^2 \rangle}{6Nt}, \tag{5.32}$$

where $R(t)$ is the total displacement of the system at time t from its position at $t = 0$, and N the number of atoms. Alternatively, $D = (d(R(t)^2)/dt)/6N$, and so can be obtained from a plot of $R(t)^2$ against t.

For both MD and KMC, the diffusion constant at each temperature is obtained from calculating the gradient of a plot of $R(t)^2$ vs t, using linear regression. For the KMC results, the data points for the first 2000 steps are discarded: points obtained in this section of the trajectory are likely to contain large fluctuations away from the mean, especially at low temperatures.

Obviously, the displacement $R(t)$ obtained from KMC will be the distance from the starting minimum to the current minimum: while that obtained from MD will also contain a vibrational contribution. In the long time limit, this difference becomes negligible.

5.2 RESULTS

The principal quantities of interest in comparing KMC and MD trajectories are the diffusion constants, which we can use to assess fragility, and distribution of the energies of the minima sampled during the trajectory, which we can use to verify that the two simulation methods are sampling the same regions of phase space.

5.2.1 DIFFUSION CONSTANTS

Figures 5.2-5.4 are Arrhenius plots—$\ln D$ vs $\epsilon_{\mathrm{AA}}/k_{\mathrm{B}}T$—comparing diffusion constants obtained from KMC and MD. Table 5.2 contains the relative performance of several standard fitting functions to the MD data for $\rho = 1.1$ and $1.2\,\sigma_{\mathrm{AA}}{}^{-3}$.

Several trends emerge as the density increases in the MD data. First of all, the linearity of the relationship between $\ln D$ and T^{-1} increases with ρ. The 'strength parameter', D/T_0, is in the range $8-9$ for $\rho = 1.1\,\sigma_{\mathrm{AA}}{}^{-3}$ and $18-28$ for $\rho = 1.2\,\sigma_{\mathrm{AA}}{}^{-3}$. Thus with decreasing density, it appears that this system becomes *less fragile* with increasing density. These results appear to contradict Sastry's findings for a 256-atom system,[69] which suggested that the fragility increased with increasing density. Closer

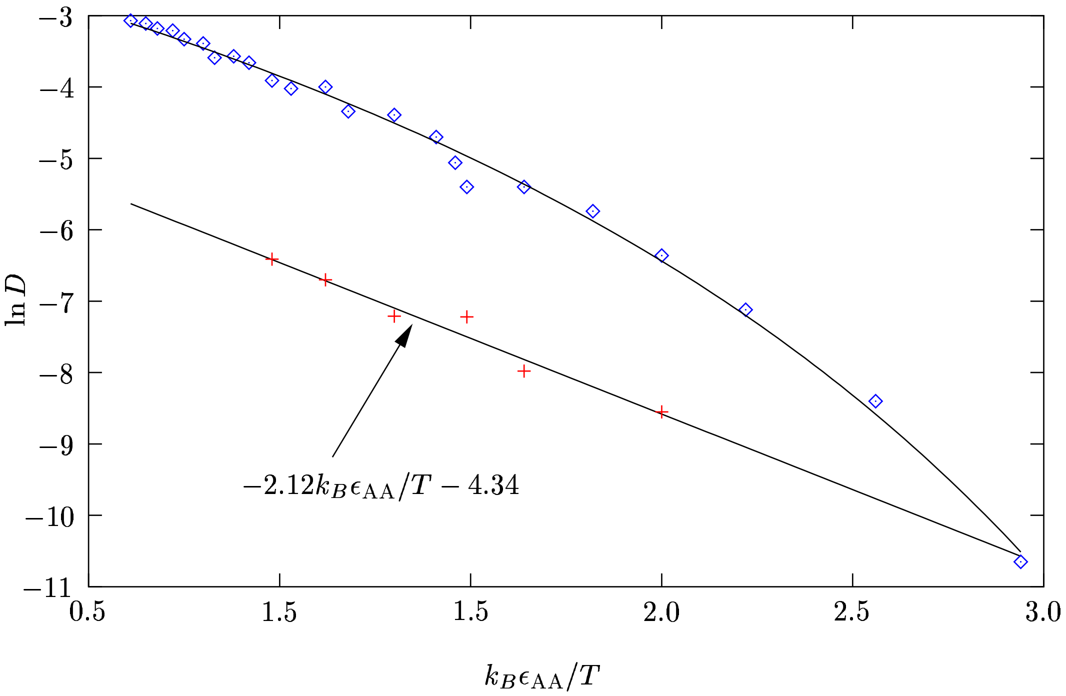

Figure 5.2: Arrhenius plots of diffusion constants obtained from KMC (red crosses) and MD (blue diamonds), at density 1.1. Included is the linear regression for the KMC diffusion constants, showing that these appear to have Arrhenius behaviour.

examination reveals that our parameters from VTF fits are broadly similar at number density $1.1\,\sigma_{\mathrm{AA}}{}^{-3}$: Sastry obtained $k_{\mathrm{B}}T_0/\epsilon_{\mathrm{AA}} = 0.156$ and $A \sim 1.2\,\epsilon_{\mathrm{AA}}$; we find $k_{\mathrm{B}}T_0/\epsilon_{\mathrm{AA}} = 0.172$ and $A = 1.41\,\epsilon_{\mathrm{AA}}$. It appears that the smaller system system suffers from significant finite size effects, especially at higher densities. However, as long as we take these into account when considering our results, they should not prevent us from drawing some preliminary conclusions about the nature of strong and fragile liquid potential energy landscapes.

The KMC data is linear at all densities, with a similar activation energy, E_a to the limiting activation energy of the MD data at the high-temperature end of the range studied here. The discrepancy increases with decreasing density: the diffusion constant from KMC is smaller by factors of ~ 20 for $\rho = 1.1\,\sigma_{\mathrm{AA}}{}^{-3}$, ~ 10 for $\rho = 1.2\,\sigma_{\mathrm{AA}}{}^{-3}$ and ~ 3 for $\rho = 1.3\,\sigma_{\mathrm{AA}}{}^{-3}$ at the top end of the temperature range studied here.

The data obtained from KMC can also be fitted to the asymptotic MCT relationship

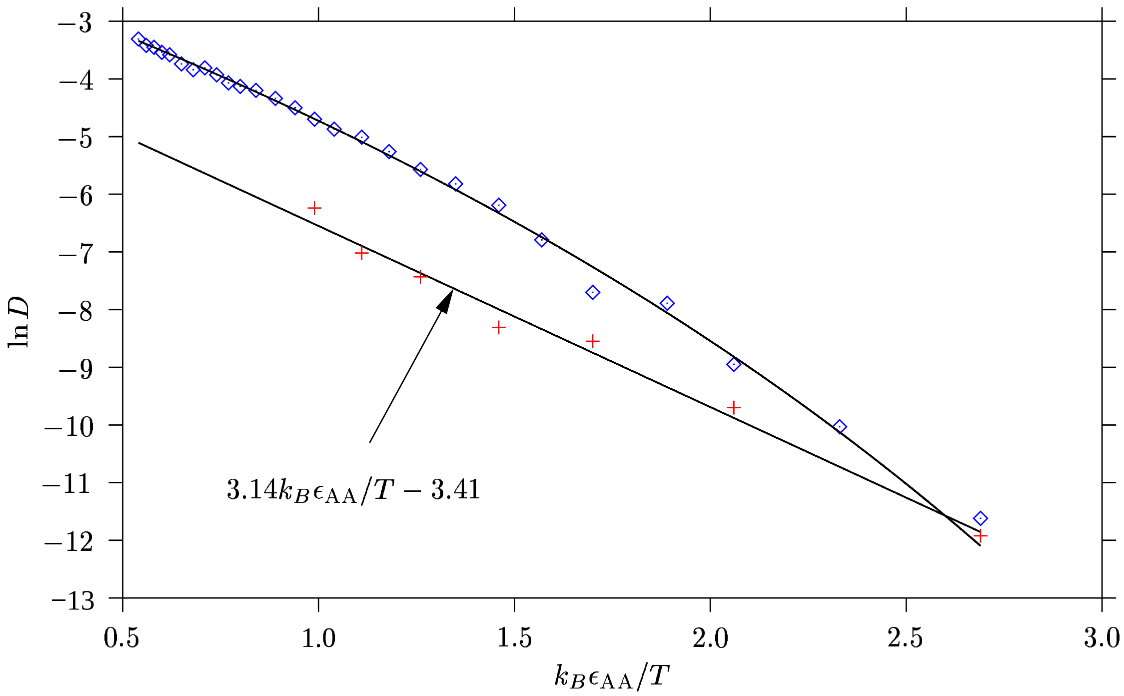

Figure 5.3: Arrhenius plots of diffusion constants obtained from KMC (red crosses) and MD (blue diamonds) at number density $1.2\,\epsilon_{\mathrm{AA}}\sigma_{\mathrm{AA}}{}^{-3}$. Included is the linear regression for the KMC diffusion constants: showing that these appear to have Arrhenius behaviour.

$D \sim (T - T_c)^{\gamma}$. From simulations employing more atoms and larger supercells,[95,96,98] it is accepted that $T_c \sim 0.435$ for $\rho = 1.2\,\sigma_{\mathrm{AA}}{}^{-3}$, the number density at which most research is performed. It is perhaps surprising that in the 60-atom system studied here, a measurable diffusion constant is obtainable below $k_{\mathrm{B}}T/\epsilon_{\mathrm{AA}} \sim 0.4$, which has previously been found to be the mode-coupling critical temperature.[94,95] In part this must be due to the Stoddard-Ford quadratic function and the cutoff of $1.842\,\sigma_{\alpha\beta}$, which decreases the well depth by 28% (§2.4.1).

We can quantify the degree to which the behaviour of the system is different from that observed in larger scale MD simulations.[94–96,98,163] In Table 5.2 we present the results from least-squares fitting using three different functions of $\ln D$ to $1/T$ for $\rho = 1.1\,\sigma_{\mathrm{AA}}{}^{-3}$ and $\rho = 1.2\,\sigma_{\mathrm{AA}}{}^{-3}$. The obvious functions to use are the asymptotic MCT relationship, $D \sim (T - T_c)^{\gamma}$, and the VTF and Arrhenius relationships. The MD data point at the lowest temperature, $k_{\mathrm{B}}T = 0.37\epsilon_{\mathrm{AA}}$, has the greatest uncertainty and so

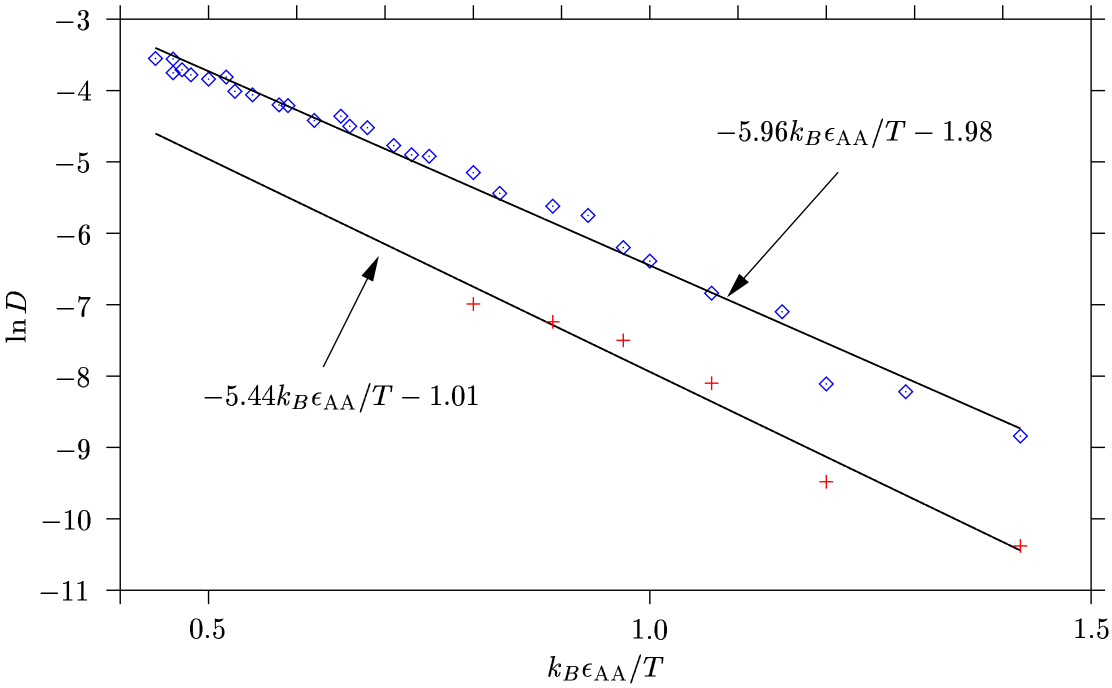

Figure 5.4: Arrhenius plots of diffusion constants obtained from KMC (red crosses) and MD (blue diamonds), at density 1.3. Both the KMC and MD results have been fitted using linear regression, as it appears that at this density the Arrhenius law is the most appropriate empirical fitting function.

we have included fits both with and without that point.

All the fitting parameters in presented in Table 5.2 suggest that the system studied here is different from one that uses a large supercell.[94–96, 98, 163] At $\rho = 1.2\,\sigma_{\mathrm{AA}}{}^{-3}$, the mode-coupling critical temperature is lowered to between 0.32 and $0.37\,\epsilon_{\mathrm{AA}}/k_{\mathrm{B}}$. This decrease is not altogether surprising, as it is of a similar order to the decrease in well depth compared to the standard Lennard-Jones potential. The value of γ is consistent with that obtained previously.[95] Of the three fitting functions, the VTF equation has the smallest estimated variance, and is therefore the best fit. T_0 is considerably lower than observed previously,[95] whether the lowest temperature result is included or not. It is also worth noting that the estimated variance, V_{est}, is of a similar order for all three fitting functions, for number densities of 1.1 and $1.2\,\epsilon_{\mathrm{AA}}\sigma_{\mathrm{AA}}{}^{-3}$.

For the densities that exhibit super-Arrhenius behaviour, the coincidence of the

Parameter	Number density $1.2\,\sigma_{AA}^{-3}$		Number density $1.1\,\sigma_{AA}^{-3}$
	Fits without $k_BT/\epsilon_{AA} = 0.37$	Fit including $k_BT/\epsilon_{AA} = 0.37$	
k_BT_c/ϵ_{AA}	0.378 ± 0.012	0.327 ± 0.010	0.325 ± 0.003
γ	2.159 ± 0.124	2.520 ± 0.137	1.757 ± 0.062
V_{est}	0.045	0.072	0.032
A/ϵ_{AA}	2.428 ± 0.022	2.738 ± 0.177	1.408 ± 0.088
T_0	0.133 ± 0.021	0.097 ± 0.016	0.172 ± 0.010
V_{est}	0.018	0.021	0.020
E_a/ϵ_{AA}	3.810 ± 0.080	3.710 ± 0.091	2.903 ± 0.120
V_{est}	0.041	0.047	0.124

Table 5.2: Fits to the diffusion data obtained from MD, including and not including the point below $k_BT/\epsilon_{AA} = 0.435$, which is conventionally taken as the critical mode-coupling temperature T_c.[94–96] The first fit is to the asymptotic MCT behaviour: $D \sim (T - T_c)^{\gamma}$, the second to the VTF equation: $D \sim \exp[A/k_B(T_0 - T)]$, and the third to a simple Arrhenius law, $D \sim \exp(-E_a/k_BT)$. Included for each fit is V_{est} the estimated variances of the fits.

mode-coupling critical temperature T_c and the point at which the two diffusion constants appear to merge is remarkable. For $\rho = 1.1\,\sigma_{\text{AA}}$ the value of T_c obtained from the least-squares fit is $0.35\,\epsilon_{\text{AA}}/k_{\text{B}}$, and the two fit lines cross at $T = 0.350\,\epsilon_{\text{AA}}/k_{\text{B}}$. For $\rho = 1.2\,\sigma_{\text{AA}}$, these values are both around $0.38\,\epsilon_{\text{AA}}/k_{\text{B}}$.

Thus, it appears that the KMC and MD results agree at the critical temperature of MCT. This is not entirely unexpected, as it is an accepted principle of MCT that as T_c is approached, so-called 'hopping' processes become important, as the macroscopic, hydrodynamic diffusion modes become 'frozen out'. These 'hopping', or 'activated' processes are likely to be very well described by minimum-saddle-minimum transition state theory picture.

The activation energy in the KMC runs at density $1.2\,\sigma_{\text{AA}}{}^{-3}$, obtained from the Arrhenius plot (Figure 5.3) is $-3.14\,\epsilon_{\text{AA}}$. If diffusion were a single-step process, we would expect to see barriers of this magnitude in the distribution function of accepted barriers, Figure 5.5. Unlike the previous barrier distributions in Chapter 4, this distribution includes both uphill and downhill barriers, but only those accepted during the

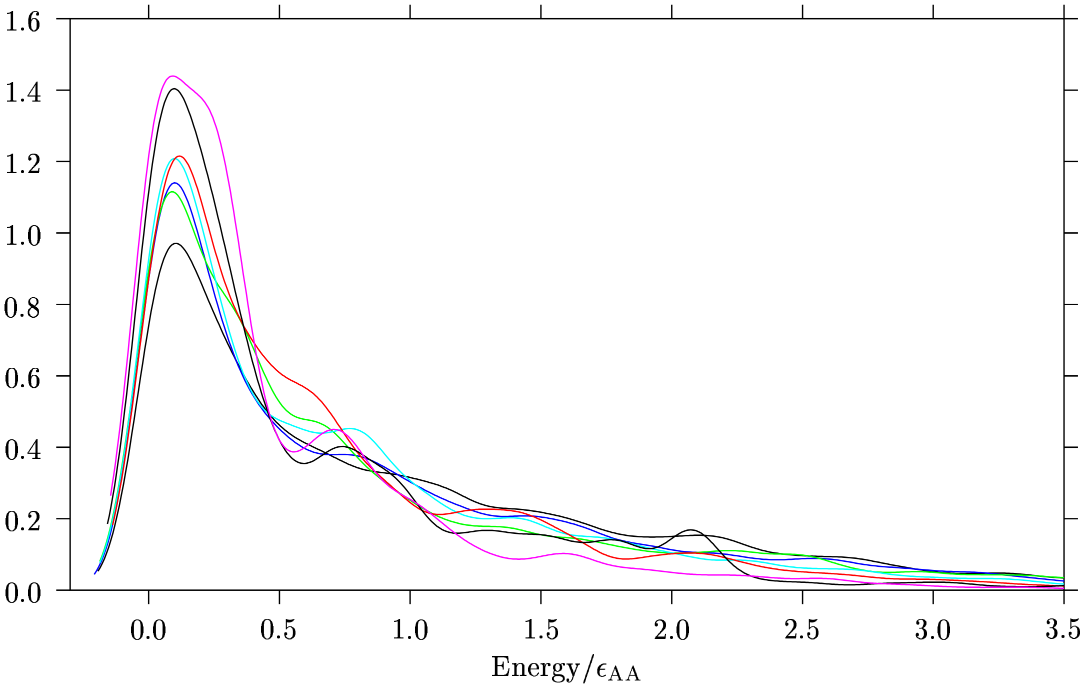

Figure 5.5: Barrier distributions of selected barriers for the KMC runs at density $1.2\,\sigma_{\mathrm{AA}}{}^{-3}$. The colours are as follows: -1.17 - black, broad low energy peak; -1.50 - blue; -1.83 - green; -2.17 - red; -2.50 - cyan; -2.83 - magenta; -3.17 - black, sharp peak at low energy.

KMC run. Nevertheless, the results are essentially the same as the downhill distributions obtained in Chapter 4, with the distributions spreading out slightly as the energy increases, as higher barrier moves are accepted more often. However, the negligible density at $E_{barrier} \sim E_a \sim 3.14\,\epsilon_{\mathrm{AA}}$ suggests that, as previously surmised, diffusion takes place by a multi-stage process, involving several transition states.

5.2.2 DISTRIBUTIONS OF ENERGIES OF MINIMA SAMPLED

We quenched the MD configurations every 10^3 steps, to generate a database of minima sampled by the cooling runs, for comparison with the distributions obtained in the KMC runs. These distributions, generated using the usual Gaussian method to produce smooth functions, are presented in Figures 5.6-5.8. In each Figure, the top panel represents the distribution functions obtained from MD, the bottom those from KMC. For clarity, only the results obtained from MD In each case, the shapes of the

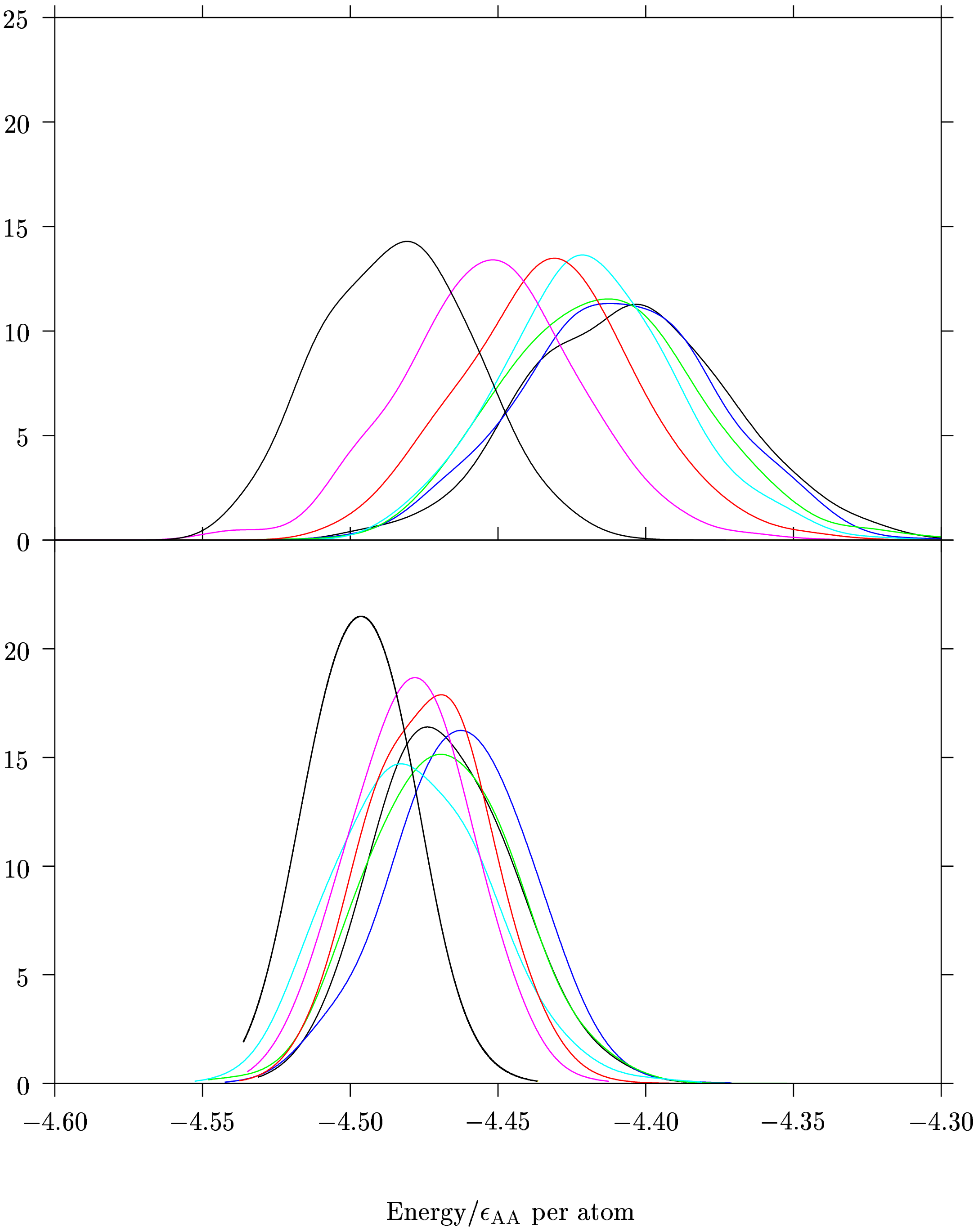

Figure 5.6: Energy distributions of minima visited by MD (top panel), and KMC (bottom panel), at number density $1.1\,\sigma_{\mathrm{AA}}{}^{-3}$. The smooth distribution functions were generated using the Gaussian smoothing technique described in §4.3.1, The Gaussian width $s = 0.01\,\epsilon_{\mathrm{AA}}$. The energies at which the microcanonical MD and KMC runs were carried out were −3.50 (black, low energy), −3.17 (magenta), −2.83 (red), −2.50 (light blue), −2.17 (green), −1.83 (dark blue), and −1.50 (black, high energy), all in ϵ_{AA} per atom.

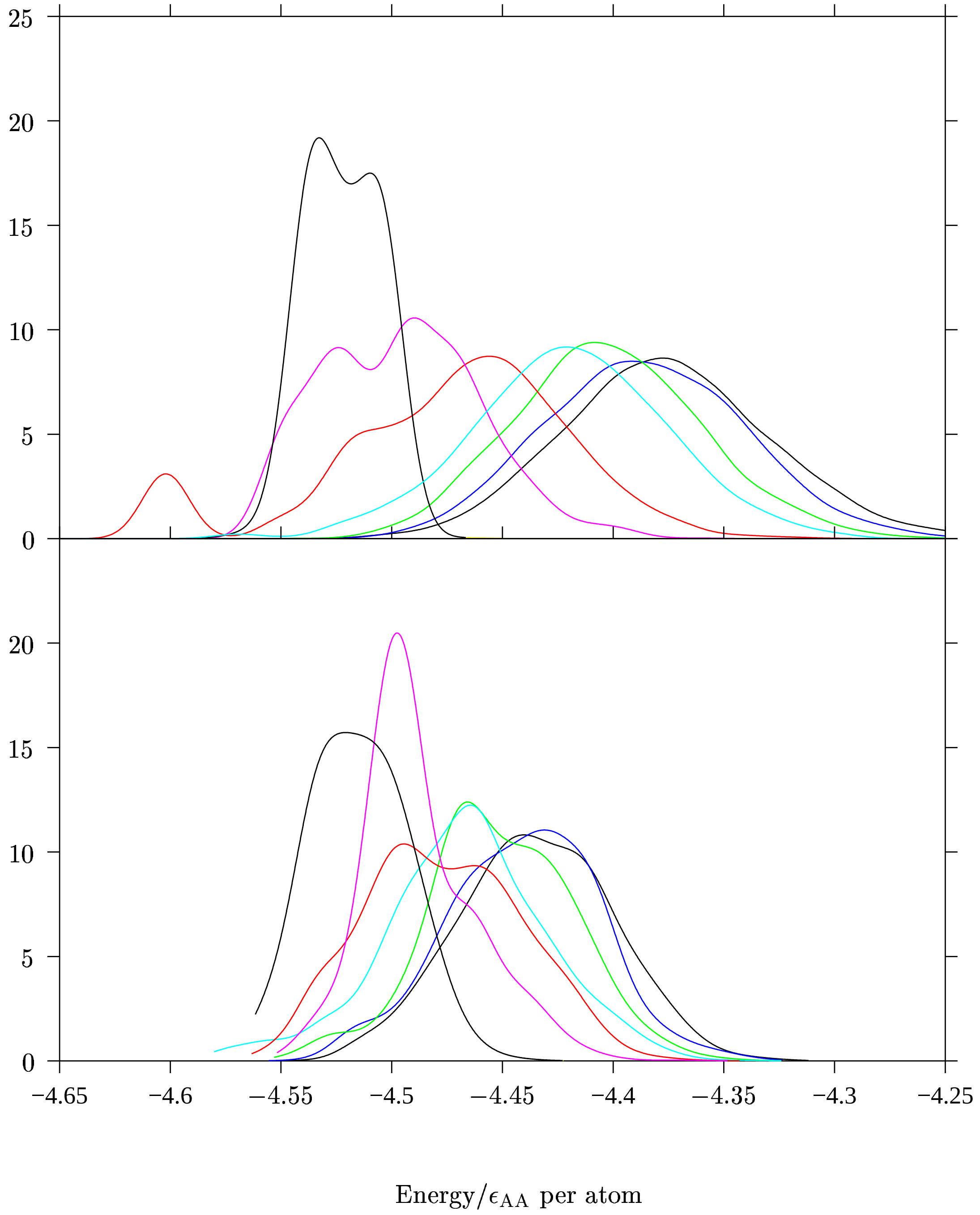

Figure 5.7: Energy distributions of minima visited by MD (top panel), and KMC (bottom panel), at number density $1.2\,\sigma_{\rm AA}{}^{-3}$. The Gaussian width $s = 0.01\,\epsilon_{\rm AA}$. The energies at which the microcanonical MD and KMC runs were carried out were −3.17 (black, low energy), −2.83 (magenta), −2.50 (red), −2.17 (light blue), −1.83 (green), −1.50 (dark blue), and −1.17 (black, high energy), all in $\epsilon_{\rm AA}$ per atom. The very low energy peak for the run at $-2.50\,\epsilon_{\rm AA}$ per atom corresponds to a set of predominantly crystalline minima samples during one of the runs.

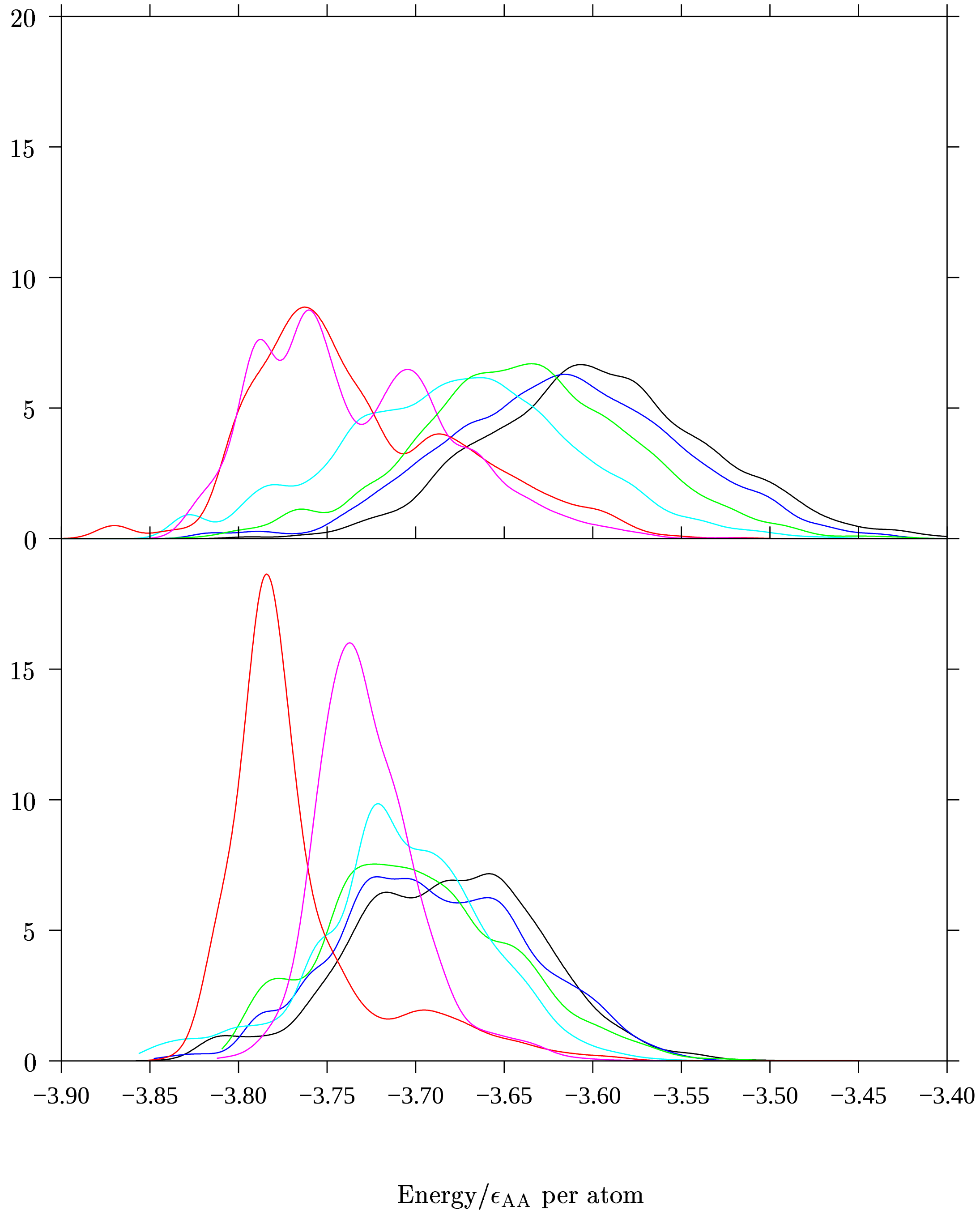

Figure 5.8: Energy distributions of minima visited by MD (top panel), and KMC (bottom panel), at number density $1.3\,\sigma_{\mathrm{AA}}{}^{-3}$. The Gaussian width $s = 0.01\,\epsilon_{\mathrm{AA}}$. The energies at which the microcanonical MD and KMC runs were carried out were 0.00 (black), −0.33 (dark blue), −0.67 (green), −1.00 (light blue), −1.33 (red), and −1.67 (magenta), all in ϵ_{AA} per atom.

$e_{tot}/\epsilon_{\mathrm{AA}}$	$\langle e_{\min}\rangle/\epsilon_{\mathrm{AA}}$ (MD)	$\langle e_{\min}\rangle/\epsilon_{\mathrm{AA}}$ (KMC)
-1.17	-4.37	-4.43
-1.50	-4.39	-4.44
-1.83	-4.40	-4.45
-2.17	-4.42	-4.47
-2.50	-4.47	-4.48
-2.83	-4.49	-4.49
-3.17	-4.52	-4.51

Table 5.3: Mean energies of minima sampled, $\langle e_{\min}\rangle$, obtained from MD and KMC at number density, $\rho = 1.2\,{\sigma_{\mathrm{AA}}}^{-3}$, at total energy e_{tot}.

distributions vary significantly. However, at low energies, the range of energies at which the distributions are non-zero are very similar. The distributions are most similar for the highest number density, and least similar for the lowest. This is consistent with the trend in the discrepancies in diffusion constant in the previous section.

There are two distributions, with obvious anomalous excess low-energy probability density: the one obtained from MD at $\rho = 1.2\,{\sigma_{\mathrm{AA}}}^{-3}$ and energy $-2.50\,\epsilon_{\mathrm{AA}}$ per atom; and that from KMC at $\rho = 1.3\,{\sigma_{\mathrm{AA}}}^{-3}$ and energy $-1.33\,\epsilon_{\mathrm{AA}}$ per atom (both in red). The source of the anomalies is the same: in both cases, the trajectories found a region of the PES with significant crystalline character, and became 'stuck'. This also explains the low diffusion constants in other cases. The ability of the BLJ 60-atom system to find substantially crystalline minima has been observed before.[182,217]

Table 5.3 tells the same story as Figure 5.7. The agreement in the mean energies is extremely good for the lowest three energies, but becomes progressively worse as the energy increases. It may be a concern that at higher energies, the microcanonical temperature is effectively significantly higher for KMC compared to the corresponding MD runs. We can obtain the harmonic microcanonical temperature from the density of states associated with a single minimum from the superposition approximation, as shown in §5.1.2. Even for the highest temperature we get $k_{\mathrm{B}}T_{\mu}/\epsilon_{\mathrm{AA}} = 1.12$, compared to the temperature in the corresponding MD run of $k_{\mathrm{B}}T/\epsilon_{\mathrm{AA}} = 1.07$. Thus, the discrepancy in the temperature is not significant, and we are justified in using the temperatures from MD in the previous Arrhenius plots for both the KMC and MD data. However, we cannot assume that the under-sampling of high energy regions of the PES will not affect our results.

5.3 Discussion and analysis

The discrepancies between KMC and MD in both the diffusion constants and energies of the minima sampled are somewhat disappointing. However, the results are still interesting, as the failure of the KMC to replicate MD may indicate the cause of the super-Arrhenius behaviour of the system.

First of all, we have to question the principal assumption of our implementation of the KMC algorithm in the present work. We have assumed that (1) populations of basins on the PES and transitions between them are well described using the harmonic superposition approximation (§5.1.2), (2) that dynamics between basins are Markovian and (3) that we have sampled phase space adequately. We can be reassured of the validity of the harmonic approximation by the results of Broderix et al.[131] Comparison of the waiting times in minima from our KMC runs and MD runs—which we quenched at every step—are in Table 5.4, indicating that the waiting times obtained by the harmonic approximation in the KMC simulations cannot be the sole cause of the discrepancies. The KMC waiting times are obviously related to the sampling of the PES as well as harmonic approximation, and the size of the discrepancies due to these two sources. However, for number density $1.3\,{\sigma_{\mathrm{AA}}}^{-3}$, where the discrepancy is temperature-independent, the ratio of waiting times is only weakly temperature dependent, and on average is 3.06 ± 1.18, which is very close to the discrepancy observed in the diffusion constant. Thus, in this case, where both MD and KMC results have Arrhenius temperature dependence, it turns out that the error in the pre-factor can be accounted for entirely by the error in the waiting time. This result probably has contributions from both sampling error and the harmonic approximation, but these appear to independent of energy. The other two number densities have a further contribution to the observed discrepancy.

Next, we consider the Markovian assumption. If the enhanced MD diffusion constant is the due to the failure of the Markovian assumption at high temperature, then there must be positive correlation between successive transitions between minima.

This question has been considered in depth by Keyes and Chowdhary (KC): who

ρ/σ_{AA}^{-3}	Min $\left[\langle t_w^{\mathrm{KMC}}\rangle / \langle t_w^{\mathrm{MD}}\rangle\right]$	Max $\left[\langle t_w^{\mathrm{KMC}}\rangle / \langle t_w^{\mathrm{MD}}\rangle\right]$
1.1	2.67	9.95
1.2	0.95	5.62
1.3	1.75	4.67

Table 5.4: Minimum and maximum values of the ratio of the arithmetic mean waiting time in MD and KMC for each of the number densities. As the total energy is raised, the ratio increases approximately linearly, reflecting the increased discrepancy between the KMC: but the harmonic approximation alone cannot explain our observations.

considered diffusion in a 32-atom Lennard-Jones system,[129] and Doliwa and Heuer (DH) who studied a 65-atom BLJ system.[234,235] Both groups found that any correlation present was entirely negative: KC found that removing the effect of correlation greatly enhanced the diffusion constant. DH coarse-grained the landscape into 'metabasins'— megabasins in our terminology— and found that there was weak back-correlation up to five inter-megabasin transitions.

We can measure the directional nature of successive transitions between basins, by examining the cosine between the transition vectors leading to the ith and jth basins in a sequence, which can be obtained easily from the scalar product of the inter-minimum vectors:

$$\cos(\theta_{ij}) = \frac{(\mathbf{R}_i - \mathbf{R}_{(i-1)}) \cdot (\mathbf{R}_j - \mathbf{R}_{(j-1)})}{\left|\mathbf{R}_i - \mathbf{R}_{(i-1)}\right| \left|\mathbf{R}_j - \mathbf{R}_{(j-1)})\right|} \tag{5.33}$$

where $\mathbf{R}_i$ represents the coordinates of the ith minimum. In Figure 5.9 we show the average value of this correlation function for the temperature ($k_{\mathrm{B}}T/\epsilon_{\mathrm{AA}} = 1$) and density ($1.1\,\sigma_{\mathrm{AA}}{}^{-3}$ at which we would expect the most positive correlation between successive inter-minimum transitions. Even the residue after subtracting pure back-correlations, i.e. those with $\cos(\theta_{ij}) = -1$, shows no significant positive correlation. Thus, on the basis of previous work,[129,234,235] and the directional correlation function we can conclude that the enhanced diffusion constant of MD over KMC is not due to non-Markovian behaviour.

Therefore, it appears that we have undersampled configuration space as comparison of the distribution of minima sampled by the two simulation methods suggests. The

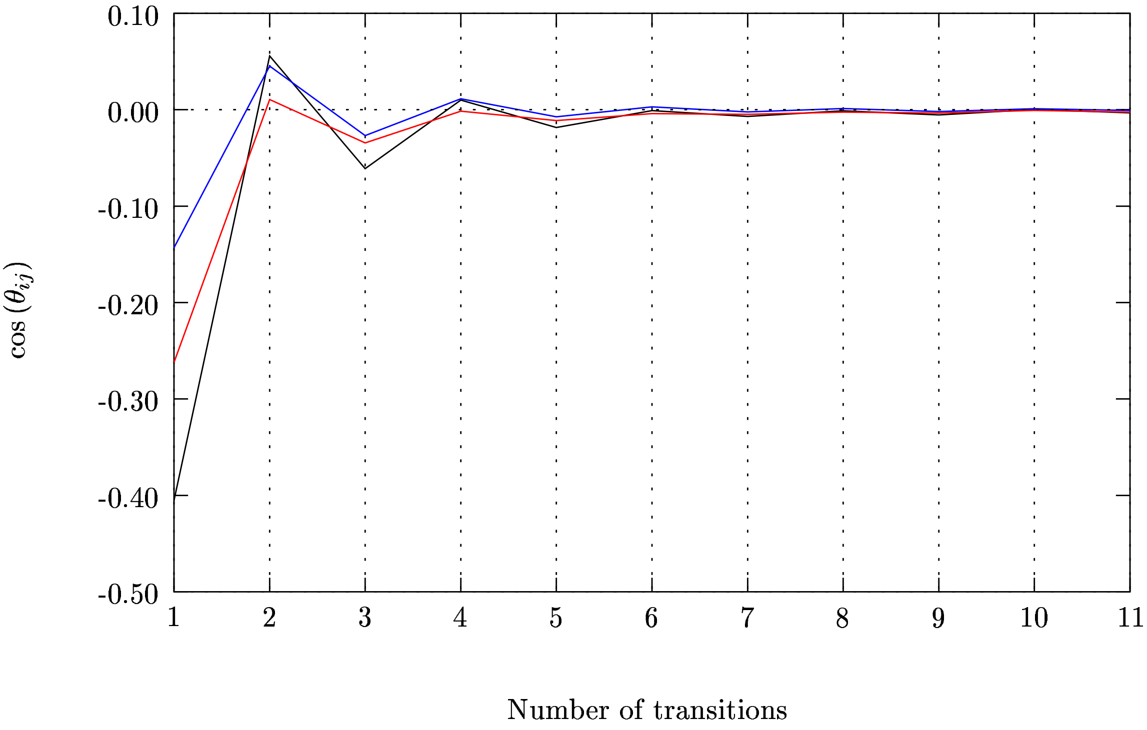

Figure 5.9: Mean values of the cosine of the angle between successive transition vectors between minima, for the MD run at energy $-1.50\,\epsilon_{\mathrm{AA}}$ and number density $1.1\,\sigma_{\mathrm{AA}}{}^{-3}$. This is the MD run that has the greatest enhancement of the diffusion constant over KMC. The three lines represent (1) all inter-minimum transitions (black), (2) pure back correlations—i.e. $\cos\theta_{ij} = \pm 1$ and (3) the difference between them. There is no positive correlation between sucessive transitions, showing that a non-Markovian explanation for the super-Arrhenius behaviour of the MD runs is not viable.

KMC approach has measured the rate of diffusion between minima at the bottom of the energy range sampled by MD. However, what is particularly interesting is that the activation energy as measured by KMC $\left(E_a^{\mathrm{KMC}}\right)$ is much smaller than the limiting activation energy measured by MD as $T \to T_c$ $\left(E_a^{\mathrm{MD}}\left(T_c\right)\right)$. If the super-Arrhenius behaviour observed at number densities $1.2\,\sigma_{\mathrm{AA}}{}^{-3}$ and $1.1\,\sigma_{\mathrm{AA}}{}^{-3}$ were due to large potential energy barriers separating megabasins in the low part of the PES, we would expect this limiting low temperature activation energy to be the same for both KMC and MD. In fact, E_a^{KMC} is much closer to A - the numerator within the exponential term in the VTF equation, which also corresponds to the approximate activation energy when $T \gg T_0$. This result throws up the rather surprising possibility that the potential barrier to diffusion at the bottom of the relevant energy is the same as at the top. As the KMC sampling of higher minima is so poor, we can assume that there is no significant change in prefactor for the KMC runs: the change in rate with changing temperature is entirely energetic, with no entropic contribution. This conclusion that the barriers do not change as the surface is descended contrasts sharply with the assumptions of the Adam-Gibbs (§1.2.1) approach, where the energetic barriers to diffusion grow with decreasing configurational entropy: again, if the Adam-Gibbs equation were directly applicable to this system, we would expect E_a^{KMC} to be close to $E_a^{\mathrm{MD}}(T_c)$. Therefore, the super-Arrhenius behaviour observed in MD must be entropic, and contained in the prefactor.

In Chapter 5, we noted that the normal mode frequencies were dependent on potential energy. However, this will be included in both KMC and MD, and so cannot be the cause of the discrepancies in the prefactor. Connectivity between megabasins remains as the most likely culprit for the failure of KMC to replicate MD. If we assume that this is the case, then it appears that higher-lying minima are, on average, connected to more minima by kinetically accessible barriers than lower-lying minima. Thus, sampling of higher energy minima is crucial to the calculation of the diffusion constant: unsurprisingly, the KMC algorithm has failed to cope with the Gaussian density of minima with energy.

The notion that the temperature dependence of the diffusion constant is controlled by entropy is far from original. However, the way we interpret this correlation between the dynamics of the system and the entropy is closer to the interpretation of Keyes' INM-REM analysis (§1.3.1).[113,114,118] In this theory, it is assumed that the diffusion constant is proportional to the time-averaged fraction of unstable normal modes corresponding to double well potentials, $\ln(f_{dw})$. This is then assumed that both $f_{dw}(E)$ is proportional to the number states of energy lower than E. In the macroscopic limit, therefore, $\ln(f_{dw}) \sim S_c$, where S_c is the configurational entropy. Thus, the relationship $D \sim \exp(S_c)$ must hold, which is reminiscent of Dzugutov's universal scaling law.[67,71,76] While the INM-REM arguments appear somewhat simplistic, they do fit simulation data surprisingly well.[119]

We combine here the INM-REM, Dzugutov and Stillinger-Weber approaches in explaining our results. It appears that in this system the potential energy barriers are essentially constant in the region of the PES explored by the supercooled liquid. We do not believe that there are no regions with larger barriers that form kinetic traps, rather that these are not sampled significantly when the system is a metastable supercooled liquid: their contribution to the partition function is only significant at time scales longer than is accessible to computer simulation. Our results suggest that the super-Arrhenius behaviour we have observed is due to decreased connectivity in the lower energy regions of the PES. The relevant energy barriers to diffusion will tend to be the lowest: i.e. the minimum barrier to diffusion. It is reasonable to expect that the number of such minimum-barrier pathways from one megabasin to another will be proportional to the number of megabasins in the system with equal, or lower, potential energy. This connectivity contribution is therefore entropic, and is expected scale as $\exp(S)$, and so we achieve the relationship,

$$D \sim \exp\left(S_c - E_a/k_{\mathrm{B}}T\right). \tag{5.34}$$

Thus in the high-temperature limit, where $k_{\mathrm{B}}T \gg E_a$, the entropic term will dominate, and we recover the relationships similar to that of Dzugutov and Keyes et al. However, as the temperature decreases, we see departure from this law as the energetic term becomes significant too.[†] Our approach differs from the INM approach, in that like Stillinger and Weber, we visualise dynamics on the PES as consisting of transitions between minima via true transition states: we do not invoke higher order saddle points. The *accessible* connectivity of megabasins on the PES, via true transition states, increases as the PES is ascended. We introduce the term accessible connectivity, meaning the number of pathways to other megabasins with potential energy barriers close to the smallest possible for diffusion.

We admit that equation (5.34) will not be appropriate near the Kauzmann point. However, we would expect that the energy barrier to diffusion below the glass transition—i.e. diffusion during ageing—might exhibit a lower activation free energy than is observed immediately before reaching T_g in the cooling schedule. This behaviour would be expected, as below T_g the system would no longer be rapidly losing entropy on the experimental timescale. Such a discontinuity is observed in, for instance, tri-naphthyl

---

[†] Dzugutov's relationship uses excess entropy rather than configurational entropy. It has been argued that they are proportional to each other,[258] and in any case for the purposes of this general discussion, we can treat the two approaches as being qualitatively similar.

benzene (TNB).[259] In the Adam-Gibbs picture, super-Arrhenius behaviour is due to an inverse relationship between potential energy barriers and the configurational entropy, and so it would be most unexpected to see a *decrease* in activation free energy below the glass transition temperature.

Our picture of the connectivity is consistent with the relationship between D and f_{dw}. The probability of sampling a configuration close enough to a transition state for an diffusive imaginary mode will obviously be proportional to the accessible connectivity, multiplied by the Boltzmann factor of the minimum barrier pathway. Thus, D will be linearly related to the time average of f_{dw}. The low activation energy pathways below T_g are also rather reminiscent of Johari-Goldstein slow β processes. The pre-factor to these processes would correspond to the number of pathways 'frozen in' at T_g: again, the α processes have a much larger free activation energy approaching T_g owing to the rapidly decreasing entropy.

In Chapter 4 we observed that potential energy barriers of diffusive rearrangements become larger with increasing density. Thus, while the barriers may be the same in both high- and low-lying regions of the PES at constant volume, we expect that at constant pressure, as in experiment, that the barriers may be grow with decreasing temperature as the glass-former becomes more dense.

5.4 SUMMARY

We have used the failure of KMC to replicate MD to glean some novel information about the PES of this 60-atom binary Lennard-Jones system. Approaching T_g, there are still diffusive pathways accessible to the system with activation free energy close to the high temperature limiting value.

Therefore, in this atomic glass, the Adam-Gibbs picture of increasing potential energy barriers as the surface is descended does not apply. Instead we conclude, by a process of elimination and considering other models, that the connectivity between megabasins is proportional to the configurational entropy.

APPENDIX: GROUPING OF MINIMA

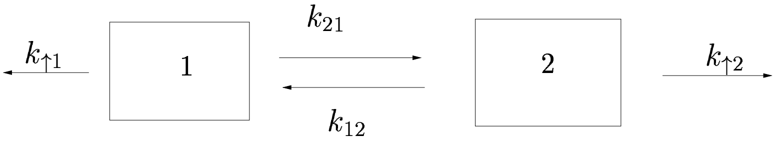

Figure 5.10:

Consider a pair of minima connected by fast rates k_{21} and k_{12}, where we use the conventional chemical notation, in which k_{ij} represents the rate *from* minimum j *to* minimum i. $k_{\uparrow i}$ represents the rate—or sum of rates—from minimum i to minima outside the group.

In conventional KMC, we consider the waiting time in each minimum. Here we consider the waiting time, τ, in the group of minima 1 and 2:

$$\begin{aligned} \tau &= \left(\frac{P_1}{P_1 + P_2} k_{\uparrow 1} + \frac{P_2}{P_1 + P_2} k_{\uparrow 2} \right)^{-1} \\ &= \frac{P_1 + P_2}{P_1 k_{\uparrow 1} + P_2 k_{\uparrow 2}}, \end{aligned} \tag{5.35}$$

where P_1 and P_2 are the occupation probabilities of minima 1 and 2, respectively. According to the detailed balance requirement, $P_1 k_{21} = P_2 k_{12}$, and so we can eliminate P_1 and P_2 to give:

$$\tau = \frac{k_{12} + k_{21}}{k_{\uparrow 1} k_{12} + k_{\uparrow 2} k_{21}}. \tag{5.36}$$

In the special case where $k_{\uparrow 1} = k_{\uparrow 2} = k_{\uparrow}$ and $k_{12} = k_{21}$, $\tau = (k_{\uparrow})^{-1}$.

We can now calculate the expectatation value of the waiting time, $\bar{\tau}$, in conventional KMC, in which we do not coarse grain by grouping minima 1 and 2 together. The transition probability from minimum j to minima i, $w_{ij} = k_{ij}/(k_{ij} + k_{\uparrow j})$. Thus, assuming we start from minimum 1,

$$\begin{aligned}
\bar{\tau} &= w_{\uparrow 1}\frac{1}{k_{21}+k_{\uparrow 1}} + w_{21}w_{\uparrow 2}\left(\frac{1}{k_{12}+k_{\uparrow 2}} + \frac{1}{k_{21}+k_{\uparrow 1}}\right) \\
&\quad + w_{12}w_{21}\left(\bar{\tau} + \frac{1}{k_{12}+k_{\uparrow 2}} + \frac{1}{k_{21}+k_{\uparrow 1}}\right) \qquad (5.37) \\
&= \frac{k_{\uparrow 2}+k_{12}+k_{21}}{k_{\uparrow 2}k_{21}+k_{\uparrow 1}k_{12}+k_{\uparrow 1}k_{\uparrow 2}}.
\end{aligned}$$

In the special case where the respective rate constants are equal, $\bar{\tau} = (k_{\uparrow})^{-1}$, as above. It is easy to see that this expression will be close to that of Equation 5.35 provided that intra-group rates are much quicker than inter-group rates.

To generalise this expression for a group of n minima, we consider a transition probability matrix $\mathbf{W}$, $w_{ij} = k_{ji}/(\sum_{l=1}^{n} k_{li} + k_{\uparrow i})$. As we are using an n - fold kinetic Monte Carlo scheme, $w_{ii} = 0$, and $\sum_{j=1}^{n} w_{ij} + w_{\uparrow i} = 1$. Given a vector of the expected population of each minimum in the group after m steps, $p_j(m)$, we obtain $p_j(m+1) = \sum_i p_j(m)w_{ji}$. The expectation value of the time increment for this step is then the scalar product of $\mathbf{P}(m)$ and a vector of the waiting times for each of the minima in the group, $\mathbf{T}$, where $T_i = (\sum_{l=1}^{n} k_{li} + k_{\uparrow i})^{-1}$. Thus, given an initial population vector $\mathbf{P}(0)$, the expectation value of the time spent in the group of minima is given by:

$$t_w = \mathbf{T}^T \left(\sum_{i=0}^{\infty} \mathbf{W}^i\right) \mathbf{P}(0). \qquad (5.38)$$

Intuition suggests that $\sum_{i=0}^{\infty} \mathbf{W}^i$ will converge to a finite value provided that neither the group of minima or any subset of it form a closed set. To prove this mathematically, we first diagonalize $\mathbf{W}$, so that $\mathbf{W} = \mathbf{U}\Lambda\mathbf{U}^{-1}$, where Λ is a diagonal matrix of the eigenvectors of $\mathbf{W}$, and $\mathbf{U}$ a matrix of its corresponding eigenvalues. $\mathbf{W}^n = \mathbf{U}\Lambda^{\mathbf{n}}\mathbf{U}^{-1}$, and so it follows that the geometric progression in Equation (5.38) will converge if the spectral radius, $\rho(\mathbf{W}) > 1$, where $\rho(\mathbf{W}) = \max\{|\lambda| : \lambda \ni \sigma(\mathbf{W})\}$ and $\sigma(\mathbf{W})$ is the set of all eigenvalues of $\mathbf{W}$.

$\rho(\mathbf{W})$ is a lower bound for all possible matrix norms of $\mathbf{W}$.[260] If we consider the maximum row sum matrix norm, $|||\mathbf{W}|||_{\infty}$, defined by:

$$\|\mathbf{W}\|_\infty = \max_{1\leq i\leq n}\sum_{j=1}^{n}|W_{ij}|. \tag{5.39}$$

$\|\mathbf{W}\|_\infty \leq 1$, as the elements of row i represent the transition probabilities from minimum i to the other members of the group, and so cannot total more than 1. It therefore follows that $\rho(\mathbf{W}) \leq 1$.

The matrix $\mathbf{W}$ is necessarily nonnegative: $W_{ij} \geq 0\ \forall\ i, j$. It is a universal property of nonnegative matrices that there exists a vector $\mathbf{x}$, with $x_i \geq 0$ and $\mathbf{x} \neq 0$, which satisfies the equation $\mathbf{Wx} = \rho(\mathbf{W})\mathbf{x}$. Therefore, $\rho(\mathbf{W})$ is a real, positive eigenvalue of $(\mathbf{W})$.[260]

Finally, we consider the determinant of the matrix $(\mathbf{W} - \mathbf{I})$, which will be zero if $\rho(\mathbf{W}) = 1$:

$$\begin{vmatrix} -1 & w_{21} & w_{31} & \cdots \\ w_{12} & -1 & w_{32} & \\ w_{13} & w_{23} & -1 & \\ \vdots & & & \ddots \end{vmatrix} = 0 \tag{5.40}$$

The determinant will be non-zero provided that no rows or columns are linearly dependent. We can check by using elementary row and column operations in the following way:

1. Add all the columns to the right of the first column to it, giving the following matrix, with the same determinant

$$\begin{vmatrix} \sum_{j=2}^{n} w_{j1} - 1 & w_{21} & w_{31} & \cdots \\ \sum_{j=2}^{n} w_{j2} - 1 & -1 & w_{32} & \\ \sum_{j=2}^{n} w_{j3} - 1 & w_{23} & -1 & \\ \vdots & & & \ddots \end{vmatrix}$$

.

2. If there are no nonzero entries in the first column, the determinant is zero, and there is an eigenvalue, $\lambda = 1$. Otherwise, if there are r zero entries, permute the rows so that the nonzero entries in the first column are in the top r rows. Then

permute the columns, so that the diagonal entries in the 2nd to the nth rows remain -1.

3. Repeat 1-2 for all the other columns in turn, adding the columns to the right and then rearranging.

The matrix will now be in block triangular form:

$$\begin{vmatrix} A_{11} & & * & \\ & A_{22} & & \\ & & \ddots & \\ & \mathbf{0} & & A_{kk} \end{vmatrix}$$

where A_{ii} are square sub-matrices. The determinant of the complete matrix is just the product of the determinants of the block diagonal matrices, which can only be zero if any of the columns are zero, or linearly dependent, which can only be the case if there is a subset of minima from which there is zero probability of escape.

6

Conclusions and outlook

So what have we achieved? We set out to try and understand the underlying PES for various model glasses, focusing particularly on the popular binary Lennard-Jones (BLJ) mixture. Previous studies of the energy landscape have tended to focus on minima, obtained by regular quenching of MD trajectories. Barrier distribution statistics can only be inferred from such techniques, and lack of ergodicity at low temperatures makes exploration of very low lying regions of the PES impossible.

Global optimisation, by basin-hopping, enabled us to find new crystal structures for the BLJ system. It had previously been assumed that its excellent glass-forming ability was due to the absence of a stable crystal structure. Instead, we showed that the glass-forming ability was more likely to be due to the entropic barrier to crystallisation from the melt, owing to the vanishing probability of nucleation of the layered structure. This natural conclusion was verified further by the rapidly growing number of minima in the BLJ system as the landscape was ascended, which we illustrated in a simplified disconnectivity graph. The Stillinger-Weber silicon potential, and homogeneous systems were found to possess funnel-type potential energy surfaces in the region of the crystal.

Generation of rearrangement pathways in low-lying regions of the PES in the second chapter was consistent with experimental findings on real glassy systems, in that we found evidence of enhanced low-frequency vibrational normal modes, and processes with extremely low barriers, which were potential candidates for two-level systems. The omnipresence of low barriers, which are kinetically accessible well below the glass transition, led us to develop a threshold criterion to separate nondiffusive and diffusive rearrangements. We were then able to define a ‘megabasin’ as a set of rearrangements that are only connected by pathways that are nondiffusive. Generation of stationary points at constant pressure showed that the nondiffusive rearrangements were density-independent, while barriers to diffusion increased with density.

Finally, we implemented kinetic Monte Carlo to try and understand dynamics in the supercooled BLJ liquid. The surprising result, that we learned due to the failure of the KMC to replicate MD, was that approaching T_c is appears that potential energy barriers to rearrangement are the same as at much higher temperature. Instead, the super-Arrhenius slowing down appears to be due to decreasing connectivity between megabasins in low-lying regions of the PES. The agreement as T_c is approached, of both the distributions of the energies of minima sampled and the diffusion constants, suggest future KMC simulations below T_c simulating ageing processes may be fruitful.

6.1 OUTLOOK

Studying the landscape by generating stationary points is a relatively new way to tackle the problems in supercooled liquids and glasses. Computational expense is still a problem, particularly for KMC. Much time is wasted retracing one's steps, finding transition states that have already been found. Development of new methods that could increase this efficiency would make KMC a much more practical proposition. As we saw in the previous chapter, KMC falls down at temperatures relatively modest compared to T_c, as it cannot find enough diffusive transition states connected to higher energy minima and so cannot sample the surface properly. Engineering an improved transition state searching algorithm might alleviate this problem.

Kinetic Monte Carlo is certainly applicable below T_c, and may yield some interesting results. We have not touched upon ageing in the present work: this is an obvious future application of the methodology, as not only does the efficiency of KMC start to compete with MD but as the system is relaxing down the surface, KMC is not challenged by high entropy in the same way as in the present work.

Our picture of the relationship between configurational entropy and connectivity needs further investigation. One possible method is Wales' discrete path sampling algorithm.[161] This approach involves the averaging over an ensemble of paths between two regions of configuration space via transition states and intermediate minima. This need not suffer from the same problems as KMC, as long as the PES is sampled representatively, and so it may be possible to verify our findings for the 60-atom BLJ system for larger systems. It can also deal with processes that are too slow even for KMC, and so may allow simulation of glass formers at and around T_g. However, the method still requires some development to deal with transport properties and entropically-driven phase transformations such as the melting of a crystal.

In general, a universal feature of theories of glassy and supercooled liquid dynamics is their alleged universality. Analysis of the PES from first principles, as presented here, may hold the key to understanding why many of these theories achieve some success. We hope that the present work is a small step in this direction.

REFERENCES

[1] M. Goldstein, J. Chem. Phys. **51**, 3728 (1969).

[2] G. S. Fulcher, J. Am. Ceram. Soc. **8**, 339 (1925).

[3] H. Vogel, Z. Phys. **22**, 645 (1921).

[4] G. Tammann and W. Z. Hesse, Anorg. Allgem. Chem. p. 245 (1926).

[5] C. Angell, J. Non-Cryst. Solids **102**, 205 (1988).

[6] M. Paluch, S. J. Rzoska, P. Habdas and J. Ziolo, J. Phys. Condensed Matter. **8**, 10885 (1996).

[7] M. Paluch, J. Ziolo and S. J. Rzoska, Phys. Rev. E **56**, 5764 (1997).

[8] R. Böhmer and C. A. Angell, in *Disorder Effects on Relaxational Processes*, edited by R. Richert and A. Blumen, Berlin (1994), Springer.

[9] C. A. Angell, Science **267**, 1924 (1995).

[10] F. H. Stillinger, Science **267**, 1935 (1995).

[11] W. Kauzmann, Chem. Rev. **43**, 219 (1948).

[12] C. A. Angell, J. Non-Cryst. Solids **131-133** (1991).

[13] G. Williams and D. C. Watts, J. Chem. Soc., Faraday Trans. **66**, 80 (1970).

[14] R. Kohlrausch, Ann. Phys. (Leipzig) **12**, 393 (1847).

[15] R. G. Palmer, D. L. Stein, E. Abrahams and P. W. Anderson, Phys. Rev. Lett. **53**, 958 (1984).

[16] O. Edholm and C. Blomberg, Chem. Phys. **252**, 221 (2000).

[17] G. P. Johari and M. Goldstein, J. Chem. Phys. **53**, 2372 (1970).

[18] G. P. Johari and M. Goldstein, J. Chem. Phys. **55**, 4245 (1971).

[19] B. I. Bleaney and B. Bleaney, *Electricity and Magnetism*, Oxford University Press, Oxford (1976).

[20] N. G. McCrum, B. E. Read and G. Williams, *Anelastic and dielectric effects in polymeric solids*, Wiley, New York (1967).

[21] G. P. Mikhailov, in *Physics of Non-Crystalline Solids*, edited by J. A. Prins, pp. 270–282, Amsterdam (1965), North Holland.

[22] G. P. Johari, J. Chem. Phys. **58**, 1766 (1973).

[23] F. R. Blackburn, C. Y. Wang and M. D. Ediger, J. Phys. Chem. **100**, 18249 (1996).

[24] F. Fujara, B. Geil, H. Sillescu and G. Fleischer, Z. Phys. B. **88**, 195 (1992).

[25] M. T. Cicerone and E. M. D., J. Chem. Phys. **104**, 7210 (1996).

[26] M. D. Ediger, Annu. Rev. Phys. Chem. **51**, 99 (2000).

[27] D. Ehlich and H. Sillescu, Macromolecules **23**, 1600 (1990).

[28] E. Rössler and J. Eiermann, J. Chem. Phys. **104**, 5237 (1994).

[29] H. Sillescu, J. Chem. Phys. **104**, 4877 (1996).

[30] M. D. Ediger, J. Non-Cryst. Solids **235-237**, 10 (1998).

[31] K. L. Ngai, J. Phys. Chem. B. **103**, 10684 (1999).

[32] P. W. Anderson, B. I. Halperin and C. M. Varma, Philos. Mag. **25**, 1 (1972).

[33] W. A. Phillips, J. Low Temp. Phys. **7**, 351 (1972).

[34] C. Zeller and R. O. Pohl, Phys. Rev. B **4**, 2029 (1971).

[35] W. A. Phillips (ed.), *Amorphous solids: low temperature properties*, Springer-Verlag, New York (1981).

[36] X. Liu, B. E. White, R. O. Pohl, E. Iwanizcko, K. M. Jones, A. H. Mahan, B. N. Nelson, S. Crandall and S. Veprek, Phys. Rev. Lett. **78**, 4418 (1997).

[37] G. Daldoss, O. Pilla, G. Viliani, C. Brangian and G. Ruocco, Phys. Rev. B **60**, 3200 (1999).

[38] C. A. Angell, J. Phys. Condensed Matter. **12**, 6463 (2000).

[39] N. I. Agladze and A. J. Sievers, Phys. Rev. Lett. **80**, 4209 (1998).

[40] U. Buchenau, N. Prager, N. Nücker, A. J. Dianoux, N. Ahmad and W. A. Phillips, Phys. Rev. B **34**, 5665 (1986).

[41] A. P. Sokolov, E. Rossler, A. Kisliuk and D. Quitmann, Phys. Rev. Lett. **71**, 2062 (1993).

[42] S. Elliott, *Physics of amorphous materials*, Longman (1983).

[43] S. Taraskin and S. Elliott, Europhys. Lett. **39**, 37 (1997).

[44] S. N. Taraskin and S. R. Elliot, Phys. Rev. B **59**, 8752 (1999).

[45] H. R. Schober and C. Oligschleger, Phys. Rev. B **53**, 11469 (1996).

[46] V. Mazzacurati, G. Ruocco and M. Sampoli, Europhys. Lett. **34**, 681 (1996).

[47] T. Uchino and T. Yoko, J. Chem. Phys. **108**, 8130 (1998).

[48] G. Guillot and Y. Guissani, Phys. Rev. Lett. **78**, 2401 (1997).

[49] A. F. Ioffe and A. R. Regel, Prog. Semicond. **4**, 237 (1960).

[50] S. P. Das, Phys. Rev. E **59**, 3870 (1999).

[51] U. Buchenau, Y. M. Galperin, V. L. Gurevich and H. Schober, Phys. Rev. B **43**, 5039 (1991).

[52] U. Buchenau, Y. M. Galperin, V. L. Gurevich, D. A. Parshin, M. A. Ramos and H. R. Schober, Phys. Rev. Lett. **46**, 2798 (1992).

[53] M. Paluch, J. Gapinski, A. Patkowski and E. W. Fischer, J. Chem. Phys. **114**, 8048 (2001).

[54] M. Paluch, K. L. Ngai and S. Hensel-Bielowka, J. Chem. Phys. **114**, 10872 (2001).

[55] M. H. Cohen and D. Turnbull, J. Chem. Phys. **31**, 1164 (1959).

[56] K. U. Schug, H. E. King Jr. and R. Böhmer, J. Chem. Phys. **109**, 1472 (1998).

[57] J. Köplinger, G. Kasper and S. Hunklinger, J. Chem. Phys. **113**, 4701 (2000).

[58] D. Huang, D. M. Colucci and G. B. McKenna, J. Chem. Phys. **116**, 3925 (2002).

[59] R. L. Cook, H. E. King, C. A. Herbst and D. R. Herschbach, J. Chem. Phys. **100**, 5178 (1994).

[60] J. H. Gibbs and E. A. DiMarzio, J. Chem. Phys. **28**, 373 (1958).

[61] G. Adam and J. H. Gibbs, J. Chem. Phys. **43**, 139 (1965).

[62] P. J. Flory, Proc. R. Soc. A **234**, 60 (1956).

[63] F. H. Stillinger, J. Chem. Phys. **88**, 7818 (1988).

[64] M. L. Wiliams, J. Phys. Chem. **59**, 95 (1955).

[65] M. L. Williams, R. F. Landel and J. D. Ferry, J. Am. Chem. Soc. **77**, 3701 (1955).

[66] C. A. Angell, J. Res. Natl. Inst. Stand. Technol. **102**, 171 (1997).

[67] M. Dzugutov, J. Phys.: Condens. Matter **11**, A253 (1999).

[68] G. P. Johari, J. Chem. Phys. **112**, 7518 (2000).

[69] S. Sastry, Nature **409**, 164 (2001).

[70] I. Hodge, J. Res. Natl. Inst. Stand. Technol. **102**, 195 (1997).

[71] M. Dzugutov, Nature **381**, 137 (1996).

[72] S. Chapman and T. G. Cowling, *The mathematical theory of non-uniform gases*, Cambridge University Press, Cambridge (1939).

[73] J.-P. Hansen and I. R. McDonald (eds.), *Theory of simple liquids*, Academic Press, San Diego (1986).

[74] H. J. Raveche, J. Chem. Phys. **35**, 2242 (1971).

[75] J. J. Hoyt, M. Asta and B. Sadigh, Phys. Rev. Lett. **85**, 594 (2000).

[76] M. Dzugutov, preprint cond-mat/0103117 (2002).

[77] D. Kivelson, G. Tarjus, X. Zhao and S. A. Kivelson, Phys. Rev. E **53**, 751 (1994).

[78] G. Tarjus, D. Kivelson and S. Kivelson, Supercooled liquids - ACS syposium series **676**, 67 (1997).

[79] D. Kivelson and G. Tarjus, J. Chem. Phys. **109**, 5481 (1998).

[80] S. A. Kivelson, X. Zhao, D. Kivelson, T. M. Fischer and C. M. Knobler, J. Chem. Phys. **101**, 2391 (1994).

[81] G. Tarjus, D. Kivelson and P. Viot, J. Phys. Condensed Matter. **12**, 5497 (2000).

[82] F. C. Frank, Proc. R. Soc. A **215**, 43 (1952).

[83] W. Götze, in *Liquids, Freezing and the Glass Transition, Les Houches, Session LI, 1989*, edited by J.-P. Hansen, D. Levesque and J. Zinn-Justin, pp. 287–499, North-Holland, Amsterdam (1991).

[84] W. Götze and L. Sjögren, Rep. Prog. Phys. **55**, 241 (1992).

[85] W. Kob, ACS Symp. Ser. **676**, 28 (1997).

[86] E. Leutheusser, Phys. Rev. A **29**, 2765 (1984).

[87] U. Bengtzelius, W. Götze and A. Sjölander, J. Phys. C**17**, 5915 (1984).

[88] W. Götze and L. Sjögren, J. Phys. C**21**, 3407 (1988).

[89] W. Götze and L. Sjögren, Z. Phys. B. **65**, 415 (1987).

[90] W. Götze, J. Phys.: Condens. Matter **11**, A1 (1999).

[91] W. van Megen and S. M. Underwood, Phys. Rev. Lett. **70**, 2766 (1993).

[92] W. van Megen and S. M. Underwood, Phys. Rev. E **48**, 248 (1993).

[93] W. van Megen and S. M. Underwood, Phys. Rev. E **49**, 4206 (1994).

[94] W. Kob and H. C. Andersen, Phys. Rev. Lett. **73**, 1376 (1994).

[95] W. Kob and H. Andersen, Phys. Rev. E **51**, 4626 (1995).

[96] W. Kob and H. Andersen, Phys. Rev. E **52**, 4134 (1995).

[97] M. Nauroth and W. Kob, Phys. Rev. E **55**, 657 (1997).

[98] S. Sastry, P. G. Debenedetti and F. H. Stillinger, Nature **393**, 554 (1998).

[99] J. N. Murrell and K. J. Laidler, Trans. Faraday Soc. **64**, 371 (1968).

[100] F. H. Stillinger and T. A. Weber, Phys. Rev. A **25**, 978 (1982).

[101] F. H. Stillinger and T. A. Weber, Phys. Rev. A **28**, 2408 (1983).

[102] F. H. Stillinger, Phys. Rev. E **59**, 48 (1999).

[103] P. G. Debenedetti and F. H. Stillinger, Nature **410**, 259 (2001).

[104] A. Heuer and S. Büchner, J. Phys. Condensed Matter. **12**, 6535 (2000).

[105] B. Derrida, Phys. Rev. Lett. **45**, 79 (1980).

[106] P. G. Wolynes, J. Res. Natl. Inst. Stand. Technol. **102**, 187 (1997).

[107] J. D. Ferry, J. Am. Chem. Soc. **72**, 3746 (1950).

[108] G. Seeley and T. Keyes, J. Chem. Phys. **912**, 5581 (1989).

[109] T. Keyes, J. Chem. Phys. **103**, 9810 (1995).

[110] B. Madan and T. Keyes, J. Chem. Phys. **98**, 3342 (1993).

[111] T. Keyes, J. Chem. Phys. **106**, 46 (1997).

[112] T. Keyes, J. Chem. Phys. **101**, 5081 (1994).

[113] T. Keyes, J. Chowdhary and J. Kim, Phys. Rev. E **66**, 051110 (2002).

[114] T. Keyes, Phys. Rev. E **62**, 7905 (2000).

[115] R. Zwanzig, J. Chem. Phys. **79**, 4507 (1983).

[116] J. Chowdhary and T. Keyes, Physica A **314**, 575 (2002).

[117] J. Chowdhary and T. Keyes, Phys. Rev. E **65**, 026125 (2002).

[118] U. Zürcher and T. Keyes, Phys. Rev. E **60**, 2065 (1999).

[119] E. La Nave, A. Scala, F. Starr, F. Sciortino and H. Stanley, Phys. Rev. Lett. **84**, 4605 (2000).

[120] E. La Nave, H. E. Stanley and F. Sciortino, Phys. Rev. Lett. **88**, 035501 (2002).

[121] D. Kohen and F. H. Stillinger, Phys. Rev. E **61**, 1176 (2000).

[122] D. J. Wales and J. P. K. Doye, Phys. Rev. B **63**, 214204 (2001).

[123] F. H. Stillinger and P. G. Debenedetti, J. Chem. Phys. **116**, 3353 (2002).

[124] D. J. Wales, Science **293**, 2067 (2001).

[125] F. H. Stillinger and T. A. Weber, J. Chem. Phys. **80**, 2742 (1984).

[126] F. H. Stillinger, P. G. Debenedetti and S. Sastry, J. Phys. Chem. B. **103**, 4052 (1999).

[127] F. H. Stillinger and P. G. Debenedetti, J. Phys. Chem. B. **103**, 4052 (1999).

[128] C. A. Angell, B. E. Chards and V. Velikov, J. Phys. Condensed Matter. **11**, A75 (1999).

[129] T. Keyes and J. Chowdhary, Phys. Rev. E **64**, 032201 (2001).

[130] L. Angelani, G. Parisi, G. Ruocco and G. Viliani, Phys. Rev. E **61**, 1681 (2000).

[131] K. Broderix, K. K. Bhattacharya, A. Cavagna, A. Zippelius and I. Giardina, Phys. Rev. Lett. **85**, 5360 (2000).

[132] L. Angelani, R. Di Leonardo, G. Parisi and G. Ruocco, Phys. Rev. Lett. **87**, 055502 (2001).

[133] A. Scala, L. Angelani, R. Di Leonard, G. Ruocco and F. Sciortino, Philos. Mag. B **82**, 151 (2002).

[134] R. Di Leonardo, L. Angelani, G. Parisi, G. Ruocco, A. Scala and F. Sciortino, Philos. Mag. B **82**, 163 (2002).

[135] A. Cavagna, Europhys. Lett. **53**, 490 (2001).

[136] D. J. Wales, *Energy Landscapes*, Cambridge University Press, Cambridge (2003), In press.

[137] J. P. K. Doye and D. J. Wales, J. Chem. Phys. **116**, 3777 (2002).

[138] G. T. Barkema and N. Mousseau, Phys. Rev. Lett. **77**, 4358 (1996).

[139] G. T. Barkema and N. Mousseau, Phys. Rev. Lett. **81**, 1865 (1998).

[140] G. T. Barkema and N. Mousseau, Phys. Rev. B **62**, 4985 (2000).

[141] G. T. Barkema, N. Mousseau and S. W. de Leeuw, J. Chem. Phys. **112**, 960 (2000).

[142] G. T. Barkema and N. Mousseau, Computational Physics Communications **122**, 206 (1999).

[143] J. H. Shin and H. A. Atwater, Phys. Rev. B **48**, 5964 (1993).

[144] S. Roorda, W. C. Sinke, J. M. Poate, D. C. Jacobson, S. Dierker, B. S. Dennis, D. J. Eaglesham, F. Spaepen and P. Fuoss, Phys. Rev. B **44**, 3702 (1991).

[145] N. P. Kopsias and D. N. Theodorou, J. Chem. Phys. **109**, 8573 (1998).

[146] G. M. Crippen and H. A. Scheraga, Archives of Biochemistry and Biophysics **144**, 462 (1971).

[147] J. Pancíř, Collect. Czech. Chem. Commun. **40**, 1112 (1974).

[148] R. L. Hilderbrandt, Computers and Chemistry **1**, 179 (1977).

[149] C. J. Cerjan and W. H. Miller, J. Chem. Phys. **75**, 2800 (1981).

[150] D. J. Wales, Phys. Rev. A **49**, 2195 (1994).

[151] D. J. Wales and T. R. Walsh, J. Chem. Phys. **105**, 6957 (1996).

[152] L. J. Munro and D. J. Wales, Phys. Rev. B **59**, 3969 (1999).

[153] D. J. Wales, J. P. K. Doye, M. A. Miller, P. N. Mortenson and T. R. Walsh, Adv. Chem. Phys. **115**, 1 (2000).

[154] D. J. Wales, J. Chem. Soc., Faraday Trans. **88**, 653 (1992).

[155] D. J. Wales, J. Chem. Soc., Faraday Trans. **89**, 1305 (1993).

[156] W. H. Press, B. P. Flannery, S. A. Teukolsky and W. T. Vetterling, *Numerical Recipes*, Cambridge University Press, Cambridge (1986).

[157] D. Liu and J. Nocedal, Mathematical Programming B **45**, 503 (1989).

[158] T. F. Middleton and D. J. Wales, Phys. Rev. B **64**, 024205 (2001).

[159] M. Allen and D. J. Tildesley, *The Computer Simulation of Liquids*, Clarendon Press, Oxford (1987).

[160] H. Jónsson, G. Mills and K. W. Jacobsen, in *Classical and Quantum Dynamics in Condensed Phase Simulations*, edited by B. J. Berne, G. Cicotti and D. F. Coker, Singapore (1998), World Scientific.

[161] D. J. Wales, Mol. Phys. **100**, 3285 (2002).

[162] D. J. Wales, Mol. Phys. p. In press (2002).

[163] A. Mukherjee, S. Bhattacharyya and B. Bagchi, J. Chem. Phys. **116**, 4577 (2002).

[164] W. D. Luedtke and U. Landman, Phys. Rev. B **37**, 4656 (1988).

[165] W. D. Luedtke and U. Landman, Phys. Rev. B **40**, 1164 (1989).

[166] C. J. Tsai and K. D. Jordan, J. Phys. Chem. **97**, 11227 (1993).

[167] J. P. K. Doye and D. J. Wales, Z. Phys. D **40**, 194 (1997).

[168] N. Mousseau and G. T. Barkema, Phys. Rev. E **57**, 2419 (1998).

[169] H. E. A. Huitema, J. P. van der Eerden, J. J. M. Janssen and H. Human, Phys. Rev. B **62**, 14690 (2000).

[170] D. J. Wales and J. P. K. Doye, J. Phys. Chem. A. **101**, 5111 (1997).

[171] Z. Li and H. A. Scheraga, Proc. Natl. Acad. Sci. USA **84**, 6611 (1987).

[172] Z. Li and H. A. Scheraga, J. Mol. Struct. (Theochem) **179**, 333 (1988).

[173] P. N. Mortenson, *Energy landscape of model polypeptides*, Ph.D. thesis, Cambridge University (May 2001).

[174] O. M. Becker and M. Karplus, J. Chem. Phys. **106**, 1495 (1997).

[175] D. J. Wales, M. A. Miller and T. R. Walsh, Nature **394**, 758 (1998).

[176] R. S. Berry and R. Breitengraser-Kunz, Phys. Rev. Lett. **74**, 3951 (1995).

[177] R. E. Kunz and R. S. Berry, J. Chem. Phys. **103**, 1904 (1995).

[178] P. E. Leopold, M. Montal and J. N. Onuchic, Proc. Natl. Acad. Sci. USA **89**, 8721 (1992).

[179] Y. Levy and O. M. Becker, Phys. Rev. Lett. **81**, 1126 (1998).

[180] J. P. K. Doye, M. A. Miller and D. J. Wales, J. Chem. Phys. **110**, 6896 (1999).

[181] M. A. Miller, J. P. K. Doye and D. J. Wales, J. Chem. Phys. **110**, 328 (1999).

[182] T. F. Middleton, J. Hernandez-Rojas, P. N. Mortenson and D. J. Wales, Phys. Rev. B **64**, 184201 (2001).

[183] O. K. Rice and H. C. Ramsperger, J. Am. Chem. Soc. **49**, 1617 (1927).

[184] L. S. Kassel, J. Phys. Chem. **32**, 225 (1928).

[185] A. Marcus and O. K. Rice, J. Phys. Colloid. Chem. **55**, 894 (1951).

[186] J. E. Jones and A. E. Ingham, Proc. R. Soc. A **107**, 636 (1925).

[187] The 'unit' density system studied in our previous report[158] in fact has density 0.99611.

[188] T. A. Weber and Stillinger, Phys. Rev. B **31**, 1954 (1985).

[189] R. M. Ernst, S. R. Nagel and G. S. Grest, Phys. Rev. B **43**, 8070 (1991).

[190] S. D. Stoddard and J. Ford, Phys. Rev. A **8**, 1504 (1973).

[191] K. Tanaka, H. Okamoto, E. Maruyama, T. Shimada and M. Sato (Trans.), *Amorphous Silicon*, Wiley, New York (1999).

[192] E. R. Cowley, Phys. Rev. Lett. **60**, 2379 (1988).

[193] S. J. Cook, Phys. Rev. B **47**, 7686 (1993).

[194] H. Balamane, T. Halicioglu and W. A. Tiller, Phys. Rev. B **46**, 2250 (1992).

[195] F. H. Stillinger and T. A. Weber, Phys. Rev. B **31**, 5262 (1985).

[196] J. Q. Broughton, Phys. Rev. B **35**, 9120 (1987).

[197] N. Mousseau and G. T. Barkema, Phys. Rev. B **61**, 1898 (2000).

[198] Y. Song, R. Malek and N. Mousseau, Phys. Rev. B **62**, 15680 (2000).

[199] F. Wooten, K. Winer and D. Weaire, Phys. Rev. Lett. **54**, 1392 (1985).

[200] C. A. Angell and S. S. Borick, J. Phys. Condensed Matter. **11**, 8163 (1999).

[201] S. Ansell, S. Krishnan, J. J. Felten and D. L. Price, J. Phys. Condensed Matter. **10**, L73 (1998).

[202] C. A. Angell, A. Borick and M. Grabow, J. Non-Cryst. Solids **205-207**, 463 (1996).

[203] C. A. Angell, D. Bressel, M. Hemmati, E. J. Sare and J. C. Tucker, Phys. Chem. Chem. Phys. **2**, 1559 (2000).

[204] C. A. Angell and C. T. Moynihan, Met. Mat. Trans. B **31B**, 587 (2000).

[205] O. Mishima and E. Stanley, Nature pp. 329–335 (1998).

[206] X. Liu, B. E. White Jr., R. Pohl, E. Iwanizcko, K. M. Jones, A. H. Mahan, B. N. Nelson, R. S. Crandall and S. Veprek, Phys. Rev. Lett. **78**, 4418 (1997).

[207] C. A. Angell, C. T. Moynihan and M. Hemmati, J. Non-Cryst. Solids **274**, 319 (2000).

[208] K. C. Pandey, Phys. Rev. Lett. **57**, 2287 (1986).

[209] M. Parinello and A. Rahman, J. Appl. Phys. **52**, 7182 (1981).

[210] F. Sciortino, W. Kob and P. Tartaglia, Phys. Rev. Lett. **83**, 3214 (1999).

[211] T. B. Schroder, S. Sastry, J. C. Dyre and S. C. Glotzer, J. Chem. Phys. **112**, 9834 (2000).

[212] C. Donati, F. Sciortino and P. Tartaglia, Phys. Rev. Lett. **85**, 1464 (2000).

[213] S. Sastry, Phys. Rev. Lett. **85**, 590 (2000).

[214] S. Sastry, J. Phys.-Cond. Matt. **12**, 6515 (2000).

[215] F. Sciortino, W. Kob and P. Tartaglia, J. Phys.-Cond. Matt. **12**, 6525 (2000).

[216] L. Angelani, R. Di Leonardo, G. Ruocco, A. Scala and F. Sciortino, Phys. Rev. Lett. **85**, 5356 (2000).

[217] J. Hernandez-Rojas and D. J. Wales, Preprint cond-mat/0112128 (2001).

[218] T. Hahn (ed.), *International tables for Crystallography*, vol. A, Space Group Symmetry, International Union of Crystallography, Dordrecht, Holland (1983).

[219] A. Bowman, G. Arnold and N. Krikorian, Acta Crystallographica B **27**, 1067 (1971).

[220] D. Fletcher, R. McMeeking and D. Parkin, J. Chem. Inf. Comput. Sci **36**, 746 (1996).

[221] D. J. Wales, J. P. K. Doye, A. Dullweber, M. P. Hodges, F. Y. Naumkin, F. Calvo, J. Hernandez-Rojas and T. F. Middleton, The Cambridge Cluster Database, URL http://www-wales.ch.cam.ac.uk/CCD.html (2001).

[222] F. Calvo, *Personal Communication* (2002).

[223] J. R. Fern/'andez and P. Harrowell, Phys. Rev. E **67**, 011403 (2002).

[224] P. J. Steinhardt, D. Nelson and M. Ronchetti, Phys. Rev. B **28**, 784 (1983).

[225] R. M. Lynden-Bell and D. J. Wales, J. Chem. Phys. **101**, 1460 (1994).

[226] R. E. Leone and P. v. R. Schleyer, Angew. Chem. Int. Ed. Engl. **9**, 860 (1970).

[227] R. Malek and N. Mousseau, Phys. Rev. E **62**, 7723 (2000).

[228] N. Mousseau, *Personal Communication* (2002).

[229] D. Donati, J. F. Douglas, W. Kob, S. J. Plompton, P. H. Poole and S. C. Glotzer, Phys. Rev. Lett. **80**, 2338 (1998).

[230] F. H. Stillinger and T. A. Weber, J. Phys. Chem. **87**, 2833 (1983).

[231] B. Doliwa and A. Heuer, Phys. Rev. Lett. **80**, 4915 (1998).

[232] D. J. Wales and J. Uppenbrink, Phys. Rev. B **50**, 12342 (1994).

[233] L. J. Munro and D. J. Wales, Faraday Disc. **106**, 409 (1997).

[234] B. Doliwa and A. Heuer, preprint cond-mat/0209139 (2002).

[235] B. Doliwa and A. Heuer, preprint cond-mat/0205283 (2002).

[236] G. Gilbert and S. C. Smith, *Theory of Unimolecular and combination Reactions*, Blackwell, Oxford (1990).

[237] T. F. Middleton and D. J. Wales, J. Chem. Phys. **118**, 4583 (2003).

[238] J. Bell and P. Dean, Philos. Mag. **25**, 1381 (1972).

[239] S. Taraskin, *Pers. com.* (2000).

[240] M. Page and J. W. McIver, J. Chem. Phys. **88**, 922 (1988).

[241] E. A. Jagla, Mol. Phys. **99**, 753 (2001).

[242] P. M. Morse, Phys. Rev. **34**, 57 (1929).

[243] N. G. van Kampen, *Stochastic Processes in Physics and Chemistry*, North-Holland, Amsterdam (1981).

[244] K. A. Fichthorn and W. H. Weinberg, J. Chem. Phys **95**, 1090 (1991).

[245] A. B. Bortz, M. H. Kalos and J. L. Lebowitz, J. Comp. Phys.**17**, 10 (1975).

[246] D. J. McGinty, J. Chem. Phys. **55**, 580 (1971).

[247] J. J. Burton, J. Chem. Phys. **56**, 3133 (1972).

[248] M. R. Hoare, Adv. Chem. Phys. **40**, 49 (1979).

[249] G. Franke, E. R. Hilf and and P. Borrmann, J. Chem. Phys. **98**, 3496 (1993).

[250] D. J. Wales, Mol. Phys. **78**, 151 (1993).

[251] H. C. Kang and W. H. Weinberg, J. Chem. Phys. **90**, 2824 (1988).

[252] L. A. Ray and R. C. Baetzold, J. Chem. Phys. pp. 2871–2878 (1990).

[253] M. I. Larsson, Phys. Rev. B **64**, 115428 (2001).

[254] F. M. Bulnes, V. D. Pereyra and J. L. Riccardo, Phys. Rev. E **58**, 86 (1998).

[255] G. Henkelman and H. Jónsson, J. Chem. Phys. **115**, 9657 (2001).

[256] R. Q. Snurr, A. T. Bell and D. N. Theodorou, J. Phys. Chem. **98**, 11948 (1994).

[257] M. L. Greenfield and D. N. Theodorou, Macromolecules **31**, 7068 (1998).

[258] L.-M. Martinez and C. A. Angell, Nature **410**, 663 (2001).

[259] D. Plazek, J. Chem. Phys. **49**, 3678 (1968).

[260] R. A. Horn and C. R. Johnson, *Matrix Analysis*, Cambridge University Press, Cambridge (1985).

PUBLICATIONS

Some of the work presented in this thesis has been published in the following papers.

CHAPTER 2

- 'Crystals of binary Lennard-Jones solids',
  T. F. Middleton, J. Hernàndez-Rojas, P. N. Mortenson and D. J. Wales, *Phys. Rev. B*, **64**, 184201 (2001).

CHAPTER 3

- 'Energy landscapes of model glasses',
  T. F. Middleton, and D. J. Wales, *Phys. Rev. B*, **64**, 024205 (2001).

- 'Energy landscapes of model glasses II: results at constant pressure',
  T. F. Middleton, and D. J. Wales, *J. Chem. Phys.*, **118**, 4583 (2003).

CHAPTER 4

- 'Kinetic Monte Carlo simulation of binary Lennard-Jones solid',
  T. F. Middleton, D. J. Wales, (2003), *Submitted.*